12-2011

Studies Toward the Development of a Microelectrode Array for Detection of Dopamine Through Redox Cycling

Anupama Aggarwal
University of Arkansas, Fayetteville

STUDIES TOWARD THE DEVELOPMENT OF A MICROELECTRODE ARRAY FOR DETECTION OF DOPAMINE THROUGH REDOX CYCLING

STUDIES TOWARD THE DEVELOPMENT OF A MICROELECTRODE ARRAY FOR DETECTION OF DOPAMINE THROUGH REDOX CYCLING

A dissertation submitted in partial fulfillment
of the requirements for the degree of
Doctor of Philosophy in Chemistry

By

Anupama Aggarwal
University of Delhi
Bachelor of Science in Chemistry, 2005

December 2011
University of Arkansas

ABSTRACT

Redox cycling is an electrochemical technique that cycles the reversible redox species between its oxidative states repeatedly on generator and collector electrodes. Two or more individually-addressable microelectrodes located close to each other allow redox cycling to be possible. Electrochemical behavior of a biologically important molecule, dopamine is examined under redox cycling conditions. To our knowledge, this is the first report on detection of physiological concentration of dopamine in presence of up to 100 times excess ascorbate with the use of redox cycling, without the involvement of polymer coating such as Nafion®.

Microfabrication was used to produce different geometries (parallel bands and concentric rings) with feature size of 4 µm or 25 µm and inter-electrode spacing of 4 µm or 25 µm on a single substrate (microelectrode arrays). Comparison of the individual electrochemical response of different arrangements of individually addressable elements composing generator and collector electrodes on band and ring microelectrode arrays is presented. The individually addressable nature of microelectrodes allowed the study of different combinations of anodic and cathodic electrodes and the current at the individual elements composing the generator and the collector. Reversible electroactive species hexaammineruthenium (III) chloride in a 0.5 M potassium chloride electrolyte solution was used to perform the electrochemical characterization and comparisons of the microelectrode arrays. Behavior of band and ring microelectrodes in an array format during redox cycling is compared to each other as well as to the available theory.

The optimized geometry and arrangement of microelectrodes is used to exhibit detection of dopamine with and without redox cycling. Comparison of dopamine behavior in presence and absence of redox cycling and other available methods of detection is provided. Detection of dopamine in presence of some of the common interferences (ascorbate and 3,4-

dihydroxyphenylacetic acid) is shown with and without redox cycling on unmodified electrodes as well as on electrodes modified with Nafion®.

These studies indicate that redox cycling can detect dopamine at physiologically relevant concentrations in presence of interferences, but will require the coating of electrodes with Nafion in addition to broaden the range of interfering compounds that can be eliminated. Traditional voltammetric methods to detect dopamine cannot measure resting, or static dopamine concentrations where redox cycling would be of further interest. Redox cycling provides elimination from the interfering ascorbate signal, enhancing the sensitivity toward the analyte simultaneously.

Based on the knowledge gathered from comparison of different electrodes and redox cycling of dopamine, an interdigitated microelectrode probe design suitable for investigation of redox cycling of dopamine is fabricated. The probe contains array having dimensions that will be suitable for tissue insertions studies. The knowledge gained through this project will eventually lead to a new class of multi-electrode probes for in vivo studies of neurotransmitters in neurosciences.

This dissertation is approved for recommendation
to the Graduate Council

Dissertation Director:

_____
Dr. Ingrid Fritsch

Dissertation Committee:

_____
Dr. Charles Wilkins

_____
Dr. David Paul

_____
Dr. Julie Stenken

_____
Dr. Simon Ang

DISSERTATION DUPLICATE RELEASE

I hereby authorize the University of Arkansas Libraries to duplicate this Dissertation when needed for research and/or scholarship.

Agreed _____
Anupama Aggarwal

Refused _____

ACKNOWLEDGEMENTS

I would like to sincerely thank my research advisor, Dr. Ingrid Fritsch for the invaluable support and guidance that she has provided me throughout the graduate school. This project would not have been possible without her idea. For the time and energy she has invested in shaping my career and for the patience, I am forever indebted. She has provided me the bridge between school and professional life. I will always carry with me the confidence she has shown in me.

I thank other members of my committee. I appreciate the input from Professor David W. Paul on interpretation of the data and Dr. Julie A. Stenken for providing the challenge to understand thoroughly the different aspects of my project. Dr. Julie A. Stenken has taken personal interest toward providing a balanced growth to my career. It is due to her support that I was able to attend an international conference and add to my knowledge and experience.

Many thanks to Jerry Homesley for help with testing and fixing of the scanning electrochemical microscope and other instruments, Errol Porter for the advice on fabrication of microelectrode arrays, Brandon Rogers for upgrading the polishing wheel, Alan Toland for the use of the scanning electron microscope, and K.Z. Shein for working on the Edwards evaporator.

I greatly appreciate the help of Dr. Melissa C. Weston for providing me the required training for the research. She has been a great friend in lab and a wonderful mentor. Special thanks to Dr. Wolfgang Schuhmann for providing indispensable help and valuable guidance for the use and operation of SECM and providing new stream of ideas for my project. Michaela Nebel and Thomas Erichsen provided the knowledge for the operation of SECM instrument, making a contribution in the thus far success toward my project.

Finally and most importantly, I would like to thank my parents, my brother and grandmother for their eternal love and support, and to all my dear friends for daily encouragement and enthusiasm to help me complete this journey. I greatly appreciate the initiative taken by Dr. Satya Gupta toward my higher studies.

DEDICATIONS

To Mom and Dad, I dedicate this dissertation to you!

TABLE OF CONTENTS

LIST OF FIGURES

LIST OF TABLES

1. INTRODUCTION TO REDOX CYCLING FOR DETECTION OF REDOX SPECIES

1.1 INTRODUCTION

Redox cycling is a simple electrochemical method for detection of electrochemically active and reversible compounds. It offers several advantages over other electrochemical techniques. Cyclic voltammetry carries out oxidation in the forward sweep followed by reduction in the reverse sweep (or vice versa) on a single electrode. Fast scan cyclic voltammetry does so by employing very high scan rates, such as 100 V/s – 400 V/s. Redox cycling, on the other hand, carries out oxidation and reduction simultaneously on two different but closely located electrodes. Repetitive recycling of the redox species on the two electrodes add to the current, providing amplification of signal. This increases the sensitivity of the technique. Careful selection of potentials at the electrodes can provide elimination of signal from different redox species, enhancing the selectivity of the technique. This method can be employed to mixtures of dopamine and ascorbate, important in brain chemistry, to eliminate the irreversible ascorbate signal and amplify the dopamine signal.

The concept of redox cycling originated from rotating ring disk experiments in the 1960s.[1-4] Some of the first reports on redox cycling at an array of microelectrodes were published in the early 1980s.[5-9] Redox cycling at static electrodes coincides with the initial success in microfabrication of multiple, closely-spaced microelectrodes.[5, 10-14] Since then, redox cycling has been used by several researchers for different purposes. Niwa and Morita and coworkers are among the ones to have contributed extensively toward the understanding of redox cycling.[15-20] Amatore and coworkers have worked extensively toward unlocking the theory of diffusion at microelectrodes and their arrays through simulations.[21-26] Fritsch and coworkers have worked

with arrays of microelectrodes for a long time and have explored redox cycling for detection of compounds having biological importance.[27-34]

Two fundamental requirements of redox cycling at static electrodes are: two or more *closely spaced* (25 μm or less in an open cell with no cell wall or ceiling) microelectrodes poised at oxidative and reductive potentials and an electrochemically-*reversible* redox species. The main principle of the technique is as follows: a reversible redox species undergoes oxidation at the anode, the product diffuses to the nearby cathode and reduces back (or vice versa). Current is produced at both the electrodes. The redox species can undergo multiple redox cycles between anode and cathode until it diffuses out to the bulk solution. The number of redox cycles depend on the spacing between the electrodes and the diffusion coefficient of the molecule. All the redox cycles of the molecule contribute to the total current signal. This provides enhancement in the current signal compared to the current obtained at a single microelectrode, thereby increasing the sensitivity of the technique toward the analyte. Figure 1 shows the basic underlying mechanism of redox cycling.

Dopamine is an extremely important neurological molecule. It has electrochemical properties and is present in a chemical matrix in the brain that would make it suitable for detection by redox cycling. Its seemingly endless list of functions in brain includes behavior and cognition, punishment and reward, analytical thinking, learning, motivation, sleep, mood, and attention. Dysfunction in dopamine uptake or release mechanism is diagnosed to be the cause of various neurological diseases such as Schizophrenia,[35] Parkinson's disease,[36, 37] Huntington's disease,[38] Tourette's syndrome,[39] and drug abuse.[37, 40, 41]

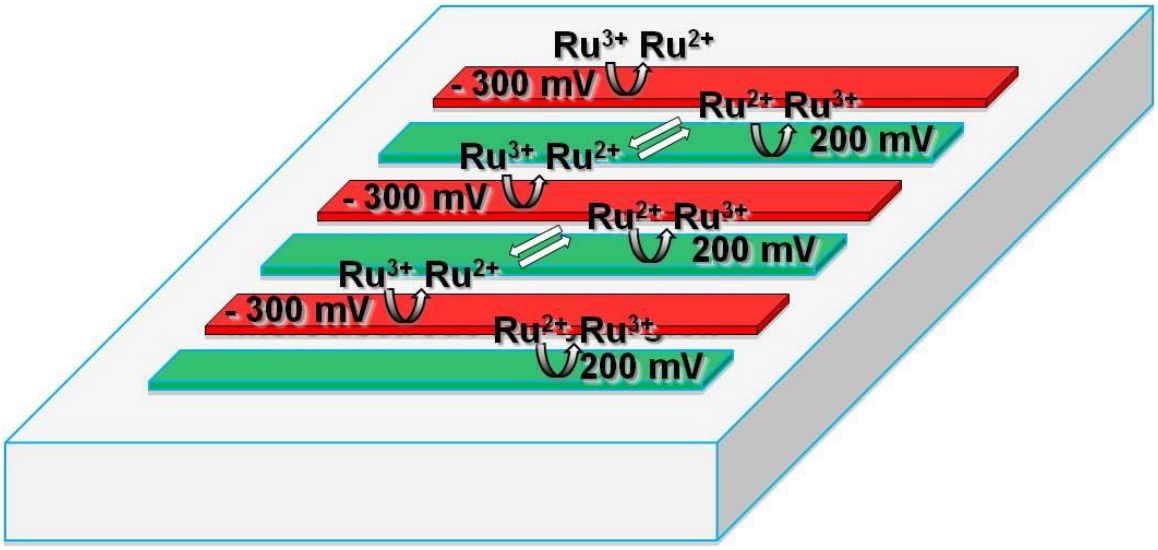

Figure 1.1 Schematic of redox cycling is shown on a microelectrode array containing multiple closely located microelectrodes, specific to the example of the model compound hexaammineruthenium (III) chloride. One set of electrode(s) is poised at the anodic potential to produce the oxidized form of a redox species, Ru^{3+} (shorthand for $[Ru(NH_3)_6]^{3+}$, and the other at the cathodic potential to produce the reduced form of a redox species, Ru^{2+} (shorthand for $Ru(NH_3)_6^{2+}$). The starting form of the redox species converts its oxidation state at the generator electrode (the anode, +200 mV, in this example). The generator product diffuses to the nearby collector (cathode, -300 mV, in this example) and converts back to the initial redox form.

Dopamine is electrochemically reversible for a short duration of time. The oxidation product of dopamine, dopamine-o-quinone, undergoes intermolecular cyclization to form a substituted indole, which is an inert species as shown in figure 1.2.[42] However, the reaction has slow kinetics. Thus, if the microelectrodes are positioned close enough to each other, then dopamine can be cycled several times before it converts into the indole form or diffuses into the bulk. Redox cycling on dopamine has been performed in the past on microelectrode arrays.[19, 27, 43-48] Our work explores the configuration of generator and collector electrodes which provides the best results for dopamine detection in presence of at least up to 100 times excess ascorbate without the need for electrode modification.

Microfabrication is an expensive and time-consuming tool, which does not allow flexibility of design and arrangement of the fabricated electrodes, except by making a new set of arrays. Thus, preliminary studies involving the evaluation of redox cycling were carried out here on individually addressable microelectrode arrays, which allows for variation in the number, assignment (anode or cathode), and spacing of activated electrodes to explore redox cycling from different configurations. The optimization studies were performed to obtain a limit of detection for dopamine at physiological concentrations in the presence of at least up to 100 times excess ascorbate. Optimization of method development and design of microelectrode arrays including the optimal spacing between microelectrodes would be required to obtain best results for detection of dopamine through redox cycling. It is estimated that decreasing the gap between the electrodes from 4 μm in the present design to 0.8 μm in the future design will provide the detection limit of 1 μM dopamine in presence of 100 μM ascorbate on the probe like sensors discussed below. More specific details and the context in which different studies are done have been described in the introductions of individual chapters.

Dopamine-o-quinone **Substituted Indole**

Intramolecular cyclization of DA.[43]

Figure 1.2. Intramolecular cyclization of dopamine to form substituted indole.

It is important not only to demonstrate the ability to detect physiological concentrations of dopamine in the brain and in the presence of interference(s), but equally important to demonstrate a technique to do so with minimal tissue damage. This would require scaling down the array to fit to a shape (probe like) and dimensions (100 µm wide x 100 µm thick) suitable for in vivo experiments. Thus, the optimized designs were also transferred to arrays on dagger-like probes to better accommodate the requirements for tissue insertion and in vivo experiments in the future. The arrays are 80 µm in width contained in the center of the probe region of a much bigger sensor. When ready for the in vivo experiments, the sensors would be scaled down to 100 µm x 100 µm using DRIE. At this time, their bigger size facilitated in their handling. Characterization as well as redox cycling studies were performed on the probe arrays to demonstrate their ability to detect dopamine.

Scanning electrochemical microscopy (SECM) is a powerful tool for studying processes at surfaces both biological and inorganic.[49, 50] It will allow us to study localized electrochemistry on generator and collector surface while dopamine is under redox cycling. When operated in constant distance control mode with nanoelectrode tips, it achieves submicron spatial resolution. It allows tunable placement of a microelectrode tip near the chip-based electrodes. SECM makes it possible to study the effect of varying distance between its tip and individual the microelectrodes on the chip while redox cycling occurs between the SECM tip and the microelectrodes. The knowledge on survival of dopamine in presence of interference, and its local electrochemistry will better allow us to understand its behavior and design sensor for its detection.

Microdisk electrodes were fabricated to be used as SECM tips. Characterization of the fabricated electrodes was performed to determine their electrochemical area and quality of their

seal. Effects of varying spacing between the SECM tip and the microelectrodes on the array (while involved in redox cycling with each other) were explored.

1.2 OVERVIEW OF THE STUDIES DESCRIBED IN THIS DISSERTATION

The goal of the project was to perform method development for detection of dopamine through redox cycling. The fundamental studies described in the subsequent chapters lead to the fabrication of an optimized device. Fabrication of small feature microelectrode array was successfully accomplished at the HiDEC facility (University of Arkansas, Fayetteville, AR). A procedure was established to speed up the fabrication of small features for future devices. Detailed characterization of the arrays is presented with a well-behaved electrochemical species, hexaammineruthenium (III) chloride. Achievement of small, 4-μm features allowed redox cycling to be possible with dopamine with and without the presence of interfering species, ascorbate and 3,4-dihydroxyphenylacetic acid (DOPAC) at physiological concentrations. Dopamine calibration curves are presented.

The results establish that redox cycling is an effective means for detecting dopamine in the presence of ascorbate. It is also shown that redox cycling is capable of detecting physiologically relevant concentrations of dopamine. However, it has never been attempted in vivo. The next step toward attempting redox cycling in vivo for dopamine detection is taken by developing the microelectrode arrays in dagger (probe-like) designs. The dimensions of the arrays contained in a probe like sensor are compatible for in vivo testing. The use of the microelectrode daggers can be expanded to other biological and environmental applications and can increase the scope of redox cycling in the neurosciences.

Please note that each chapter hence contains introductory paragraphs to support and justify the research in this dissertation. The chapters were written as self-contained manuscripts and each possesses an independent list of references. Thus, some of the contents may be repetitive.

The chapters in this dissertation contain the following information. Chapter 2 explores redox cycling using a model compound under different conditions, which include different geometries, electrode dimensions, electrode spacing, and electrode arrangements. Chapter 3 contains method development for detection of dopamine in presence of ascorbate and DOPAC using redox cycling as an electrochemical method of development. Chapter 4 describes the design and fabrication procedure for fabrication of interdigitated array probe sensors for detection of dopamine suitable for tissue insertion studies. Chapter 5 discusses the experiments performed using SECM. Finally, Chapter 6 provides an overall summary and suggests future experiments.

1.3 REFERENCES

(1) Albery, W. J.; Bruckens.S *Transactions of the Faraday Society* **1966**, *62*, 1920-&.

(2) Albery, W. J.; Bruckens.S *Transactions of the Faraday Society* **1966**, *62*, 1946-&.

(3) Albery, W. J.; Hitchman, M. L. *Ring-disc electrodes [by] W. J. Albery and M. L. Hitchman*; Clarendon Press, Oxford, 1971.

(4) Albery, W. J.; Hitchman, M. L.; Ulstrup, J. *Transactions of the Faraday Society* **1968**, *64*, 2831-&.

(5) Bard, A. J.; Crayston, J. A.; Kittlesen, G. P.; Shea, T. V.; Wrighton, M. S. *Analytical Chemistry* **1986**, *58*, 2321-2331.

(6) Corcoran, G. B.; Mitchell, J. R. *Advances in Experimental Medicine and Biology* **1982**, *136*, 1085-1098.

(7) Heikkila, R. E.; Manzino, L. *Annals of the New York Academy of Sciences* **1987**, *498*, 63-76.

(8) Liehr, J. G.; Ulubelen, A. A.; Strobel, H. W. *Journal of Biological Chemistry* **1986**, *261*, 6865-6870.

(9) Scheulen, M. E.; Kappus, H.; Thyssen, D.; Schmidt, C. G. *Biochemical Pharmacology* **1981**, *30*, 3385-3388.

(10) Chidsey, C. E.; Feldman, B. J.; Lundgren, C.; Murray, R. W. *Analytical Chemistry* **1986**, *58*, 601-607.

(11) Thormann, W.; Vandenbosch, P.; Bond, A. M. *Analytical Chemistry* **1985**, *57*, 2764-2770.

(12) Paul, E. W.; Ricco, A. J.; Wrighton, M. S. *Journal of Physical Chemistry* **1985**, *89*, 1441-1447.

(13) Kittlesen, G. P.; White, H. S.; Wrighton, M. S. *Journal of the American Chemical Society* **1984**, *106*, 7389-7396.

(14) White, H. S.; Kittlesen, G. P.; Wrighton, M. S. *Journal of the American Chemical Society* **1984**, *106*, 5375-5377.

(15) Morita, M.; Horiuchi, T.; Tabei, H. *Journal of Electroanalytical Chemistry* **1992**, *322*, 191-201.

(16) Morita, M.; Niwa, O.; Horiuchi, T. *Electrochimica Acta* **1997**, *42*, 3177-3183.

(17) Niwa, O. *Electroanalysis* **1995**, *7*, 606-613.

(18) Niwa, O.; Morita, M.; Tabei, H. *Analytical Chemistry* **1990**, *62*, 447-452.

(19) Niwa, O.; Morita, M.; Tabei, H. *Electroanalysis* **1994**, *6*, 237-243.

(20) Niwa, O.; Tabei, H.; Solomon, B. P.; Xie, F. M.; Kissinger, P. T. *Journal of Chromatography B-Biomedical Applications* **1995**, *670*, 21-28.

(21) Fosset, B.; Amatore, C.; Bartelt, J.; Wightman, R. M. *Analytical Chemistry* **1991**, *63*, 1403-1408.

(22) Amatore, C.; Da Mota, N.; Sella, C.; Thouin, L. *Analytical Chemistry* **2010**, *82*, 2434-2440.

(23) Amatore, C.; Sella, C.; Thouin, L. *Journal of Physical Chemistry B* **2002**, *106*, 11565-11571.

(24) Arkoub, I. A.; Amatore, C.; Sella, C.; Thouin, L.; Warkocz, J. S. *Journal of Physical Chemistry B* **2001**, *105*, 8694-8703.

(25) Amatore, C.; Oleinick, A.; Svir, I. *Journal of Electroanalytical Chemistry* **2004**, *564*, 245-260.

(26) Fosset, B.; Amatore, C. A.; Bartelt, J. E.; Michael, A. C.; Wightman, R. M. *Analytical Chemistry* **1991**, *63*, 306-314.

(27) Vandaveer, W. R.; Woodward, D. J.; Fritsch, I. *Electrochimica Acta* **2003**, *48*, 3341-3348.

(28) Sreenivas, G.; Ang, S. S.; Fritsch, I.; Brown, W. D.; Gerhardt, G. A.; Woodward, D. J. *Analytical Chemistry* **1996**, *68*, 1858-1864.

(29) Anderson, E. C.; Weston, M. C.; Fritsch, I. *Analytical Chemistry* **2010**, *82*, 2643-2651.

(30) Nagale, M. P.; Fritsch, I. *Analytical Chemistry* **1998**, *70*, 2908-2913.

(31) Henry, C. S.; Fritsch, I. *Journal of the Electrochemical Society* **1999**, *146*, 3367-3373.

(32) Nagale, M. P.; Fritsch, I. *Analytical Chemistry* **1998**, *70*, 2902-2907.

(33) Tatistcheff, H. B.; Fritschfaules, I.; Wrighton, M. S. *Journal of Physical Chemistry* **1993**, *97*, 2732-2739.

(34) Frisbie, C. D.; Fritschfaules, I.; Wollman, E. W.; Wrighton, M. S. *Thin Solid Films* **1992**, *210*, 341-347.

(35) Davis, K. L.; Kahn, R. S.; Ko, G.; Davidson, M. *American Journal of Psychiatry* **1991**, *148*, 1474-1486.

(36) Obata, T. *Journal of Neural Transmission* **2002**, *109*, 1159-1180.

(37) Wightman, R. M.; May, L. J.; Michael, A. C. *Analytical Chemistry* **1988**, *60*, A769-&.

(38) Bibb, J. A.; Yan, Z.; Svenningsson, P.; Snyder, G. L.; Pieribone, V. A.; Horiuchi, A.; Nairn, A. C.; Messer, A.; Greengard, P. *Proceedings of the National Academy of Sciences of the United States of America* **2000**, *97*, 6809-6814.

(39) Mink, J. W. *Pediatric Neurology* **2001**, *25*, 190-198.

(40) Koob, G. F.; Bloom, F. E. *Science* **1988**, *242*, 715-723.

(41) Phillips, P. E. M.; Stuber, G. D.; Heien, M.; Wightman, R. M.; Carelli, R. M. *Nature* **2003**, *422*, 614-618.

(42) Hawley, M. D.; Tatawawa.Sv; Piekarsk.S; Adams, R. N. *Journal of the American Chemical Society* **1967**, *89*, 447-&.

(43) Cullison, J. K.; Waraska, J.; Buttaro, D. J.; Acworth, I. N.; Bowers, M. L. *Journal of Pharmaceutical and Biomedical Analysis* **1999**, *19*, 253-259.

(44) Dam, V. A. T.; Olthuis, W.; van den Berg, A. *Analyst* **2007**, *132*, 365-370.

(45) Niwa, O.; Kurita, R.; Liu, Z. M.; Horiuchi, T.; Torimitsue, K. *Analytical Chemistry* **2000**, *72*, 949-955.

(46) Niwa, O.; Morita, M. *Analytical Chemistry* **1996**, *68*, 355-359.

(47) Niwa, O.; Morita, M.; Tabei, H. *Electroanalysis* **1991**, *3*, 163-168.

(48) Peng, W. F.; Wang, E. K. *Analytica Chimica Acta* **1993**, *281*, 663-671.

(49) Barker, A. L.; Gonsalves, M.; Macpherson, J. V.; Slevin, C. J.; Unwin, P. R. *Analytica Chimica Acta* **1999**, *385*, 223-240.

(50) Mirkin, M. V.; Horrocks, B. R. *Analytica Chimica Acta* **2000**, *406*, 119-146.

2. COMPARISON OF REDOX CYCLING BEHAVIOR AT INDIVIDUAL ELEMENTS IN MICROBAND AND MICRORING ELECTRODE ARRAYS

2.1 ABSTRACT

A comparison of electrochemical responses of *individual elements* at coplanar parallel band and concentric ring microelectrode arrays during redox cycling is reported. Redox cycling is of interest because of signal amplification and elimination of irreversible faradaic current and charging background current. The individually addressable nature of the 18 microelectrodes (4-µm wide separated by 4-µm gaps) and a multipotentiostat allowed different combinations of cathodes (generator) and anodes (collector) to be explored; and current to be monitored at (up to eight) individual or sets of the electrodes. The work was performed using an electrochemically reversible species, hexaammineruthenium (III) chloride. The microbands exhibited more efficient redox cycling than the microrings, providing better detection limits (0.014 µM for microband and 0.110 µM for microring using the alternate generator – collector arrangement of electrodes). Lower current density is observed at the ring electrodes due to overlap of diffusion layers on the inner edge of the microrings. Alternating generators and collectors, multiple collectors flanked by single generators, single generators flanked by multiple collectors, are some of the electrode configurations that were investigated. This study provides details on advantages and limitations of the different configurations.

2.2 INTRODUCTION

The studies presented in this paper compare redox cycling behavior at two different coplanar, microelectrode array (MEA) geometries: parallel bands and concentric rings. Variations in overlapping diffusion patterns of redox species for different electrode geometries lead to different electrochemical signals from redox cycling.[1, 2] Redox cycling has typically been studied by monitoring current at two sets of active electrodes,[2, 3] typically called generators and collectors and often in the form of interdigitated arrays (IDAs) of microelectrodes. Here, we independently monitor electrochemical signals arising from (up to eight) individual electrode elements. Thus, we can measure the contribution of each element to the overall current of the collective generator and collector. While some analysis has been done by simulations previously, it has not been done experimentally.[4-7]

The technique cycles the reversible redox species between its two oxidative states repeatedly between closely spaced, two or more (generator and collector) electrodes. Cathodic and anodic potentials are applied at the electrodes with respect to the standard electrode potential, E°, of the redox species. This repetitive electron transfer between the two states of a redox species adds to the current at the generator electrode(s), leading to amplification (A_F) and a signal at the collector electrode(s). The enhanced faradaic current at the generator can also be viewed as resulting from the steeper concentration gradient[8] caused by the nearby oppositely biased collector that regenerates the depleted redox form. Thus, there is a higher flux of active form to the generator. Also, a higher efficiency of collection generally leads to steeper concentration gradients and more amplified current.[2, 3, 8]

The amplification factor[2, 9-14] is defined as the ratio of the generator current when the collector electrode is biased (on) in redox cycling mode, $i_{G/C}$, to that when the collector electrode is at open circuit potential (off), i_G,

$$A_F = \frac{i_{G/C}}{i_G} \quad (1)$$

Collection efficiency[2, 9-13, 15] (C_e) is defined as the capacity of the collector to convert the total generator product back to its starting redox form. It can be calculated by dividing the current obtained at collector (i_C) by the current at the generator in the presence of redox cycling.

$$C_e = \frac{i_C}{i_{G/C}} 100\% \quad (2)$$

(Note that i_C with a capitol 'C' for the collector current is not to be confused with i_c with a lower case 'c' for the charging current.)

The concept of redox cycling originated from early studies with rotating ring disk electrodes (RRDEs),[16-19] where the disk serves as the generator and the ring as the collector. Transfer of the generated species across the gap to the collector results from convection caused by rotation. Redox cycling is also suitable for miniaturized systems, where the gap is so small that diffusion alone can transfer the generated species to the collector efficiently. Redox cycling offers improved signal-to-noise ratio, better temporal resolution (≤ several hundred milliseconds) and minimized charging currents compared to transient techniques. The concept has been used in flow cells, reversal electrolysis, study of homogenous reactions coupled to electron transfer, liquid chromatography, capillary zone electrophoresis and flow injection methods.[4, 8, 20-24] The concept can also be used to discriminate between electrochemically reversible and irreversible compounds by holding the two electrodes at selectively different potentials.[2, 3, 25-28] Thus, it is of

interest to study the fundamentals of redox cycling and understand the conditions leading to optimum currents at the generator and collector elements.

The existing literature for band and ring electrodes reports different limiting diffusional regimes using simulations and computational studies. Microelectrodes are especially of interest due to enhancement in current density as a result of strong edge effect. Niwa and co-workers have studied redox cycling at microband arrays of different dimensions extensively.[2, 3, 23, 24, 27, 29-33] A vast literature is available for analysis on diffusional mass transfer under quasi steady state and steady state conditions, chronoamperometry, linear sweep voltammetry, chronopotentiometry and electrode kinetics at microbands.[34-43] Amatore and Compton and co-workers have studied diffusion regimes at thin film-coated microband electrodes and channel microbands under laminar flows. They have also modeled redox cycling using dual microband electrodes as well as arrays.[44-53] Microring electrodes having small thickness as well as small radius are of interest for studying fast reaction kinetics due to the uniform accessibility of their surface to redox species. Amatore has explored the diffusion at microrings for varying combinations of thickness and time scales using conformal mapping.[54] Microrings provide a link between hemicylindrical symmetry (for microbands) at short time scales ($w/r_o = 0.05$; w = width and r_o = outer radius of the electrode) and hemispherical symmetry (for microdisks) at long time scales ($w/r_o = 0.5$) when the diffusion layer exceeds the microring's outer radius. Predictions of current for microrings has been performed using computer simulations for quasi steady state and steady state responses and for coupled chemical reactions, as well as for techniques such as ac impedance, cyclic voltammetry, and chronoamperometry.[54-64] Also, two-electrode, microring-disk systems have been evaluated under redox cycling conditions.[4, 6, 18] However, redox cycling has not previously been explored at an array of concentric microrings.

Clearly, electrode geometry plays an important role in redox cycling. The studies herein compare redox cycling at individually-addressable MEAs of parallel microband electrodes with that at concentric microring electrodes. In the latter, various selections of rings having different diameters, different effects of overlapping diffusion layers for a given time scale, and different generator and collector assignments are possible. The investigations are especially unique in that they explore current responses at and contributions of individual elements comprising the generator and collector involved in redox cycling, which heretofore has not been investigated. Finally, the ability to vary different assignments of different geometries of generator and collector electrodes might lead to improved designs for redox cycling.

2.3 EXPERIMENT

2.3.1 Chemicals and materials. Hexaammineruthenium (III) chloride (Alfa Aesar, MA, USA) and potassium chloride (EMD Chemical Inc., Darmstatd, Germany), both ACS grade, were used as received. Water, ACS reagent grade (≥ 18 MΩ-cm), was obtained from Ricca Chemical Co. (Arlington, TX).

2.3.2 Electrochemical studies. Experiments were carried out in triplicates on the same device throughout the study. To avoid compositional changes due to electrochemistry from one experiment to another, fresh solution was used each time. All electrochemical experiments were performed using cyclic voltammetry (CV) with a multipotentiostat equipped with a faraday cage that could accommodate up to eight working electrodes (CHI 1030, CH Instruments, Austin, TX).

For redox cycling experiments, current at both the electrodes were plotted as a function of potential at the generator. The potential range was swept at the generator (from +200 mV to –

300 mV and back) and the collector was held at a constant potential (+200 mV) versus Ag/AgCl (saturated KCl) reference electrode. In order to determine the amplification factor, CV was performed with the same generators, but with the electrodes assigned as collectors left at open circuit. In all experiments (except for the calibration curves) a 5.0 mM solution of $Ru(NH_3)_6Cl_3$ in 0.5 M KCl electrolyte was used. Experiments were performed with 4 mL of solution, contained by a polyimide reservoir (2 cm width x 2 cm length x 1 cm height) placed onto the horizontally-oriented chip. The seal with the chip did not leak. A platinum wire auxiliary electrode and Ag/AgCl (saturated KCl) reference electrode were carefully inserted into the solution and located distant from the array to avoid interference and held by a dual clamp. Unless otherwise stated, all currents reported in this manuscript are the absolute values of the difference between the peak or steady state current, whichever is larger, and the charging background. Generator current is cathodic and collector current is anodic. Small scan rate was chosen to provide long time scale for redox species to diffuse to the neighboring electrodes and improve collection at collector electrodes. Effect of varying the number of generator - collector pairs on amplification and on collection efficiency was studied using the band microelectrode array. Effect of varying the gap between the generator and collector electrodes on amplification and collection efficiency was also studied using the band microelectrode array.

Different assignments of generator and collector electrodes were investigated in redox cycling experiments: alternating generators and collectors where the outermost electrodes are collectors (configuration 1a) and where the outermost electrodes are generators (configuration 1b); one outermost generator with multiple collectors to one side (configuration 2a) and two outermost generators with multiple collectors on the inside (configuration 2b); one innermost generator with multiple collectors to one side (configuration 3, microrings only); one central

generator with multiple collectors on both sides (configurations 4a and 4b); and one innermost and one outermost generator electrode that flank multiple central collectors between them (configuration 5). For each configuration, all microelectrodes composing the generator were shorted together and polarized at the primary working channel of the potentiostat. Microelectrodes composing the collector were polarized individually at seven different secondary channels but at the same potential. This allowed the monitoring of the unique current responses of microelectrodes forming the collector. Configurations where there are more than seven collector elements are shorted symmetrically. The following electrodes are shorted together for configuration 2a: 5 - 18, 6 - 17, 7 – 16, 8 – 15, 9 – 14, 10 – 13, and 11 – 12. The following electrodes are shorted together for configuration 4a: 3 - 17, 4 - 16, 5 – 15, 6 – 14, 7 – 13, 8 – 12, and 9 – 11.

2.3.3 Design and fabrication of MEAs. The MEA devices are shown in Figure 2.1. They contain 18 coplanar band or 17 ring gold electrodes, one large gold feature (4.00 mm x 2.00 mm) that served as an on-chip quasireference and one large feature (4.00 mm x 4.00 mm) that served as an auxillary electrode. Each of the working electrodes in the array is individually addressable via contact pads. The microbands and microrings have an average width of 4.0 ± 0.1 μm and are separated by 4.0 ± 0.1 μm gaps. The parallel microbands have a length of 2.00 ± 0.01 mm and essentially identical areas of $0.8 \times 10^{-4} \pm 0.001$ cm^2. The individually-addressable rings are interrupted by a wedge of insulator to cover the leads. Table 2.1 lists the measured diameter and the calculated electrode areas of each microring, taking into consideration the wedge.

The coplanar MEAs were fabricated using a conventional photolithographic procedure described previously[65] with the minor modifications described below. In brief, a 50 nm thick

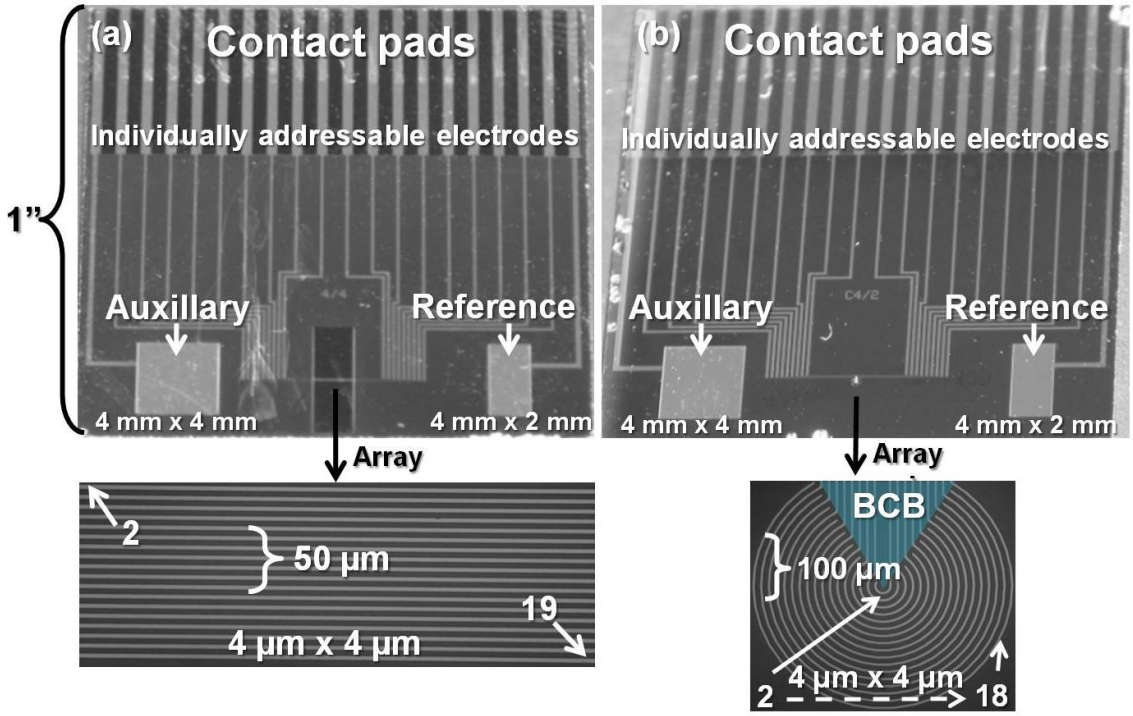

Figure 2.1. Photographic images showing a full view and an expanded view of the array region of a (a) parallel band and (b) concentric ring MEA. Larger electrodes used as on-chip quasireference and auxillary electrodes are also shown in full views. The rings are not complete circles due to the presence of connection lines covered by the insulator, benzocyclobutene (BCB). Number *1* is designated to the auxillary electrode in each array and number *20* to the quasireference electrode. The smallest ring electrode (the central disk) is absent due to a fabrication defect. Hence, the ring MEA contains only 17 rings numbered from *2* to *18*. The parallel microbands are numbered from *2* to *19*, with the auxillary and quasireference electrodes numbered as *1* and *20* respectively.

Table 2.1. Details of dimensions and current at ring MEAs. Current was based on CV responses at 0.10 V/s in 5.0 mM $[Ru(NH_3)_6]^{3+}$ and 0.5 M KCl electrolyte.

Electrode[a]	Inner Diameter[b,c] / μm	Electrode Area[d] / 1 x 10^{-4} cm^2	Current[e,c] / nA	Current Density[f] / mA cm^{-2}
2	6	0.0134	9.8	7.3
3	14	0.0264	14.2	5.4
4	22	0.0435	24.9	5.7
5	30	0.0603	36.3	6.0
6	38	0.0772	46.6	6.0
7	46	0.0940	57.3	6.1
8	54	0.1107	67.8	6.1
9	62	0.1275	76.5	6.0
10	70	0.1443	90.1	6.2
11	78	0.1611	95.9	6.0
12	86	0.1779	112.0	6.3
13	94	0.1947	119.0	6.1
14	102	0.2114	128.0	6.1
15	110	0.2282	141.0	6.2
16	118	0.2450	148.0	6.1
17	126	0.2618	165.0	6.3
18	134	0.2786	175.0	6.3

a. Electrodes increase in number from inner to outer ring. They are labeled in Figure 2.1.
b. Inner diameters are actual measured values.
c. The standard deviations for the current values vary from ± 0.01 – 0.05 nA for the pooled data from 3 repetitions on a single electrode and 10 chips.
d. Ring electrode area is calculated from the measured width of rings and their inner diameter and subtracting out the insulating wedge, as follows: $\pi(r_{outer})^2 - \pi(r_{inner})^2 - C\pi/360^o[(r_{outer})^2 - (r_{inner})^2]$ where C is the central angle. The error is that which is propagated from the inner diameter and from the width of the electrode.
e. The current is that of the plateau or peak of the cathodic wave of the CV response minus the charging background current at that potential.

f. The current density is calculated by dividing the measured current by the calculated electrode area. The standard deviations for the current density values vary from ± 0.010 – 0.049 mA/cm^2 for the pooled data from 3 repetitions on a single electrode and 10 chips. The error is that which is propagated from the error in the measured current and the error from the calculated area of the electrode.

layer of gold was deposited onto a 5 nm thick chromium adhesion layer on a silicon-dioxide coated (2 μm) silicon wafer. (Thicknesses are based on the readings of the piezoelectric crystal thickness monitor on the thermal evaporator that was used to deposit the metals.) After patterning the metal layers to define electrodes, leads and contact pads, MEAs were encapsulated by an insulation layer (formed by the polymer benzocyclobutene (BCB)) and subsequently patterned to open up the active electrode areas that would be exposed to solution and the contact pads that would be inserted into the edge connector (solder contact, 20/40 position, 0.05 in. pitch, Sullins Electronics Corp., CA).

A different photoresist (S1805) was used this time to achieve better spatial resolution required for the small feature size. Due to low viscosity, and thus smaller thickness obtained for the photoresist, the exposure time was greatly reduced from 35 s to 2 s for patterning of the gold features through a chrome mask. The etching time for the Au and Cr layers was also reduced to 5 s each.

The metal layers were deposited on the wafer with an Edwards 306 Auto thermal evaporator. The wafer was spin-coated with photoresist (S1805) at 6000 rpm to form a uniform thickness of the film. The photoresist was patterned by exposure through a Cr mask for 2 s. The Au and Cr layers were then etched for 5 s each by wet etch processes.

To form the insulating layer, the wafer was spin-coated with the photosensitive BCB solution and then exposed through a mask with 350 nm UV light. The regions of unexposed BCB were then dissolved away using BCB developing and rinsing solutions. A descumming procedure was then performed on the arrays using reactive ion etching (mixture of O_2, 36 sccm and SF_6, 4 sccm at 300 mT and 300 W rf power applied for 13 minutes).

2.4 RESULTS & DISCUSSION

2.4.1 Characterization of MEAs. Each microelectrode in a band and ring MEA was characterized by CV in 5.0 mM $[Ru(NH_3)_6]^{3+}$ redox solution and 0.50 M KCl electrolyte at 0.10 V/s and 0.01 V/s scan rates. Figure 2.2 shows examples of responses of both geometry at 0.10 V/s scan rate. The electrochemical response of microband electrodes showed high reproducibility within the array (3.8% relative standard deviation, RSD, 15 electrodes) and from array to array (pooled 8.5% RSD, 10 chips, 15 electrodes each). Because the microrings have varying diameters, their electrochemical signal is compared in terms of current density (normalized to electrode area) throughout this paper. The current density of microring electrodes showed 3.8% RSD (N=15) within the array and pooled 8.4% RSD from array to array (10 chips, 15 electrodes each). These results suggest that the fabrication procedures are equally precise for planar and circular geometry. They also imply that the current density is also a good a way to compare electrochemical response for different sized rings and between band and ring geometries.

Equations for predicting steady state current achieved at long time scales are well established for band and disk geometry.[8] The most accepted exact solution for the rings was provided in 1951 by Smythe.[66] These equations (shown below) are used to predict the responses at long time scales and were derived for a solution where only the oxidized form of the redox species is in the electrolyte at 25 ºC,

$$i_{band} = \frac{2\pi mFADC_o}{w\ln[\frac{64Dt}{w^2}]} \quad (3)$$

$$i_{disk} = 4nFDC_o r \quad (4)$$

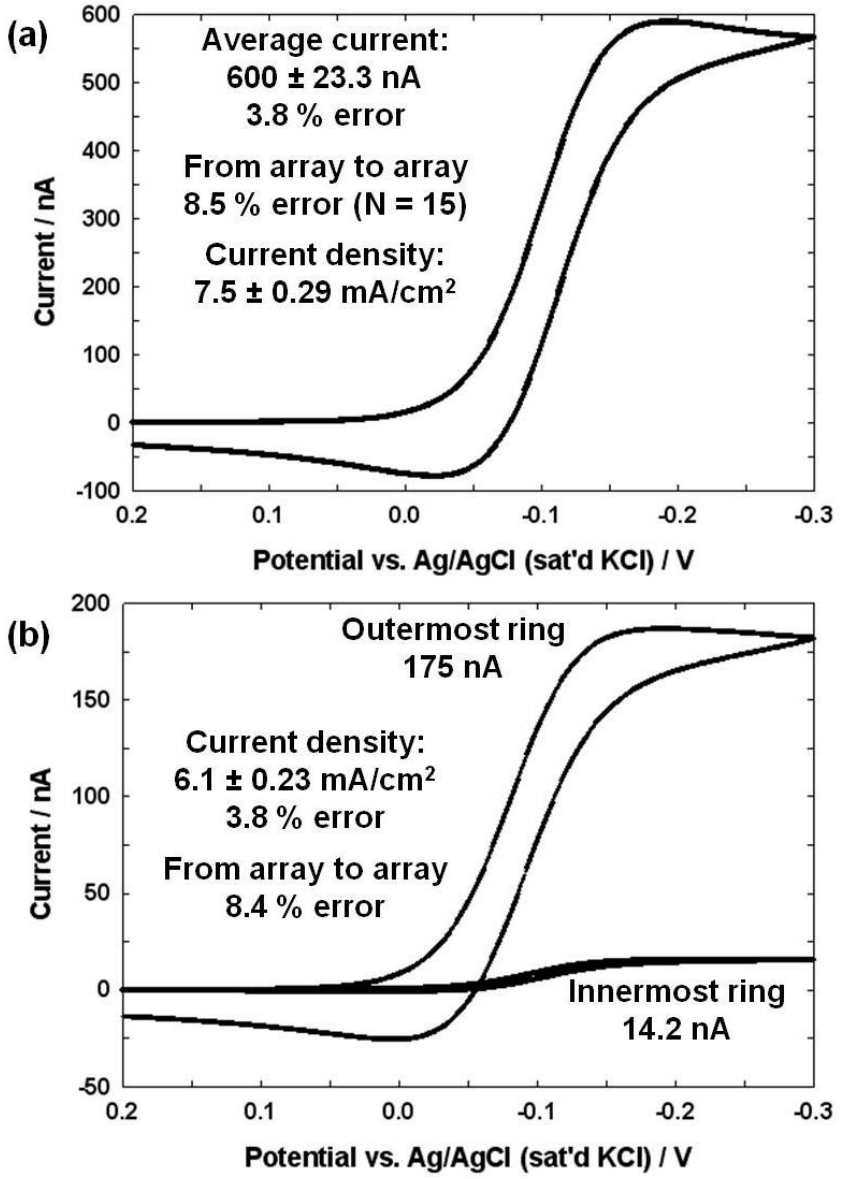

Figure 2.2. Averaged CV responses for (a) 18 microbands in a MEA, and examples of individual responses for (b) the outermost and the innermost microrings contained in a MEA in a solution of 5.0 mM $[Ru(NH_3)_6]^{3+}$ and 0.5 M KCl at 100 V/s scan rate. The averaged electrochemical response for the microbands was obtained by dividing the summation of current obtained at each microband in the array at each data each point on the potential axis by the total number of microbands. RSD values were obtained from multiple electrodes and chips as described in the text.

$$i_{ring} = \frac{nFDC_o\pi^2(r_o + r_i)}{\ln(16(r_o + r_i)/(r_o - r_i))} \quad (5)$$

where A is the area, D is the diffusion coefficient, C_O is the bulk concentration of the oxidized form of the redox species, w is the width of the electrode, t is the time that the potential is poised at a reducing potential well past E°, r_o is the outer and r_i is the inner radius of the ring electrode. Experimental data is compared with the theoretical predictions in table 2.2. The closest predictors to the experimental currents are Eq. 3 for the bands and Eq. 5 for rings of all sizes, and further explained below.

The microbands exhibit peak-shaped behavior at short time scales and sigmoidal behavior at long time scales. At short times scales, the root mean squared distance that a molecule diffuses, is less than the width (the smallest dimension of the electrode), and $Dt/w^2 << 1$.[8] Thus at 1.00 V/s, where t is 0.50 s (the time it takes to scan from E° to the switching potential), w is 4.0 x 10^{-4} cm and D is 7.8 x 10^{-6} cm^2/s, $Dt/w^2 = 0.24$. Thus, linear diffusion dominates mass transfer. At long time scales, when the distance molecules diffuse exceeds the smallest electrode dimension ($Dt/w^2 >> 1$), radial diffusion dominates mass transfer. The value of Dt/w^2 at 0.01 V/s (t = 50 s) is 2.44 x 10^3 and quasi steady state behavior (due to hemicylindrical symmetry) is observed and predicted by Eq. 3 at long time scales.

The larger microrings also show peak behavior at short time scales (e.g. 1.00 V/s where $Dt/r_o^2 << 1$) and sigmoidal behavior at slow time scales (e.g. 0.01 V/s where $Dt/r_o^2 >> 1$). For the smaller rings however, radial diffusion dominates at all time scales studied (0.01 V/s - 1.00 V/s) due to their small size. The largest ring in the array (ring 18) has a w/r_o value of 0.03. It should exhibit thin ring behavior similar to a looped band. Both the experimental current density and the theoretical value obtained using Eq. 5 are much closer to the values for a band than those for

Table 2.2. Electrochemical responses for band and ring electrodes based on CV responses in 5.0 mM $[Ru(NH_3)_6]^{3+}$ and 0.5 M KCl electrolyte 0.01 V/s. Theoretical values calculated for band, ring and disk geometry a long time scale using the equations 3-5. The data reported in current density (current divided by the electrode's area, i_d).

	L or r_o / cm	Calculated A/ 1 x 10^{-4} cm^2	Exp i/ nA	Exp i_d/ mA cm^{-2}	Theoretical i/ nA	Theoretical i_d[b] / mAcm^{-2}
Band	0.20	0.80	451.9	5.65	459.4	5.74
Ring 18	0.013	0.28	170.0	6.10	164.3	5.90
Ring 2	0.0010	0.013	9.64	7.19	16.67	12.44
Disk	0.013	0.28			235.3[a]	8.45[c]
Disk	0.0010	0.013			17.6[a]	14.16[c]

a. The current values for the disk are the predicted values calculated using equation 4 at long time scales and the same outer radii as those for the rings i.e. either 0.013 cm or 0.0010 cm.
b. The theoretical current density values calculated by first calculating the current values using equation 3-5 at long time scales and then dividing those by the respective electrode area.
c. The theoretical current density for the disk are calculated using the same area as for the rings i.e. either 0.28 x 10^{-4} cm^2 or 0.013 x 10^{-4} cm^2.

disk. Thus the bigger ring follows hemicylindrical symmetry for the given time scale. The smallest ring (#2) has a w/r_o value of 0.4, and is expected to exhibit disk behavior, which is also predicted by Eq. 5. However, for the given time scale it follows a diffusion profile that is between that of band geometry (similar depletion of the diffusion layer along both edges because of the lack of curvature) and disk geometry (depletion across the center between the opposites sides of the circle).

The average current density of microbands (7.5 ± 0.3 mA/cm^2) is greater than for microrings (6.1 ± 0.2 mA/cm^2) at 0.10 V/s. This is a result of the difference in the circular and the linear geometry of the electrodes. The diffusion layer on the inner edge of a ring overlaps with itself from one side to the other, resulting in depletion of redox species. Thus microrings are able to shield better due to their circular geometry. A greater overlap of diffusion layers should also provide greater amplification when the redox cycling is turned on adjacent electrodes inside the ring. Thus, we expect to obtain more efficient redox cycling and thus better detection limits for redox species interior to rings than at bands.

2.4.2 Capacitance study. There is always a concern about the quality seal of between the insulator and the fabricated electrodes on a device. An imperfect seal would become increasingly troublesome with decrease in active electrode area. Due to the small area of the IDA electrodes, it is important to test the quality of the seal. This is accomplished by comparing the capacitance of these microelectrodes with those of the macro electrodes. The capacitance (C_d) is determined by dividing the charging current (i_c), measured at 0.0 V with the area (A) of the electrode and the scan rate (υ) at which the charging current is obtained.

$$i_c = \upsilon A C_d \qquad (1)$$

The capacitance (normalized) is independent of the scan rate. Therefore, careful analysis of the capacitance as a function of the scan rate provides insights on the electrode area as well as quality of the seal with the insulator. The scan rate study on the electrodes of different sizes was conducted in 0.1 M KCl electrolyte using Ag/AgCl (saturated KCl) reference electrode. The capacitance was determined using equation 1. Figure 2.3 shows the log-log plot of the normalized capacitance versus scan rate for macro and micro electrodes.

The micro electrode shows similar variation in capacitance as does the macro electrodes, they all have the same slope (0.08 $\mu F/cm^2$). The capacitance of macro as well as micro electrodes shows negligible variation with scan rate. If there would be an imperfect seal between the insulator and the electrode surface, the slope of the log-log plot for the microelectrode would be much greater than that of the macroelectrodes. This is due to the smaller iR drop at slower scan rates than at fast scan rates. Thus, the voltage change in the cracks of an imperfect seal is greater at slower scan rates. The area in the cracks also contributes to the charging current and the total electrode area seems much bigger than the actual area.

It is therefore concluded that the insulator has a good seal with the surface of the electrode. It is to be noted however, that the slopes of the all electrodes with varying area are parallel, but offset by a factor. The exact reason for this is not known at this time. One of the reasons could be underestimation of the area, but this cannot account for the entire offset for each plot.

2.4.3 Redox cycling with different numbers of generator and collector electrodes. This experiment was carried out on large feature band microelectrode arrays (w = 25 µm, g = 25 µm) previously available in the Fritsch's laboratory. The table 2.3 shows that 1 G – 12 C provides highest amplification and collection efficiency for generator flanking collector

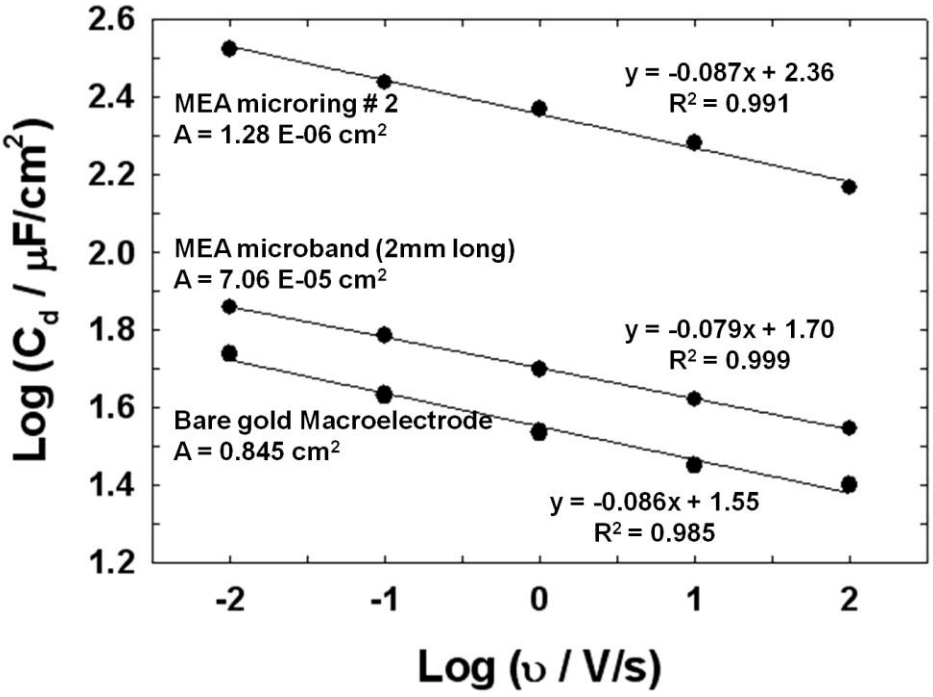

Figure 2.3. Plots of the log of the normalized capacitance versus the log of the scan rate at which the capacitance was determined for the smallest ring (#2) contained in the ring MEA, for a single microband electrode contained in the ring MEA, and for the bare, gold macroelectrode.

Table 2.3. Comparison of redox cycling parameters (amplification (A_F) and collection efficiency (C_e)) for two different arrangements of generator collector pairs: increasing number of collector electrodes flanking the generator and increasing number of alternating generator collector pairs in 5 mM $Ru(NH_3)_6^{3+}$ at 0.01 V/s scan rate obtained at 25 µm (w and g) microband electrodes contained in a MEA is shown. The area normalized collection efficiency at the collector provides a good comparison of the different electrode arrangements independent of their area. i_G is CV current, $i_{G/C}$ is the generator current during redox cycling and i_C is the collector current.

N of G / C	**Arrangement**	**i_G**	**$i_{G/C}$**	**i_C**	**A_F**	**C_e**
		nA	**nA**	**nA**		**%**
1 / 1	l l	60.3	66.2	17.2	1.2	32.6
1 / 6	l l l l l l l	60.3	68.3	52.7	1.3	70.8
1 / 12	l l l l l l l l l l l l l	60.3	69.5	52.3	1.3	73.7
2 / 3	l l l l l	97.6	130.8	83.0	1.4	60.6
3 / 4	l l l l l l l	151.7	237.7	142.3	1.6	57.8
7 / 7	l l l l l l l l l l l l l l	296.1	416.2	265.8	1.5	63.6

arrangement and that 7 G – 7 C provides best results for alternate generator - collector arrangement of electrodes. The absolute current magnitude of both the generator and the collector electrode decreases in flanking electrode arrangement compared to the alternate arrangement of electrodes. Amplification and collection efficiency are also higher for the alternate generator – collector arrangement of electrodes than the flanking arrangement. Lower current magnitude at the electrodes would provide poorer detection limits for the analyte (the ultimate goal of this project) due to higher signal to noise ratio. Thus, the alternate arrangement of electrodes should be most suitable for better detection limits.

2.4.4 Effect of varying the number of generator – collector pairs on amplification and collection efficiency. This experiment was carried out on small feature band microelectrode arrays (w = 4 µm, g = 4 µm). Table 2.4 lists the current obtained at the generator with and without redox cycling and at the collector for different numbers of electrode pairs. Figure 2.4 shows the effect of varying the number of pairs on amplification and collection efficiency. Current at the generator with and without redox cycling and at the collector increases linearly with the increasing number of generator – collector pairs from 1 to 9. There is not much improvement in the amplification and the collection efficiency from 6 to 9 pairs of electrodes. Comparison of results from 25 µm features and 4 µm features shows an increase in collection efficiency due to decrease in interelectrode gap and electrode width. This tell us that although the amplification and collection efficiency have observed a saturation point from 8 to 9 pairs of microelectrodes, the combination of decrease in the gap and width of the microelectrodes along with increase in number of generator – collector pairs will provide further improvement.

2.4.5 Effect of varying the gap between the generator and the collector on amplification and collection efficiency. This experiment was carried out on small feature band

Table 2.4. Comparison of amplification (A_F) and collection efficiency (C_e) for varying number of generator - collector pairs during redox cycling in 5 mM $Ru(NH_3)_6^{3+}$ at 0.01 V/s scan rate obtained at 4 µm microband electrodes contained in a MEA is shown. i_G is CV current, $i_{G/C}$ is the generator current during redox cycling and i_C is the collector current.

Pairs	**i_G**	**$i_{G/C}$**	**i_C**	**A_F**	**C_e**
G/C	µA	µA	µA	-	%
9/9	1.52	4.84	4.05	3.2	83.7
8/8	1.43	4.45	3.71	3.1	83.3
6/6	1.19	3.36	2.73	2.8	81.2
4/4	0.92	2.22	1.72	2.4	77.5
2/2	0.60	1.12	0.73	1.9	65.4
1/1	0.43	0.58	0.26	1.3	45.0

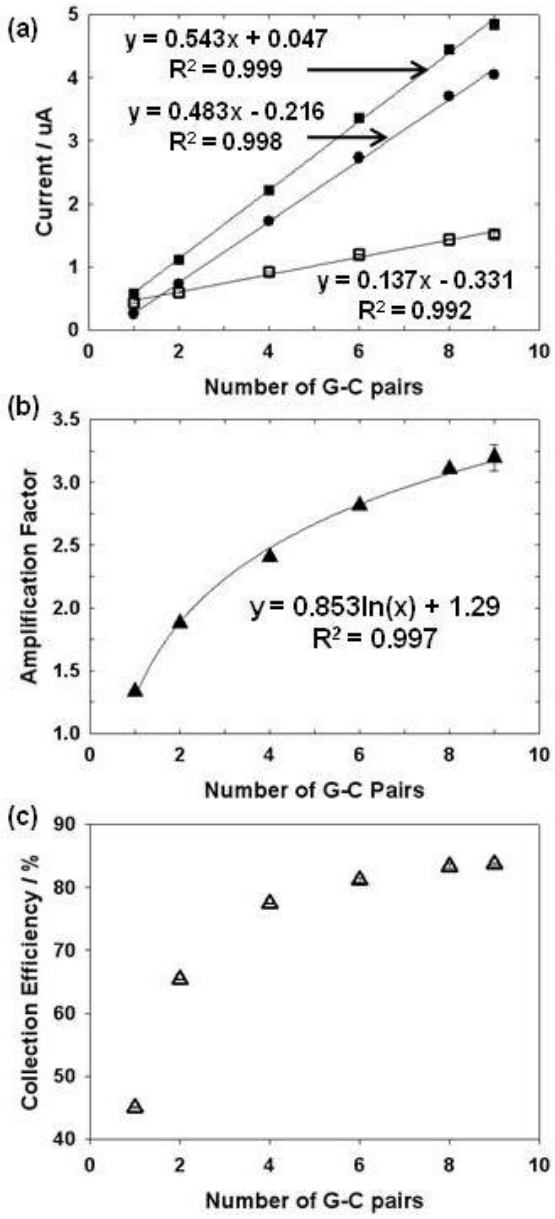

Figure 2.4. Effect of varying the number of generator – collector pairs on redox cycling is shown. (a) Faraday current at the generator with redox cycling (closed squares), collector (closed circles), and at the generator without redox cycling (open squares) increases linearly with the number of generator collector pairs. The slope for (b) amplification and (c) collection efficiency decreases with the increase in number of generator collector pairs.

microelectrode arrays (w = 4 μm, g = 4 μm). Table 2.5 lists the current obtained at the generator with and without redox cycling and at the collector for different numbers of electrode pairs. Figure 2.5 shows the effect of varying the gap between the generator and the collector on amplification and collection efficiency. This repetitive electron transfer between the two states of a redox species during a redox cycling experiment leads to the amplification at the generator. Since only one pair of generator – collector is used here, the amplification is small. The collection efficiency stays constant at 25 % up to 28 μm of gap between the generator and the collector. For smaller gaps the collection efficiency increases linearly with the decrease in interelectrode spacing.

2.4.6 Redox cycling experiments with different configurations

2.4.6.1 Amplification. Tables 2.6 and 2.7 list amplification factors for the different electrode configurations for band and ring MEAs, respectively. Alternating generator–collector arrangements (C1a and C1b) give the highest amplification factor during redox cycling, which increases the generator sensitivity. It is the typical configuration reported in literature,[2, 7, 14, 25, 30, 67, 68] where enhancement in generator current is usually the ultimate goal. This is true for both geometries, band and ring ($A_F > 2$). In the alternating arrangement, the gap between every generator and every collector is at a minimum (4 μm). As a result, the redox molecule has to travel the minimum distance to recycle, maximizing the number of redox cycles and thus the amplification. Species that are reduced at collectors distant from the originating generator do not have to diffuse back to it to be regenerated, because there is always a generator nearby. The other configurations, in contrast, where the gap between a single generator and the multiple collectors increases as the collectors flank the generator outward, the redox species are lost to the bulk solution and the number of redox cycles is decreased, lowering the amplification.

Table 2.5. Comparison of amplification (A_F) and collection efficiency (C_e) for varying gaps between generator and collector electrode during redox cycling in 5 mM $Ru(NH_3)_6^{3+}$ at 0.01 V/s scan rate obtained at 4 µm microband electrodes contained in a MEA is shown. This experiment was carried out with one pair of generator-collector electrode. i_G is CV current, $i_{G/C}$ is the generator current during redox cycling and i_C is the collector current.

Gap	**i_G**	**$i_{G/C}$**	**i_C**	**A_F**	**C_e**
µm	nA	nA	nA	-	%
4	418.1	540.2	279.9	1.3	51.8
12	411.2	452.8	195.2	1.1	43.1
20	411.2	469.9	155.5	1.2	33.1
28	398.2	432.2	117.4	1.1	27.2
36	398.2	429.8	111.4	1.1	25.9
44	388.9	412.9	111.1	1.0	26.9

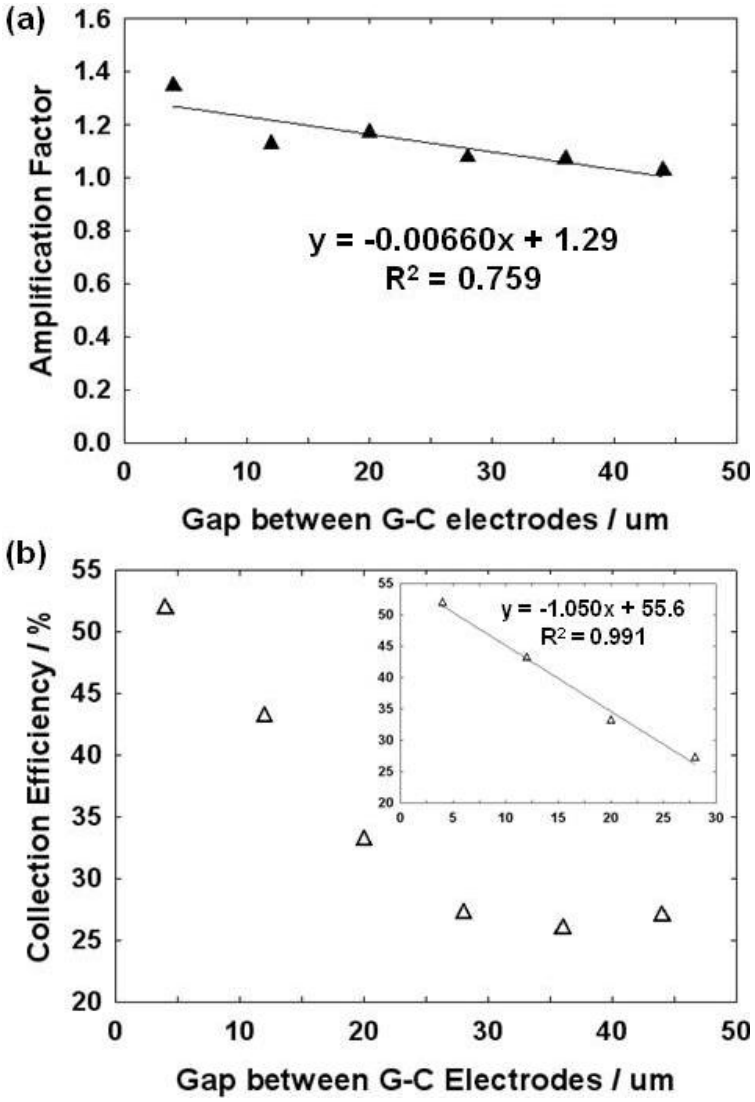

Figure 2.5. Effect of varying the gap between the generator – collector electrodes on (a) amplification and on (b) collection efficiency during redox cycling with one pair of generator collector electrodes is shown. For gaps < 30 μm the collection efficiency increases linearly with the interelectrode spacing.

Table 2.6. Calculated current densities (i_d) obtained from the raw data for redox cycling (obtained from a single chip, N = 5) at individual elements for different configurations of band MEA. The relative standard deviations are ≤ 0.5% for all current densities and ≤ 2.5% for amplification (A_F) and collection efficiency (C_e). Generator (all the elements shorted together) was polarized at working channel 1. Individual elements of the collector were polarized at channels 2-8. The electrode numbers for representing the collector elements correspond to those in figure 2.1. Collection efficiency was calculated from total current obtained at all the collector elements summed together. i_G is CV current, $i_{G/C}$ is the generator current during redox cycling and i_C is the collector current.

	i_{dG}	$i_{dG/C}$	i_{dC} at individual elements of the collector [a]							A_F	C_e [b]
	mA/cm^2				mA/cm^2					-	%
C1a					2	4	6	8	10		
	2.50	5.53	2.50	5.53	3.30	5.10	5.19	5.33	5.31	2.2	96.9
C1b					3	5	7	9	11		
	2.20	4.71	2.20	4.71	5.41	5.30	5.25	5.28	5.33	2.1	93.4
C2a					11	12	13	14	15		
	3.65	4.05	3.65	4.05	0.09	0.09	0.14	0.20	0.31	1.1	69.9
C2b					4, 17	5, 16	6, 15	7, 14	8, 13		
	4.01	4.80	4.01	4.80	1.92	0.71	0.36	0.24	0.18	1.2	76.6
C4a					3, 17	4, 16	5, 15	6, 14	7, 13		
	5.80	8.04	5.80	8.04	0.08	0.07	0.10	0.16	0.29	1.4	100.0
C4b					6	7	8	9	11		
	5.58	8.11	5.58	8.11	0.25	0.32	0.67	2.74	2.76	1.5	96.9
C5					7	8	9	10	11		
	5.11	6.85	5.11	6.85	3.45	1.00	0.61	0.50	0.60	1.3	77.3

a. The electrode numbers for representing the collector elements correspond to those in Figure 1.
b. Collection efficiencies were calculated from the total current obtained at all the collector elements summed together for a given electrode configuration.

Table 2.7. Calculated current densities (i_d) obtained from the raw data for redox cycling (obtained from a single chip, N = 5) at individual elements for different configurations of ring MEA. The relative standard deviations are ≤ 1.5% for all current densities and ≤ 1.0% for amplification (A_F) and collection efficiency (C_e). Generator (all the elements shorted together) was polarized at working channel 1. Individual elements of the collector were polarized at channels 2-8. The electrode numbers for representing the collector elements correspond to those in figure 2.1. Collection efficiency was calculated from total current obtained at all the collector elements summed together. i_G is CV current, $i_{G/C}$ is the generator current during redox cycling and i_C is the collector current.

	i_{dG}	$i_{dG/C}$	i_{dC} at individual elements of the collector[a]							A_F	C_e[b]
	mA/cm^2										
C1a			2	4	6			2	4	6	
	1.72	3.55	0.90	2.99	3.05	1.72	3.55	0.90	2.99	3.1	1.7
C1b			3	5	7			3	5	7	
	1.50	3.27	2.02	2.70	3.79	1.50	3.27	2.02	2.70	3.8	1.5
C2a			11	12	13			11	12	13	
	2.47	3.12	0.11	0.15	0.11	2.47	3.12	0.11	0.15	0.1	2.5
C3			3	4	5			3	4	5	
	1.36	1.98	0.42	0.10	0.04	1.36	1.98	0.42	0.10	0.04	1.4
C4a			3, 17	4, 16	5, 15			3, 17	4, 16	5, 15	
	2.70	3.45	0.04	0.05	0.07	2.70	3.45	0.04	0.05	0.07	2.7
C4b			6	7	8			6	7	8	
	2.66	3.26	0.20	0.23	0.46	2.66	3.26	0.20	0.23	0.5	2.7
C5			7	8	9			7	8	9	
	2.53	3.76	1.33	0.55	0.31	2.53	3.76	1.33	0.55	0.3	2.5

a. The electrode numbers for representing the collector elements correspond to those in Figure 1.
b. Collection efficiencies were calculated from the total current obtained at all the collector elements summed together for a given electrode configuration

The amplification of configuration C2b (A_F =1.20) is better than for C2a (A_F=1.11) of bands even thought the ratio of the collector to generator area is the same (7:1). C2a behaves similar to a single generator – collector experiment where the generator as well as the collector product gets similar opportunity to escape from the redox cycling. C2b behaves similar to the generator – collector – generator product where the collector is now enclosed inside the generator. The redox species enters greater number of redox cycles before diffusing to the bulk solution.

Configuration 4 of bands behaves similar to a simple collector–generator–collector situation. The width of each collector on either side of the generator is twice as much in C4a than in C4b and so is the ratio of the collector to generator area (14:1 for C4a and 7:1 for C4b). The redox species collected at the furthest collector elements rarely diffuse back to the generator to get recycled in C4a causing the amplification (1.4) to be lower than for C4b (1.5).

Configuration 2b for bands is similar to the configuration 5 for rings, except the ratio of the collector to the generator area is twice as much for C2b (7:1) as for C5 (3.5:1). This causes C5 to have greater amplification (A_F=1.3) than C2b (A_F=1.2). Essentially, the generators are closer together in C5, consistent with why the closer proximity of the generators in the alternating configuration (C1a and C1b) improve amplification, too. In addition, small ring generators experience more shielding than band electrodes, and therefore produce a more pronounced amplification when the collectors are turned on.

The amplification factor for configuration C1a where the collectors are the outermost electrodes is larger for bands (A_F=2.2) than for rings (A_F=2.1), but the opposite result was obtained for generators as the outermost electrodes, C1b (bands at A_F=2.1, rings at A_F=2.2). For most of the configurations, (C1b, C2a, C3, and C5), the rings exhibited a higher amplification

factor than the bands. The main reason is that the rings exhibit greater shielding effect than the bands because of the curvature and cross-center depletion of redox species, thus the denominator of Eq. 1 is smaller, enhancing A_F. The exceptions are (C1a, C4a, and C4b).

The amplification for the C3 configuration of rings (A_F=1.5) is greater than that for C2a of bands (A_F=1.1). Here, all of the collector elements are on one side of a single generator electrode. In the case of the rings, C3, the collector elements are all exterior to the generating ring. Thus, the collector-to-generator area is very large; compare 40:1 for C3 rings to 7:1 for C2a bands. The outer collector rings in C3 enclose the generator, collecting most of the generated species as opposed to the greater escape of the generated species to the bulk solution in the linear band geometry.

2.4.6.2 Collection efficiency. Tables 2.6 and 2.7 list collection efficiencies for the different electrode configurations for band and ring MEAs, respectively. A generator flanked by collectors on both sides has the steepest concentration gradient. This is also predicted by digital simulations. One generator flanked by two collectors on both sides provide better collection efficiency than one generator one collector experiment.[9, 12, 13] Because every generator in configuration 1a is flanked by collectors on both sides, high collection efficiency is obtained (C_e = 96.4% for bands, 83.5% for rings). A notable decrease is observed even when just the outermost generators of the array lack a flanking collector, as in configuration 1b (C_e = 93.4% for bands, 77.3% for rings).

Configuration 4 gives the highest collection efficiency of all configurations investigated for both bands and rings, because the generator product is essentially quantitatively consumed due to a large collector area compared to the generator area, and which resides on both sides of the generator. Configuration C4a (C_e=100.0% for bands, 99.8% for rings) offers a higher

collection efficiency than C4b (C_e=96.9% for bands, 99.0% for rings), because there are more active collector elements in C4a.

Likewise, the collection efficiency of configuration C2b with a generator on both sides of the collector area (C_e=76.6%) is 9% greater than that for C2a with a generator on only one side of the collector area (C_e=69.9%) for bands. Although the collector area-to-generator area ratio is the same for both configurations, the one with the larger total collector area, which is accessible by species generated at both generators, still produces the larger collection efficiency.

However, when the two flanking generators are brought closer together from configuration C2b to C5 for bands, the collection efficiency increases further (from 76.6% to 77.3%, albeit only a 1% improvement), even though there is actually a factor of two decrease in the generator-to-collector area ratio. The actual collection efficiency of *individual* collector elements when there are larger numbers of collectors decreases because the generated species that get past the first collector element are depleted by the subsequent neighboring collectors. Otherwise, the generated species has a chance to return to the previous collector and be converted there. Thus, there are diminishing returns with larger collector regions, especially if they are flanked by generators, where species can. This comparison of C2b with C5 highlights the diminishing effect of having too many collectors.

Most of the comparisons of collection efficiency thus far have been for different configurations of band electrodes. A comparison of similar configurations for the ring electrodes exhibits a similar trend. However, the C4b configuration is one of two configurations where the rings actually produced higher collection efficiency than the bands, even though the relative collector-to-generator area is smaller for the rings (6.5:1) than for the bands (7.0:1). A reason for this phenomenon is not obvious at this time, but it might have something to do with the

efficiency of collecting generating species from rings interior to the generator across the center and also from the ends of the generator ring by collectors on the opposite side of the wedge. The loss of redox species at the ends of the band generator is a small fraction of the total generated species because the band length is 500 times the width. However, that ratio is only ~95 for the generator in C4b. The other configuration where collection efficiency is greater for rings than bands is C3 (rings, 88.3%) compared to C2a (bands, 69.9%). The reason for this is the same as that described above for C3's greater amplification over that of C2a.

2.4.6.3 Current and current density. Figure 2.6 shows the combinations of generator and collector electrodes for different configurations and a visual representation of the current densities at individual elements in a given set of collectors. Tables 3 and 4 provide a numerical list at each configuration for band and ring MEAs, respectively. The current densities for bands are larger than for rings *in general*. Less shielding of diffusion layers in band MEA compared to that in ring MEA allows the generator band to generate more product. Because the generators produce more current density, therefore, the collectors also exhibit larger current density due to the greater influx of the generated species at the collector electrode. The collectors closest to the generator exhibit larger current densities than those farther away because they collect the species *before it is diluted out* into the surrounding volume. Collectors farther away, capture a lower *concentration* of generated species. This trend is clearly observed with bands (C2a, C2b, C4a, and C4b) as well as with rings (C2, C3, C4a, and C4b). Figure 2.7 shows a very clear and distinct decrease in the current density of collector elements for various configurations of band and ring geometry as the elements get further away from the generator.

The current density for bands also reflects their relative current efficiencies, but this is not true for rings. Also the current density and the efficiency for the collector bands on either

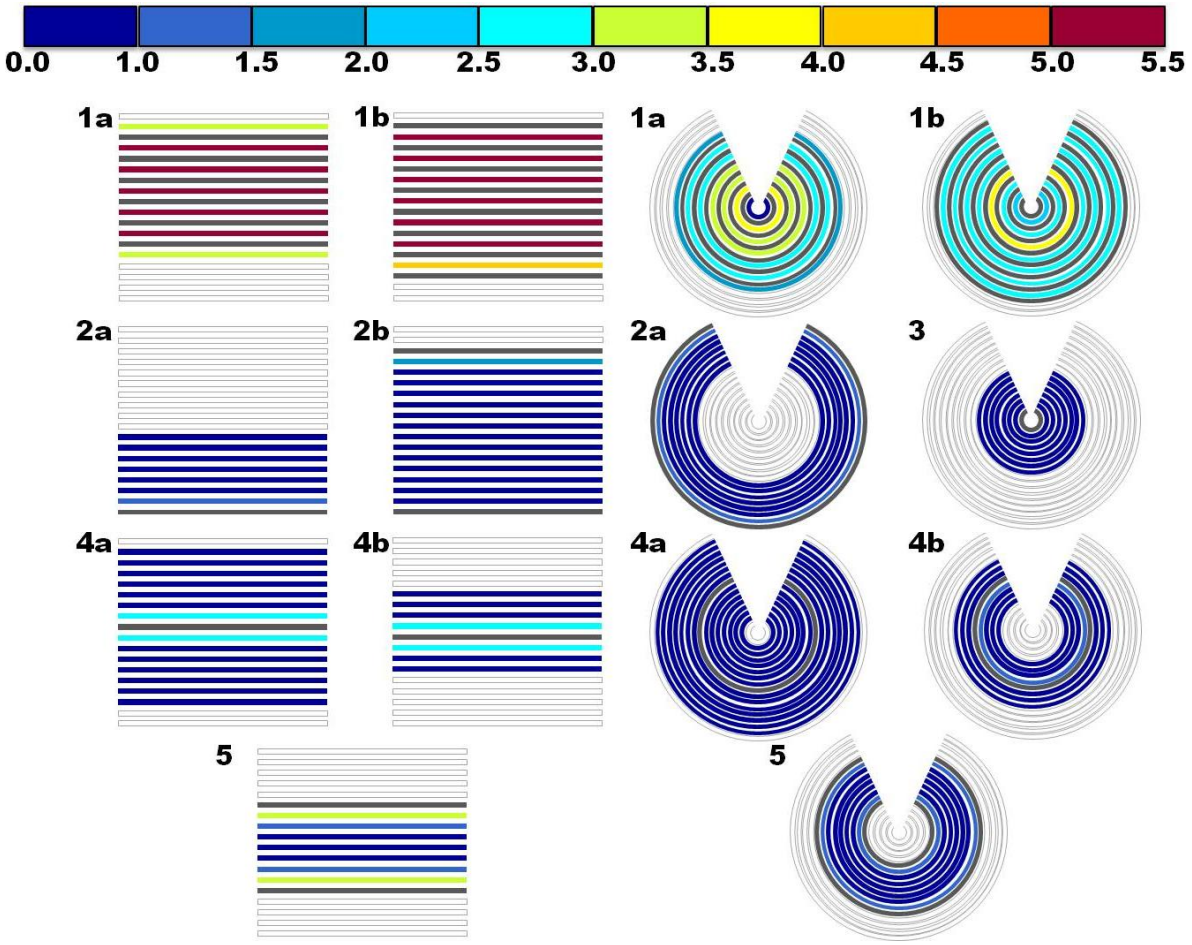

Figure 2.6. Representation of the different electrode assignments for configurations 1-5 at parallel band and concentric ring MEAs and the corresponding color charts showing current density (mA/cm^2) at the collector elements during redox cycling. The numbers next to each figure represents the configuration number. The multi-colored bar at the top is the color scale for the current densities. All the generator elements (shown in grey) are shorted together to compose a single generator working electrode. All the collector elements are polarized individually (at +200 mV) at secondary channels 2 – 8 of the potentiostat to compose seven collector working electrodes whose currents can be individually monitored. Configurations where there are more than seven collector elements are shorted symmetrically as described in the Experimental section. The outlined, unfilled bands and rings represent electrodes left at open circuit potential. The diagrams are not drawn to scale.

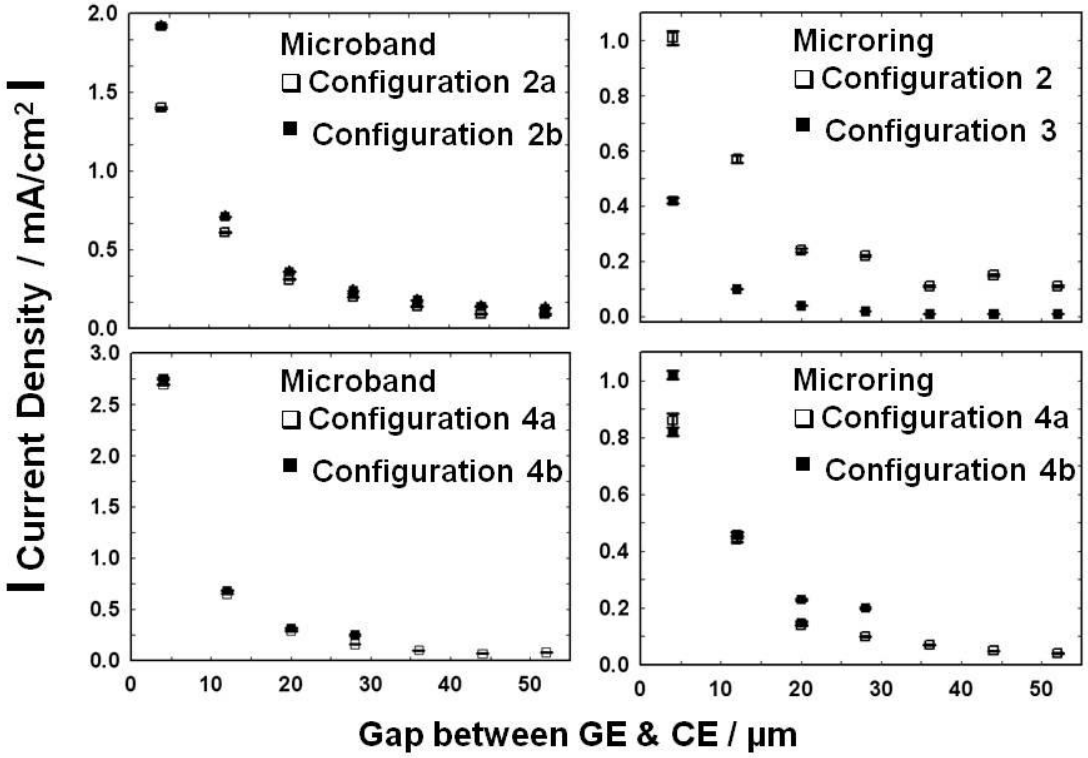

Figure 2.7. Dependence of current densities at each collector element located at different distances from the generator electrode in configurations 2, 3, and 4 of parallel band and concentric ring MEAs. The collection efficiency is proportional to the localized slope values along these plots (i.e. a higher slope for a given collector element of the configuration translates to a higher collection efficiency.)

side of the generator are similar for those having same gap from the generator. For the ring electrode, the area of each collector element is different from the other. The area increases as the collector elements move radially outward from the generator and decreases as they move radially inward. The current density decreases as the collector elements get further away from the generator, but the 'decrease' is more prominent for the collector rings radially outward of the generator than for those located radially inward. The collection efficiency for the elements radially outward of the generator, on the other hand, are greater than for those radially inward of the generator, but at the same gap. For example, the current density for the radially outward collector elements (11 to 13) in configuration 4b decreases as follows: 0.82 mA/cm^2, 0.46 mA/cm^2, 0.15 mA/cm^2 and for those radially inward (9 to 6) as follows: 1.02 mA/cm^2, 0.46 mA/cm^2, 0.23 mA/cm^2, 0.20 mA/cm^2. The collection efficiency for the radially outward collector elements (11 to 13) decreases as follows: 26.5%, 16.4%. 5.9% and for those radially inward (9 to 6) as follows: 26.1%, 10.2%, 4.3%, 3.1%. When compared the rings with the bands, it turns out that although the collectors nearest to the generator have lower current efficiencies for rings (26%) than bands (34%), the species that did not get captured move on to the next collector rings. Thus, the second set of collectors has higher collection efficiencies (16% and 10%) for rings than for bands (8%).

A large signal either at generator, at collector or at both is desired from redox cycling. Configurations 1a and 1b provide the largest currents at the collector elements for both geometries. Every collector element flanking each generator element provides maximum output of redox cycles of the molecule per unit time and steeper concentration gradient. The generator and the collector current density are highest for this arrangement (5.53 mA/cm^2 at generator and 5.33 mA/cm^2 at collector for band; 3.55 mA/cm^2 at generator and 3.33 mA/cm^2 at collector for

ring). Generator surrounded by the collector (Figure 2.6, C1a) is compared with the collector surrounded by the generator in Figure 2.6, C1b. Only half of the product enters the redox cycling from the outer collector elements. The rest is lost in the bulk. They have lower current density (3 mA/cm^2 for bands and 1.5 mA/cm^2 for rings) than the other 'inlaid' elements (5 mA/cm^2 for bands and 3 mA/cm^2 for rings). Thus, for best results a collector should be enclosed inside the generator. Collector element 2 in C1a for the rings has extremely low current density due to depletion of diffusion layers across its edges.

Configuration 4 has the high current density at the generator (8 mA/cm^2 for bands and > 3 mA/cm^2 for rings) due to quick consumption of its product by the collectors on both sides. The steep concentration gradient thus provides more efficient redox cycling. The current density for the collector elements closest to the generator is highest and then decrease outward as the gap increases for all configurations. This effect is clearly seen in figure 2.6 and confirms the simulation predictions by Wrighton and co-workers.[9] For gaps < 15 μm, the amplification in current density (factor of 4 for bands and 2 for rings when g is 4 μm; factor of 2 for bands and 3 for rings when g is 12 μm) is significant and exponential. The collector elements lying at a gap of < 15 μm from the generator contribute to > 80% of the total collector current. The collector elements lying at a gap > 15 μm only decrease the current density without adding significantly to the total current, thus lowering the sensitivity. Thus, smaller the interelectrode gap, higher the increment in the collection efficiency and the sensitivity. Equations have also been derived by Bard et. al. and simulations were used to predict collection efficiency as a function of gap, but only for one generator and one collector or for one generator flanked by two collectors. Such an equation does not account for any variation in the number or arrangement of generator and collector electrodes.[9]

Ultimately, comparison of different configurations of both geometries reveal that the parallel microband geometry would give the highest signal *per unit area of the overall space of the array occupied by active elements* in the array on the chip.

2.4.6.4 Calibration curves. Figure 2.8 shows linear calibration curves (all having R^2 values with at least two 9's) obtained for band and ring MEAs in $[Ru(NH_3)_6]^{3+}$ at 0.10 V/s scan rate with and without redox cycling using the alternating generator-collector configuration C1a. The detection limits were calculated at three times the standard deviation of the blank. The current sensitivity enhancement (calculated by dividing the slope of either the generator or collector in presence of redox cycling with the slope of the generator in its absence) at the generator (factor of 2.2 for bands and 2.5 for rings) and at the collector (factor of 1.8 for bands and 1.9 for rings) caused by redox cycling is significant for both the geometries. The sensitivity of all three calibration curves for the ring MEA (generator: 0.123 nA/μM, collector: 0.097 nA/μM, generator without redox cycling: 0.050 nA/μM) is only 20% of the sensitivities for the band MEA (generator: 0.590 nA/μM, collector: 0.474 nA/μM, generator without redox cycling: 0.266 nA/μM). Microrings also exhibit poorer detection limit (0.140 μM at the generator and 0.110 μM at the collector) than microbands (0.083 μM at the generator and 0.014 μM at the collector). This implies that a greater overlap of an electrode's diffusion field with itself results in greater depletion even with redox cycling, decreasing the current density as well as the detection limits of the microrings. Thus, overlap of diffusion layers may not necessarily affect the efficiency of redox cycling, but the sensitivity for a geometry.

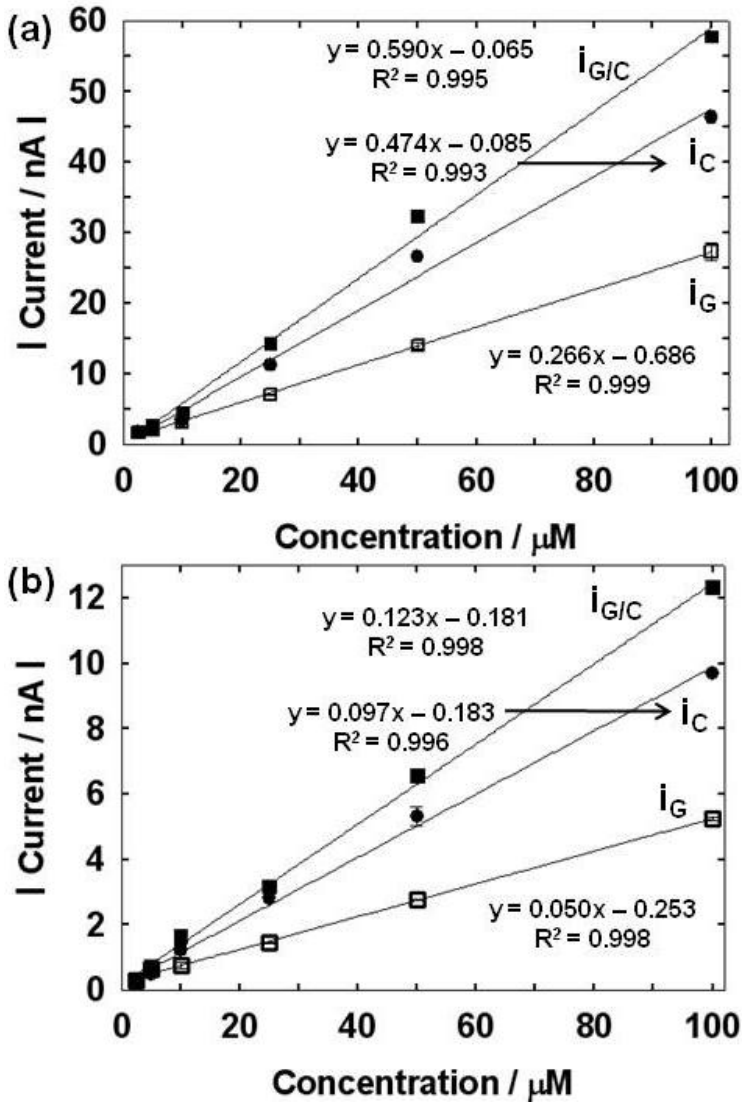

Figure 2.8. Calibration curves obtained from a single (a) parallel band and (b) concentric ring MEA in the presence and absence of redox cycling in varying concentrations of $[Ru(NH_3)_6]^{3+}$ at 0.01 V/s scan rate. Equations for the least squares best fit lines to the data are shown in the figure. Detection limits (determined from three times the standard deviation of the blank) are as follows: for (a) parallel bands: generator with collector off, 0.045 μM (open squares); generator with collector on, 0.083 μM (closed squares); collector, 0.0140 μM (closed circles); and for (b) concentric rings: generator with collector off, 0.110 μM (open squares); generator with collector on, 0.140 μM (closed squares); collector, 0.110 μM (closed circles). i_G is CV current, $i_{G/C}$ is the generator current during redox cycling and i_C is the collector current.

2.5 CONCLUSIONS

The use of individually addressable arrays and a multipotentiostat provided the flexibility to study redox cycling of various configurations of electrodes for ring and band geometries. By assigning different electrodes as collector elements, we could change the overall area for capture, without fabricating new chips. This was especially notable with C3 for the rings where a collector to generator area of 40 : 1 was easily achieved, taking advantage of the increasing sizes of the rings going outward from the generator. No improvement in detection limits is observed at ring arrays with the onset of redox cycling due to low current density. The overlapping diffusion layer of a circular electrode depletes itself across the diameter, and thus produce lower overall signal. With the given dimensions and for the given time scale, the bigger rings in array behave more closely to hemicylindrical symmetry like that of the bands, but the smaller rings show behavior intermediate of hemicylindrical and hemispherical symmetry.

Different factors need to be considered while designing a microelectrode array in addition to the geometry. Given the configurations and geometries that were investigated here, we can arrive at some recommendations. The alternating collector-generator-collector configuration (1a) and the parallel band geometry provides the best signal density at the collector as well as the best amplification. The collector flanking the generator on both sides (C4a) and the parallel band geometry provides the highest signal at the generator as well as the best collection efficiency. The alternating collector-generator-collector configuration and band geometry provides the lowest detection limits at the generator as well as the collector electrode per substrate area.

2.6 ACKNOWLEDGEMENTS

Funding has been provided in part by the National Science Foundation (CHE-0719097) and the Arkansas Biosciences Institute, the major research component of the Arkansas Tobacco Settlement Proceeds Act of 2000. We appreciate input from Professor David W. Paul on interpretation of the data. We thank Errol Porter for advice on microfabrication. The use of the High Density Electronics Center microfabrication facilities is also acknowledged.

2.7 REFERENCES

(1) Wightman, R. M.; Wipf, D. O. *Electroanalytical Chemistry* **1989**, *15*, 267-353.

(2) Niwa, O.; Morita, M.; Tabei, H. *Analytical Chemistry* **1990**, *62*, 447-452.

(3) Niwa, O.; Morita, M.; Tabei, H. *Journal of Electroanalytical Chemistry* **1989**, *267*, 291-297.

(4) Harvey, S. L. R.; Parker, K. H.; O'Hare, D. *Journal of Electroanalytical Chemistry* **2007**, *610*, 122-130.

(5) Licht, S.; Cammarata, V.; Wrighton, M. S. *Journal of Physical Chemistry* **1990**, *94*, 6133-6140.

(6) Phillips, C. G.; Stone, H. A. *Journal of Electroanalytical Chemistry* **1997**, *437*, 157-165.

(7) Singh, K. V.; Whited, A. M.; Ragineni, Y.; Barrett, T. W.; King, J.; Solanki, R. *Analytical and Bioanalytical Chemistry* **2010**, *397*, 1493-1502.

(8) Bard, A. J.; Faulkner, L. R. *Electrochemical methods : fundamentals and applications*, 2nd ed ed.; New York : Wiley, 2001.

(9) Bard, A. J.; Crayston, J. A.; Kittlesen, G. P.; Shea, T. V.; Wrighton, M. S. *Analytical Chemistry* **1986**, *58*, 2321-2331.

(10) Albery, W. J.; Brett, C. M. A. *Journal of Electroanalytical Chemistry* **1983**, *148*, 201-210.

(11) Albery, W. J.; Brett, C. M. A. *Journal of Electroanalytical Chemistry* **1983**, *148*, 211-220.

(12) Fosset, B.; Amatore, C.; Bartelt, J.; Wightman, R. M. *Analytical Chemistry* **1991**, *63*, 1403-1408.

(13) Fosset, B.; Amatore, C. A.; Bartelt, J. E.; Michael, A. C.; Wightman, R. M. *Analytical Chemistry* **1991**, *63*, 306-314.

(14) Odijk, M.; Olthuis, W.; Dam, V. A. T.; van den Berg, A. *Electroanalysis* **2008**, *20*, 463-468.

(15) Albery, W. J.; Compton, R. G.; Hillman, A. R. *Journal of the Chemical Society-Faraday Transactions I* **1978**, *74*, 1007-1019.

(16) Bruckenstein, S.; Gifford, P. R. *Analytical Chemistry* **1979**, *51*, 250-255.

(17) Liljeroth, P.; Johans, C.; Slevin, C. J.; Quinn, B. M.; Kontturi, K. *Analytical Chemistry* **2002**, *74*, 1972-1978.

(18) Menshykau, D.; del Campo, F. J.; Munoz, F. X.; Compton, R. G. *Sensors and Actuators B-Chemical* **2009**, *138*, 362-367.

(19) Roston, D. A.; Shoup, R. E.; Kissinger, P. T. *Analytical Chemistry* **1982**, *54*, 1417-&.

(20) Fosdick, L. E.; Anderson, J. L. *Analytical Chemistry* **1986**, *58*, 2481-2485.

(21) Ghanem, M. A.; Thompson, M.; Compton, R. G.; Coles, B. A.; Harvey, S.; Parker, K. H.; O'Hare, D.; Marken, F. *Journal of Physical Chemistry B* **2006**, *110*, 17589-17594.

(22) Islam, M. M.; Ueno, K.; Misawa, H. *Analytical Sciences* **2010**, *26*, 19-24.

(23) Niwa, O.; Kurita, R.; Liu, Z. M.; Horiuchi, T.; Torimitsue, K. *Analytical Chemistry* **2000**, *72*, 949-955.

(24) Niwa, O.; Morita, M. *Analytical Chemistry* **1996**, *68*, 355-359.

(25) Dam, V. A. T.; Olthuis, W.; van den Berg, A. *Analyst* **2007**, *132*, 365-370.

(26) Katelhon, E.; Hofmann, B.; Lemay, S. G.; Zevenbergen, M. A. G.; Offenhausser, A.; Wolfrum, B. *Analytical Chemistry* **2010**, *82*, 8502-8509.

(27) Niwa, O.; Morita, M.; Tabei, H. *Electroanalysis* **1991**, *3*, 163-168.

(28) Vandaveer, W. R.; Woodward, D. J.; Fritsch, I. *Electrochimica Acta* **2003**, *48*, 3341-3348.

(29) Morita, M.; Niwa, O.; Horiuchi, T. *Electrochimica Acta* **1997**, *42*, 3177-3183.

(30) Niwa, O. *Electroanalysis* **1995**, *7*, 606-613.

(31) Niwa, O.; Morita, M.; Tabei, H. *Electroanalysis* **1994**, *6*, 237-243.

(32) Niwa, O.; Tabei, H. *Analytical Chemistry* **1994**, *66*, 285-289.

(33) Niwa, O.; Tabei, H.; Solomon, B. P.; Xie, F. M.; Kissinger, P. T. *Journal of Chromatography B-Biomedical Applications* **1995**, *670*, 21-28.

(34) Alden, J. A.; Booth, J.; Compton, R. G.; Dryfe, R. A. W.; Sanders, G. H. W. *Journal of Electroanalytical Chemistry* **1995**, *389*, 45-54.

(35) Aoki, K. *Journal of Electroanalytical Chemistry* **1989**, *270*, 35-41.

(36) Aoki, K. *Journal of Electroanalytical Chemistry* **1990**, *284*, 35-42.

(37) Aoki, K.; Morita, M.; Niwa, O.; Tabei, H. *Journal of Electroanalytical Chemistry* **1988**, *256*, 269-282.

(38) Aoki, K.; Tokuda, K. *Journal of Electroanalytical Chemistry* **1987**, *237*, 163-170.

(39) Aoki, K.; Tokuda, K.; Matsuda, H. *Journal of Electroanalytical Chemistry* **1987**, *230*, 61-67.

(40) Aoki, K.; Tokuda, K.; Matsuda, H. *Journal of Electroanalytical Chemistry* **1987**, *225*, 19-32.

(41) Ju, H. X.; Chen, H. Y.; Gao, H. *Acta Chimica Sinica* **1992**, *50*, 895-900.

(42) Ju, H. X.; Chen, H. Y.; Hong, G. *Journal of Electroanalytical Chemistry* **1992**, *341*, 35-46.

(43) Streeter, I.; Compton, R. G. *Journal of Physical Chemistry C* **2007**, *111*, 15053-15058.

(44) Amatore, C.; Da Mota, N.; Lemmer, C.; Pebay, C.; Sella, C.; Thouin, L. *Analytical Chemistry* **2008**, *80*, 9483-9490.

(45) Amatore, C.; Da Mota, N.; Sella, C.; Thouin, L. *Analytical Chemistry* **2007**, *79*, 8502-8510.

(46) Amatore, C.; Da Mota, N.; Sella, C.; Thouin, L. *Analytical Chemistry* **2010**, *82*, 2434-2440.

(47) Amatore, C.; Sella, C.; Thouin, L. *Journal of Physical Chemistry B* **2002**, *106*, 11565-11571.

(48) Arkoub, I. A.; Amatore, C.; Sella, C.; Thouin, L.; Warkocz, J. S. *Journal of Physical Chemistry B* **2001**, *105*, 8694-8703.

(49) Bidwell, M. J.; Alden, J. A.; Compton, R. G. *Journal of Electroanalytical Chemistry* **1996**, *417*, 119-128.

(50) Compton, R. G.; Dryfe, R. A. W.; Alden, J. A.; Rees, N. V.; Dobson, P. J.; Leigh, P. A. *Journal of Physical Chemistry* **1994**, *98*, 1270-1275.

(51) Compton, R. G.; Fisher, A. C.; Wellington, R. G.; Dobson, P. J.; Leigh, P. A. *Journal of Physical Chemistry* **1993**, *97*, 10410-10415.

(52) Compton, R. G.; Wellington, R. G.; Dobson, P. J.; Leigh, P. A. *Journal of Electroanalytical Chemistry* **1994**, *370*, 129-133.

(53) Compton, R. G.; Winkler, J. *Journal of Physical Chemistry* **1995**, *99*, 5029-5034.

(54) Amatore, C.; Oleinick, A.; Svir, I. *Journal of Electroanalytical Chemistry* **2004**, *564*, 245-260.

(55) Brookes, B. A.; Gavaghan, D. J.; Compton, R. G. *Journal of Physical Chemistry B* **2002**, *106*, 4886-4896.

(56) Daschbach, J.; Pons, S.; Fleischmann, M. *Journal of Electroanalytical Chemistry* **1989**, *263*, 205-224.

(57) Fleischmann, M.; Bandyopadhyay, S.; Pons, S. *Journal of Physical Chemistry* **1985**, *89*, 5537-5541.

(58) Fleischmann, M.; Daschbach, J.; Pons, S. *Journal of Electroanalytical Chemistry* **1988**, *250*, 269-276.

(59) Fleischmann, M.; Daschbach, J.; Pons, S. *Journal of Electroanalytical Chemistry* **1989**, *263*, 189-203.

(60) Fleischmann, M.; Pletcher, D.; Denuault, G.; Daschbach, J.; Pons, S. *Journal of Electroanalytical Chemistry* **1989**, *263*, 225-236.

(61) Fleischmann, M.; Pons, S. *Journal of Electroanalytical Chemistry* **1987**, *222*, 107-115.

(62) Fleischmann, M.; Pons, S. *Journal of Electroanalytical Chemistry* **1988**, *250*, 257-267.

(63) Fleischmann, M.; Pons, S. *Journal of Electroanalytical Chemistry* **1988**, *250*, 277-283.

(64) Fleischmann, M.; Pons, S. *Journal of Electroanalytical Chemistry* **1988**, *250*, 285-292.

(65) Anderson, E. C.; Weston, M. C.; Fritsch, I. *Analytical Chemistry* **2010**, *82*, 2643-2651.

(66) Smythe, W. R. *Journal of Applied Physics* **1951**, *22*, 1499-1501.

(67) Seddon, B. J.; Girault, H. H.; Eddowes, M. J. *Journal of Electroanalytical Chemistry* **1989**, *266*, 227-238.

(68) Yang, X.; Zhang, G. **2005**.

3. METHOD DEVELOPMENT FOR DETECTION OF DOPAMINE IN THE PRESENCE OF ASCORBIC ACID THROUGH REDOX CYCLING

3.1 ABSTRACT

Electrochemical behavior of dopamine (DA) is examined under redox cycling conditions in the presence and absence of interferences ascorbate (AA) and 3,4-dihydroxyphenylacetic acid (DOPAC). Redox cycling converts a redox species between its oxidized and reduced form by applying suitable potentials on a set of closely located generator and collector electrodes. It allows signal amplification and discrimination between species that undergo reversible and irreversible electron transfer. Microfabrication is used to produce microband electrodes contained in a microelectrode array (MEA) with an inter electrode spacing of 4 μm. Different assignments of electrodes as generators and collectors are explored for optimum detection of dopamine in presence of ascorbate. The detection limit of dopamine in the presence of 100 μM ascorbate was found to be 0.452 ± 0.026 μM at the collector. DOPAC shows a weak signal at the collector. Detection of 10 μM dopamine in presence of 20 μM DOPAC is obtained at the electrodes coated with Nafion. The results suggest that there is possibility of a new class of multi-electrode probes that could be used for in vivo quantification of transients and tonic levels of neurotransmitters without background subtraction. Further method development along with exploration of polymer coatings is required prior to the in vivo quantification of these probes.

3.2 INTRODUCTION

To our knowledge, this is the first report on detection of physiological concentration of dopamine (DA) in the presence of high concentrations of excess ascorbate (AA, 100 x) with redox cycling, without the use of polymer coatings such as Nafion® and with the possibility to extend the concept in vivo. Dopamine detection in the presence of 3,4-dihydroxyphenylacetic acid (DOPAC) through redox cycling is also shown. Extracellular concentrations of non evoked dopamine release in striatum are reported to be in single digit micro molar.[1-4] Concentrations in low nanomolar range have been detected using redox cycling previously either with the use of flow channels or with electrode modification.[5-12] Figure 3.1 shows the schematics for redox cycling of dopamine in presence of ascorbate.

The mammalian metabolite, dopamine is a significant catecholamine and a 'stand alone' neurotransmitter.[13, 14] Dopaminergenic systems are involved in a multitude of functions including neurocognition, motor control, motivation, punishment, and reward.[15-17] Dysfunction of dopamine production or uptake is a key factor in various diseases such as Parkinson's disease,[18, 19] Huntington's disease,[20, 21] substance abuse,[19, 21, 22] Tourette's syndrome,[23] schizophrenia,[24] and attention deficit hyperactivity disorders.[21, 25] The need to study dopamine for neurological and medical purposes is well documented in literature.[18, 26]

Ascorbate is the main interference in electrochemical detection of dopamine in the extracellular brain, where it is highly concentrated (200 – 400 µM).[27-30] It acts as a neuromodulator for dopamine mediated neurotransmission, and is shown to be released simultaneously with catecholamines in adrenal medulla.[28, 29] It is electroactive in the similar potential range as other catecholamines and is found in 100 to 1000 times in excess of their

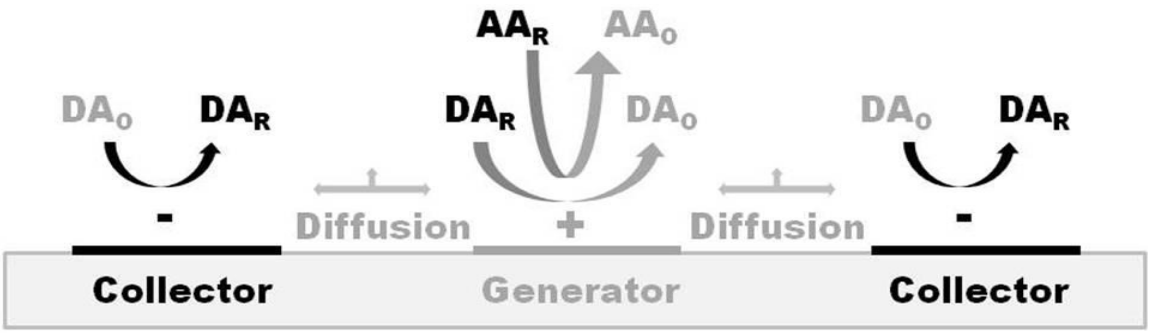

Figure 3.1. Schematics for the redox cycling of dopamine in presence of ascorbate on closely spaced microband electrodes contained in a MEA. The generator is held at oxidation potential (+ 500 mV) and the collector at reduction potential (- 200 mV). Dopamine shows oxidation current at generator due to its conversion to dopamine-quinone and reduction current at collector due to regeneration of dopamine. Ascorbate however shows only the oxidation current at the generator due to its conversion to dihydroascorbic acid.

concentrations.[31-33] There is a need to differentiate between the signal arising from dopamine and the signal not only from ascorbate but other interfering catecholamines as well.

Easy oxidation of dopamine and sub-second time resolution of electrochemical methods renders it suitable for electroanalysis. Being electrochemically reversible, dopamine is easily detected by redox cycling. Few reports exist on redox cycling to detect dopamine which utilize closely spaced electrodes fabricated on a MEA.[5, 6, 9-11, 34-36] Two or more closely spaced electrodes, the generator and the collector, are held at oxidative and reductive potentials, respectively. DA undergoes oxidation at the generator; the product diffuses across the gap and reduces back at the collector. The current produced is directly proportional to the concentration gradient of the given form of the redox species at the electrode surface.[37, 38] Being electrochemically irreversible, ascorbate does not produce any signal at the collector.[10, 35] The method not only offers improved signal-to-background ratio and real-time monitoring of ascorbate without requiring high-speed scanning electronics, but also provides elimination from ascorbate interference at the collector.

Most other electrochemical methods exploit the difference in the electron transfer rate of dopamine and ascorbate to shift the oxidation peak of ascorbate to more positive potentials. Much of the earlier work related to measuring neurotransmitters in vivo employed differential pulse voltammetry (DPV). It has poor temporal resolution (>30 s) and allows little selectivity for simultaneous measurement of analytes with oxidation peaks more than 100 mV apart.[39] Chronoamperometry offers submillisecond temporal resolution. It has been used to detect dopamine and other catecholamine neurotransmitters,[40-43] but has poor chemical selectivity. Fast scan cyclic voltammetry (FSCV) is currently the most widely used electrochemical method for making dopamine measurements. High temporal resolution of FSCV (100 ms) allows rapid

monitoring of dopamine. It uses a short time scale to exclude slow ascorbate oxidation. However, the huge charging current (caused by charging of the double layer) overtakes the faradaic signal. Because the background current in vivo is stable for a short time only,[44, 45] FSCV is typically not used for measurements exceeding a minute.[31] Thus, it is difficult with FSCV to measure resting or static dopamine concentrations, where redox cycling would be of further interest.

Microdialysis is a widely used sampling method for making in vivo measurements. It uses a dialysis probe (> 200 μm diameter) with a permselective membrane to collect dialysate from the extracellular region of the brain. The collected dialysate can be analyzed with a variety of techniques such as with liquid chromatography with electrochemistry, providing good chemical resolution. Degeneration of the tissue by ischemia and glial proliferation are some of the side effects.[2, 3, 46-49] Continuous extraction of the fluid from the brain, swelling of the probe under perfusion pressure and flow of the perfusion fluid back to the tissue causes edema.[3] It is now believed that the technique does not measure the actual, naturally-occurring concentration, but only the concentration produced by the surviving dopaminergenic elements in the tissue. Also, microdialysis has fairly slow temporal resolution (typically a 10 min sampling rate, 1 min in some cases), although Kennedy and coworkers have achieved 14 s resolution.[50] Non-invasive spectroscopic methods such as functional magnetic resonance imaging and positron emission tomography are also available that can map the neurochemical activity in regions of an intact brain, however, distinguishing between various neurotransmitters requires assistance of other agents.

Probes of carbon fiber electrodes (CFEs, only 5-15 μm diameter) and metal electrode such as gold and platinum (that can be microfabricated onto arrays) allow electrochemical

methods to avoid the above mentioned problems. Fluorescence microscopy has revealed the absence of ischemia and glial proliferation upon insertion of CFEs in brain.[48] Dopamine concentrations measured at CFEs are 10^3 times higher than estimated by microdialysis.[1, 4, 51] They show minimal fouling in vivo compared to metal electrodes. They have low background current over a wider potential window, especially in the cathodic potential region. Some laboratories prefer to make their own electrodes due to high cost. The state of the art fabrication procedure for CFEs is lengthy and irreproducible. Their shafts being bulky, they cannot be inserted in the same brain region simultaneously. Because a CFE has a single sensing site, it limits the scope of spatially correlating studies for dopamine release and uptake mechanisms and application of multi-electrode techniques such as redox cycling.

Metal electrodes (gold and platinum) on the other hand require polymer coatings to reduce biofouling. Thiol adsorption is a common problem at gold electrodes.[52-55] They also have smaller potential window compared to carbon electrodes. Metal unlike carbon can be more easily microfabricated onto substrates in form of arrays, having better spatial resolution.[56-58] This provides greater control over electrode size and spacing, flexibility in electrode design as well as application of advanced electrochemical studies.[59] Both, carbon fiber and metal microelectrodes should be suitable for study of same or multiple analyte(s) in the same or different brain region(s) simultaneously.

Chemical selectivity is the most severe limitation common to sensors. Electrode surface modification methods are often used to improve selectivity and sensitivity for the desired analyte. Nafion (perfluorinated cation-exchange membrane) is the most popular polymer surface coating since its use first by Ralph Adams' laboratory.[11, 19, 60, 61] The sulphonated derivative of Teflon, Nafion is a permselective polymer membrane. It was first used by Gerhardt et al. in 1984

coated on carbon fiber electrodes.[62] Unlike other resins, it is not covalently cross linked. Presence of the fixed anionic sites due to the ionization of the sulphonate groups in wet Nafion repels the anionic species, providing elimination from their signal.[63] These sulphonic acid groups also concentrate the cationic species. The dopamine cation enters the Nafion layer through ion exchange with Na^+ as the counter ion.[64] Nafion is also known to show an extraordinary affinity toward hydrophobic cation.[65] This property of Nafion is also exploited by the hydrophobic dopamine molecule. Positively-charged dopamine (and other biogenic amines) at the physiological pH electrostatically-incorporates and concentrates in the negatively-charged Nafion, increasing the sensitivity toward dopamine by 200 fold over the negatively charged species such as ascorbate. However, the molecule takes much longer to diffuse through the Nafion and reach the electrode due to a significant decrease in diffusion coefficient from 2.4 x 10^{-6} cm^2s^{-1} in solution[66] to 2 x 10^{-9} cm^2s^{-1} in the polymer[11, 67]. Thus, the change in concentration of dopamine at the electrode surface causes a change in the signal. Other coatings include self-assembled monolayers having acidic end groups,[67, 68] polymer electrodes with films of polypyrrole-tetradecylsulfate,[69] poly(indole-3-acetic acid),[70] or electrochemically pre-treated electrode surface[71]. Such methods exploit the difference in the positively charged dopamine and other biogenic amines having protonated amino side chain and that of negatively charged ascorbate (an anion repelling the electrode surface) at physiological pH.

DOPAC is an electrochemically active dopamine metabolite that interferes in its detection. The oxidation peak of DOPAC appears at +0.2 V versus Ag/AgCl reference electrode, which is the same as that for dopamine and ascorbate.[31] Its concentration is 20-50 times that of dopamine.[19, 45, 72-76] It is therefore of interest to determine the performance of redox cycling in the presence of DOPAC. Both DOPAC and ascorbate are weak acids as well as anions at

physiological pH. They are therefore rejected by the sulphonate groups of the Nafion polymer coating on an electrode, providing 200 fold greater sensitivity compared to these compounds. The overoxidized polypyrrole films also exhibit similar properties and are shown to be efficient toward accumulating dopamine over ascorbate and DOPAC.[45, 77-79] Selective redox cycling of dopamine in presence of ascorbate has been shown by Niwa et. al. on Nafion coated electrodes.[11] The concept can be extended to the redox cycling of accumulated dopamine in a mixture with DOPAC as well as in a mixture with DOPAC and ascorbate. DOPAC is electrochemically reversible unlike ascorbate, producing a signal both at the generator and collector during redox cycling. Hence, the redox cycling of dopamine in presence of DOPAC was carried out on Nafion coated electrodes.

This article describes redox cycling for detection of dopamine with and without ascorbate, and with and without DOPAC on a MEA in two different electrode assignments. The arrangement of electrode where central collector surrounded by large generator on both sides was used for detection of dopamine in presence of 100 fold excess ascorbate; alternating generator collector arrangement of electrodes was used for detection dopamine in presence of two fold excess DOPAC. Due to the presence of excess ascorbate, the electrocatalytic reaction between ascorbate and the oxidized dopamine resulted in no signal at the collector using the alternating generator collector arrangement of electrodes. Therefore, a different arrangement of electrodes was used having much higher generator to collector area (3.5:1) than in the alternating arrangement (1:1) to consume the excess ascorbate. Exploration of a modified MEA is additionally addressed for further discrimination of species.

3.3 EXPERIMENTAL

3.3.1 Chemicals and Materials. All chemicals were used as received unless otherwise stated. Hexaammineruthenium (III) chloride, dopamine hydrochloride, L-(+)-ascorbic acid, 3,4-dihydroxyphenylacetic acid, dextrose anhydrous, 2-[4-(2-hydroxyethyl)piperazin-1-yl]ethanesulfonic acid, and 4-amino-2-hydroxymethyl-propane-1,3-diol (all ACS grade) are obtained from Alfa Aesar (MA, USA). Water, ACS reagent grade (≥18 MΩ-cm), is obtained from Ricca Chemical Co. (Arlington, TX). Nafion® (perfluorinated ion exchange resin, 5 weight % in a mixture of lower aliphatic alcohols and water) was obtained from Sigma Aldrich and was either used as received or was diluted with ethanol (200 proof absolute, anhydrous, ACS/ USP grade).

3.3.2 MEAs. The MEA devices are shown in Figure 3.2. They contain 18 coplanar band electrodes, one large gold feature (4.00 mm x 2.00 mm) that served as an on-chip quasireference and one large gold feature (4.00 mm x 4.00 mm) that served as an auxillary electrode. Each of the electrodes in the array is individually addressable via contact pads. The microbands have an average length of 2.00 ± 0.01 mm, width of 4.0 ± 0.1 μm and are separated by 4.0 ± 0.1 μm gaps. The characterization of these MEAs performed using a model compound, hexaammineruthenium (III) chloride, are reported elsewhere.

They were fabricated using a conventional photolithographic procedure described previously.[80] In brief, a 50 nm thick layer of gold was deposited onto a 5 nm thick chromium adhesion layer on a silicon-dioxide coated (2 μm) silicon wafer. (Thicknesses are based on the readings of the piezoelectric crystal thickness monitor on the thermal evaporator that was used to deposit the metals.) After patterning the metal layers to define electrodes, leads and contact pads,

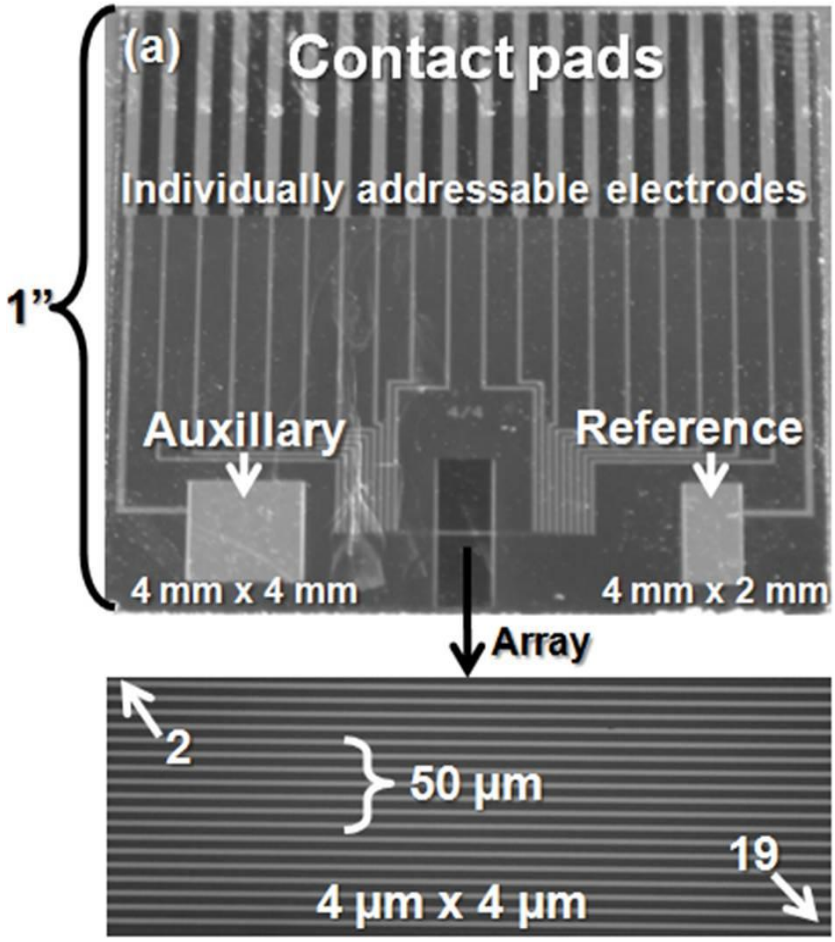

Figure 3.2. Photographic image showing a full view and an expanded view of the array region of a parallel band MEA. The microband electrodes are numbered from *2* to *19*, with the counter and quasireference electrodes numbered as *1* and *20*, respectively.

MEAs were encapsulated by an insulation layer (formed by the polymer benzocyclobutene (BCB)) and subsequently patterned to open up the active electrode areas that would be exposed to solution and the contact pads that would be inserted into the edge connector (solder contact, 20/40 position, 0.05 in. pitch, Sullins Electronics Corp., CA).

3.3.3 Experimentation and Equipment. All experiments were carried out in triplicate with a fresh solution each time to avoid carryover from the previous electrochemistry. A bipotentiostat equipped with a faraday cage and a picoamp booster (CHI 760, CH Instruments, Austin, TX) was used. For redox cycling experiments, the potential was either swept for a full range (-0.2 V to + 0.5 V) or held constant (+ 0.5 V) at the generator relative to a Ag/AgCl (saturated KCl) reference electrode. The collector was held at a constant potential (-0.2 V). In order to determine the amplification, all redox cycling experiments were repeated with the collector left at open circuit potential. Dopamine and ascorbate solutions were made fresh each time in TRIS buffer (15 mM TRIS, 140 mM NaCl, 3.25 mM KCl, 1.2 mM $CaCl_2$, 1.25 mM $NaHPO_4$, 2.0 mM Na_2SO_4) or in a-CSF buffer (100 mM NaCl, 5.0 mM KCl, 1.2 mM NaH_2PO_4, 5.0 mM $NaHCO_3$, 10 mM glucose, 2.5 mM HEPES, 1.2 mM $MgSO_4$, 1.0 mM $CaCl_2$) at 7.4 pH. *Note that only the stock solutions were purged under Ar gas, however, the experiments were conducted in oxygen environment and not in a glove bag.* The detection limits were calculated at three times the standard deviation of the blank. Eaton 6000 HX spin coater available at HiDEC center (University of Arkansas) was used for the spin coating of Nafion. Nafion diluted with ethanol in different ratios (1:0, 1:1, 1:4, 1:9 Nafion: EtOH by volume) was spin coated at MEAs at different spin speeds.

3.4 RESULTS AND DISCUSSION

3.4.1 Redox cycling of dopamine. Electrochemical behavior of dopamine was compared with and without redox cycling at a MEA using an alternating generator-collector assignment of electrodes. Nine microbands (even numbered bands in Figure 3.2) were shorted together to form the generator and the intervening nine microbands (odd numbered bands in Figure 3.2) were shorted together to form the collector. As shown in Figure 3.3, 100 µM dopamine in TRIS buffer shows pseudosteady state current with hemicylindrical symmetry at the microelectrodes during cyclic voltammetry (i_G, collector left at open circuit potential) at 0.01 V/s scan rate. Overlap of diffusion layers of neighboring electrodes causes the current to start to drop off at long times (6.1 ms or more). With the onset of redox cycling (collector poised at a reducing potential of -0.2 V), the flattening behavior of diffusion overlap is no longer observed, as the intermediate collectors replenish the supply of the redox species to the generators. An amplification factor of $A_F = 2.2$ and collection efficiency of $C_e = 66.67\%$ were obtained with redox cycling. A_F is the ratio of the generator current when the redox cycling is on (collector is polarized at -0.2 V) to the generator current when the redox cycling is off (collector is left at open circuit potential). C_e is the ratio of the generator current to the collector current when the redox cycling is on. A_F defines the increase in the generator current and C_e defines the percent redox species that diffuse from the generator to the collector to enter redox cycling.

Figure 3.4 shows a calibration curve of dopamine over a range of concentrations (5 µM to 100 µM) with and without redox cycling at a slow scan rate (0.01 V/s) using the same configuration of electrodes. A linear correlation of current with concentration was obtained (all having R^2 values of ≥ 0.99). The calibration curves were obtained after the continuous use of the

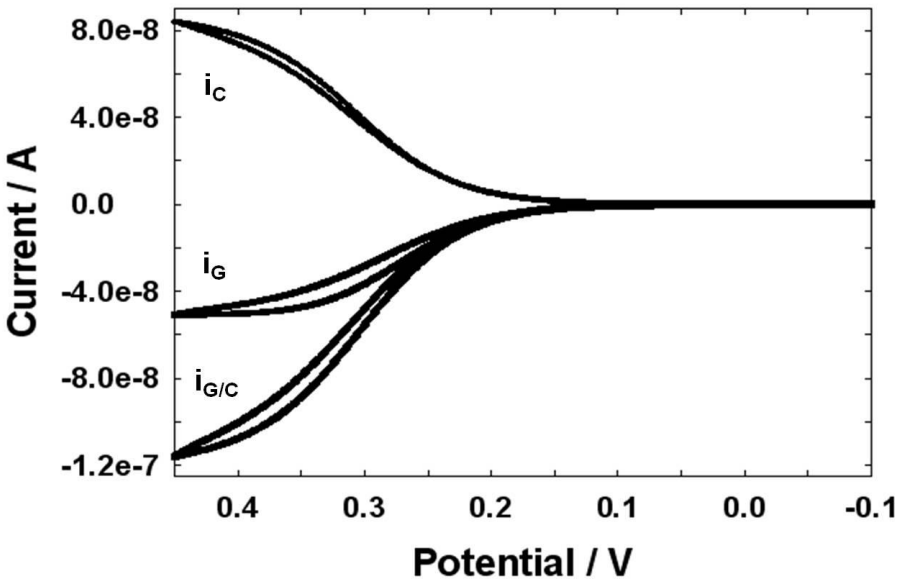

Figure 3.3. CV responses, without and with redox cycling, in a solution of 100 µM dopamine in TRIS buffer (pH 7.4) at 0.01 V/s scan rate on band MEA using an alternating generator-collector assignment of the electrodes. During redox cycling, the current at the generator electrode ($i_{G/C}$) is obtained by sweeping the full potential range versus a Ag/AgCl (saturated KCl) reference electrode and the collector current (i_c) is monitored simultaneously while that electrode is held at a reducing potential (-0.2 V). CV at the generator produces the current i_G when the collector is left at open circuit potential

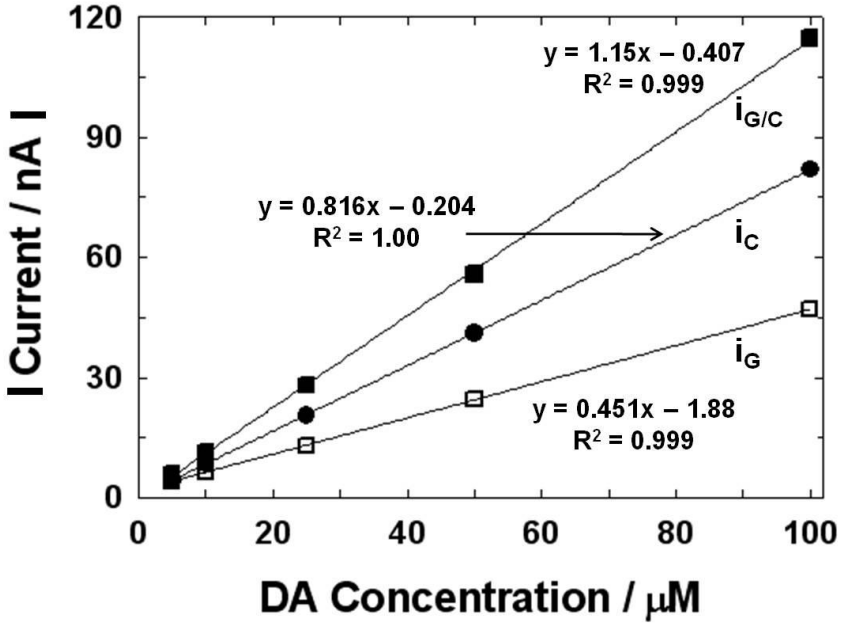

Figure 3.4. Calibration curve of current as a function of dopamine concentration in TRIS buffer (pH 7.4) with 9 pairs of alternating generator and collector electrodes at a microband MEA in the absence (generator, open squares, i_G) and presence (generator, closed squares, $i_{G/C}$ and collector, closed circles, i_C) of redox cycling using CV at 0.01 V/s scan rate. Detection limits of dopamine are as follows: generator current with collector on ($i_{G/C}$): 60.4 ± 0.506 nM (closed squares); collector current (i_C): 90.1 ± 0.199 nM (closed circles); generator current with collector off (i_G): 29.0 ± 0.148 nM (open squares).

MEAs over a period of > 4 hours with more than 50 electrochemical runs. This suggests that these MEAs have long term anti-fouling properties in dopamine – TRIS solution. The A_F, calculated from the ratio of slopes obtained at the generator with and without redox cycling was 2.5. The C_e, calculated from the ratio of slopes at the collector with that at the generator during redox cycling was 71%. The A_F for dopamine is 2.5 and for $Ru(NH_3)_6$ is 2.2 from the previous chapter. This implies that dopamine is being adsorbed on the gold surface. The C_e for dopamine is 21% lower than that for $[Ru(NH_3)_6]^{3+}$ (C_e = 90%, shown previously) on the same device.[80] This could be a result of loss of dopamine from intramolecular cyclization to form the indole,[81] which cannot be reduced at the collector. The reaction is shown in Figure 3.5. Because the formation of indole is slow (k = 0.1 s^{-1} at physiological pH),[82] a significant amount of oxidized dopamine still reaches the collector and produces current, but is lower than expected.

The detection limits for dopamine were better here for traditional CV (29.0 ± 0.148 nM, 0.02 V/s, open squares) than for redox cycling (60.4 ± 0.506 nM at generator, closed squares and 90.1 ± 0.199 nM at collector, closed circles). This is due to the limitation of the instrument. The picoamp booster for the CHI potentiostat does not support the secondary electrodes, and therefore does not filter out noise at collector. With provision of better instrumentation that can filter out noise at secondary working electrode, detection limits should improve. Also the collector is held at potentials close to that for oxygen reduction (-0.2 V). Thus, the reduction of atmospheric oxygen at collector adds to random error, leading to a higher STD_C and thus, poor detection limit.

3.4.2 Redox cycling of dopamine in presence of ascorbate. Redox cycling was also evaluated for the elimination of ascorbate signal. Redox cycling of 1 µM dopamine in the presence of 100 µM ascorbate was performed using the same alternating assignment of generator

Dopamine-o-quinone **Substituted Indole**

Intramolecular cyclization of DA.[43]

Figure 3.5. The oxidation product of dopamine, dopamine-quinone (DAQ) undergoes spontaneous intramolecular cyclization to form a substituted indole. The occurrence of this reaction causes a loss in the electrochemical signal at the collector.

and collector electrodes. A dopamine reduction signal at the collector was not observed. This could be due to the presence of excess ascorbate around the oxidized form of dopamine, dopamine-quinone (DAQ). This is a problem because the ascorbate undergoes a spontaneous reaction (shown in Figure 3.6) with DAQ, converting it back to dopamine and resulting in a loss of signal at the collector.[11, 35, 83] However, this reaction is known to have slow kinetics. Therefore, we estimate that by increasing the generator area to consume ascorbate, dopamine-quinone should survive the trip to the collector and a corresponding electrochemical response from its conversion to dopamine should be observed there.

In the event when no signal was observed from dopamine reduction at the collector due to the presence of excess of ascorbate, a signal was observed at the collector, however, due to oxygen reduction. As the generator was slowly scanned from reducing to oxidizing potentials, more oxygen was available to undergo a reaction at the collector. An eventual increase in the collector signal is therefore observed slowly. This is further confirmed by the redox cycling done in buffer alone. The collector showed similar oxygen reduction in buffer as the generator slowly scanned toward the oxidizing potentials.

Redox cycling of 1 μM dopamine in the presence of 100 μM ascorbate in TRIS buffer (pH 7.4) was then carried out with a different assignment of the electrodes: the outer 16 generators (bands 2-9 and 12-19) flanking the inner 2 collectors (bands 10-11). It was possible to vary the assignment of the electrodes because they are all individually addressable. Redox cycling at the generator shows only 5 % sensitivity toward ascorbate compared to that for dopamine. Figure 3.7 shows that the generator current (19.85 nA) obtained from the mixture of dopamine and ascorbate is equivalent to the sum of the generator currents obtained from the individual dopamine solution (2.92 nA) and the ascorbate solution (14.80 nA). The ascorbate is

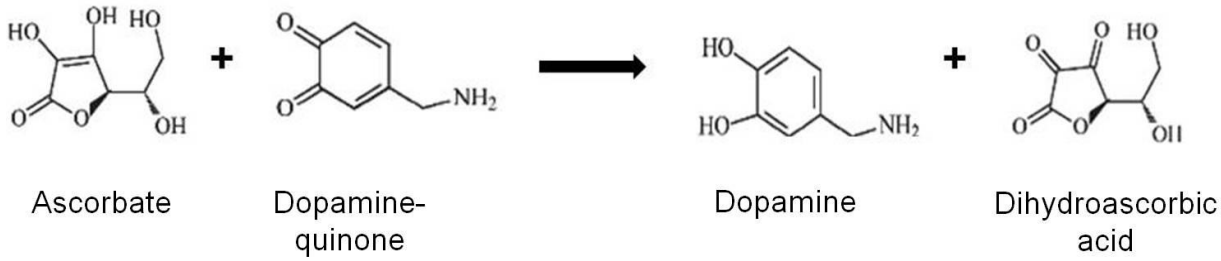

Figure 3.6. Spontaneous reaction between ascorbate and the quinone form of dopamine to form dihydroascorbic acid and the reduced form of dopamine is shown. This reaction consumes dopamine-quinone before it reaches the collector and enters redox cycling, resulting in a loss of signal at collector, and lower amplification as well as collection efficiency.

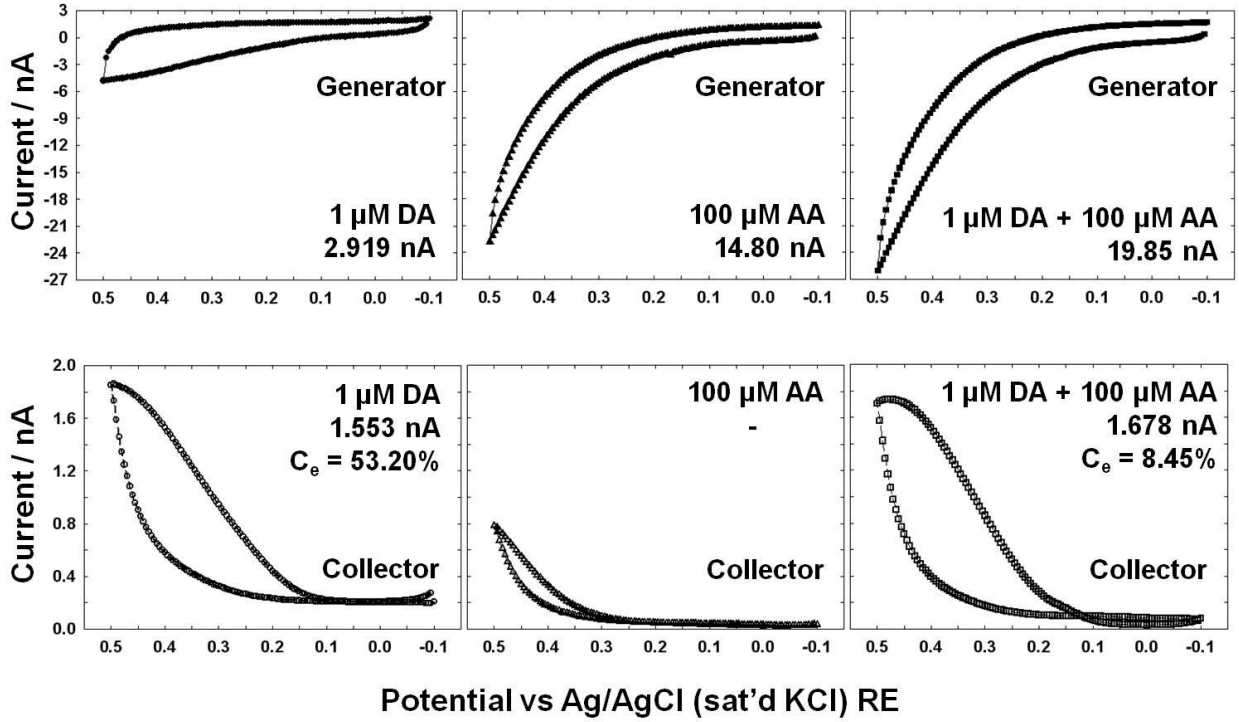

Figure 3.7. Comparison of CV responses of 1 µM dopamine, 100 µM ascorbate, and their mixture in TRIS buffer (pH 7.4) at band MEA with outer generators (bands 2-9 and 12-19; shown in the top row of plots) flanking the inner collectors (bands 10-11; shown in the bottom row of plots) during redox cycling at 0.01 V/s scan rate.

adding to the current at the generator (during redox cycling of dopamine in their mixture, but not adding to the amplification because it does not actually enter redox cycling. The only amplification observed (1.2) is due to the presence of 1 μM dopamine in the mixture which gets recycled at the collector.

The collector current obtained from the mixture of dopamine and ascorbate (1.68 nA) is equivalent to the collector current obtained from dopamine solution (1.55 nA), suggesting no contribution from ascorbate due to its irreversibility. Although a signal is observed at the collector in ascorbate solution alone, but due to the oxygen reduction as explained above, and not due to ascorbate redox cycling. A collection efficiency of 53.2% is obtained in the dopamine solution alone. The collection efficiency of 8.5% in the mixture of dopamine and ascorbate is due to the recycling of dopamine at the collector and has no contribution from ascorbate. The collection efficiency, when recalculated for the dopamine and ascorbate mixture after removing the ascorbate contribution (14.80 nA) from the total generator current (19.85 nA), comes out to be 33.2%. This decrease in collection efficiency of dopamine in presence of ascorbate is due to the electrocatalytic reaction between ascorbate and dopamine-quinone.

A calibration curve for dopamine in presence and absence of 100 μM ascorbate was prepared (shown in Figure 3.8) with and without redox cycling using the outer 14 generators (bands 2-8 and 13-19) and flanked by the inner four collectors (bands 9-12). From this point onward a-CSF buffer (pH 7.4) was used. aCSF buffer more closely mimics the composition of the extracellular fluid in the brain. Therefore, determination of detection limits in aCSF buffer would provide us a better picture of results, allowing us to predict the outcome in a real environment. The data show a linear correlation of current with dopamine concentration (all having R^2 values of ≥ 0.99). The non-zero y-intercept for the plot of the generator current is due

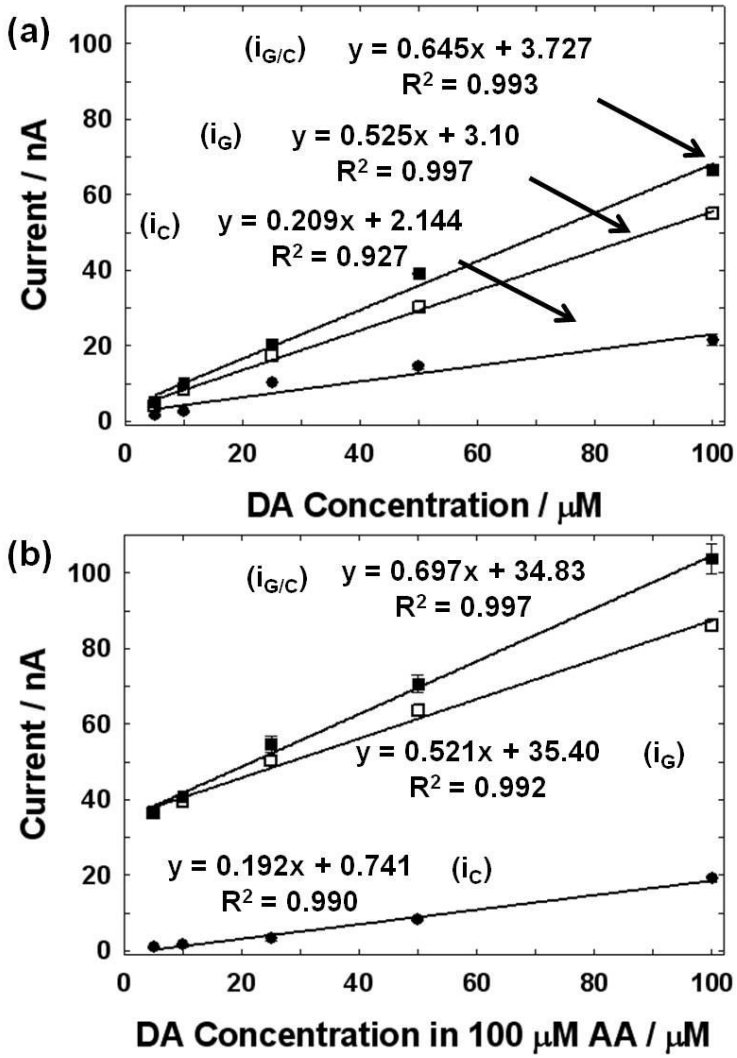

Figure 3.8. Calibration curves of current as a function of concentration for (a) dopamine in a-CSF buffer and (b) dopamine in presence of 100 μM ascorbate in a-CSF buffer, shown in the absence (generator, open squares, i_G) and in the presence (generator, closed squares, $i_{G/C}$ and collector, closed circles, i_C) of redox cycling using chronoamperometry at the microband MEA with the outer 14 generators (bands 2-8 and 13-19) flanking the inner 4 collectors (bands 9-13). The large non-zero y-intercept at the generators in (b), but not observed for the collectors, is due to the electrochemical response of the 100 μM ascorbate (35 nA), which is present in all of the solutions.

to the presence of 100 µM ascorbate, which is present in all of the solutions used to produce this calibration curve, adding an offset of 35 nA.

Addition of 35 nA current signal from 100 µM ascorbate to the dopamine current results in 8% increase in the sensitivity at the generator during redox cycling (0.645 $nA\mu M^{-1}$ for dopamine solution; 0.697 $nA\mu M^{-1}$ for dopamine and ascorbate mixture) and 1% decrease in the sensitivity at the generator without redox cycling (0.525 $nA\mu M^{-1}$ for dopamine solution; 0.521 $nA\mu M^{-1}$ for dopamine and ascorbate mixture). An 8% decrease is observed in slope of the calibration curve obtained at the collector (0.209 $nA\mu M^{-1}$ for dopamine solution; 0.192 $nA\mu M^{-1}$ for dopamine and ascorbate mixture). The amplification of 1.34 is obtained at the slope of the calibration curve of dopamine and ascorbate mixture at the generator in presence of redox cycling over that in the absence of redox cycling. The slope of the calibration curve at the collector observes the collection efficiency of 27.5%. Several reasons contribute to the low collection efficiency: the presence of the excess of ascorbate which contributes a huge signal at the generator, but not collector; the reaction between ascorbate and dopamine-quinone decreasing a signal at the collector; the large ratio of the generator to collector area (3.5:1) caused a much greater signal at the generator compared to the signal at the collector.

The detection limit of dopamine at the generator without redox cycling (107.2 ± 3.4 nM) was better than with redox cycling: 66% of that with redox cycling (163.1 ± 7.8 nM) and 25% of that at the collector (416.9 ± 67.50 nM), as explained above. The detection limit of dopamine in the presence of 100 µM ascorbate was 454.4 ± 26.34 nM with redox cycling at the collector. Even with the limitation of the instrumentation to filter out the noise at the collector (secondary working channel), redox cycling allows detection of dopamine in the submicromolar range. With the provision of better instrumentation, and MEA devices with smaller gaps (< 4 µm) between

adjacent electrodes, the detection limit should improve further. The standard deviation of the detection limit is calculated by multiplying the LOD with the ratio of the standard deviation of the slope to the slope itself.

3.4.3 Redox cycling of dopamine in presence of DOPAC. Redox cycling of dopamine in presence of DOPAC was not successful at bare gold electrodes. When compared to dopamine, redox cycling showed 45% sensitivity toward DOPAC at the generator as did the cyclic voltammetry, and 50% sensitivity at the collector. The redox cycling of dopamine in presence of DOPAC was therefore tried on electrodes coated with Nafion. Nafion should exclude both DOPAC and ascorbate because of their negative charge at the physiological pH. Exclusion of ascorbate should also suppress the spontaneous reaction between ascorbate and DAQ, increasing the collector sensitivity. In addition, dopamine is known to concentrate within Nafion from ion exchange because of its positive charge. However, the slower diffusion coefficients would be a tradeoff, diminishing the signal.

Nafion was spin-coated at the surface of MEA at 3000 rpm to provide a final thickness of 500 nm (measured using the profilometer). Figure 3.9 shows the resulting CA responses in the absence and presence of redox cycling for solutions containing DOPAC. The signal from 20 µM DOPAC at both the generator and collector had been eliminated. However, Nafion selectively allowed dopamine to permeate to the electrode surfaces via ion exchange with the counter ion Na^+. There is an ion exchange equilibrium (based upon Donnan equilibrium) constant between DA^+ and other cations in the solution. Thus, a combination of redox cycling with polymer coating such as Nafion would achieve the required selectivity for dopamine in presence of such anionic interferences. With a thickness of 500 nm, collector current during redox cycling began to appear 2.5 seconds. This poor temporal resolution that would be inadequate to capture the fast

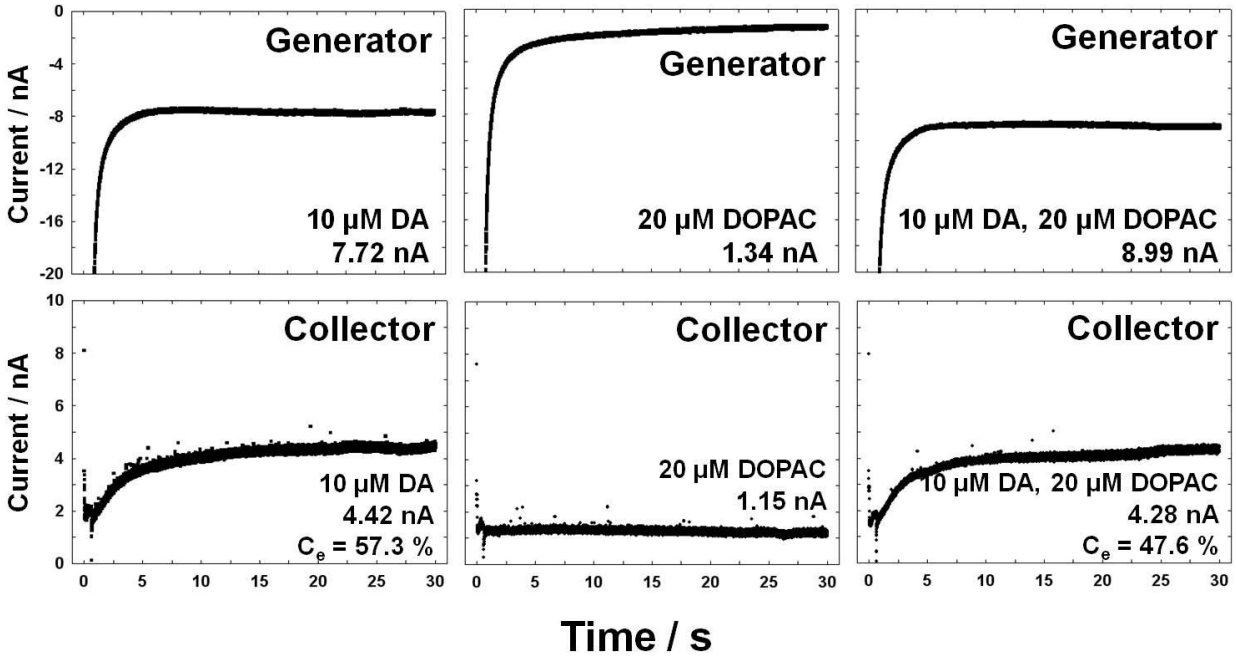

Figure 3.9. Comparison of electrochemical response obtained through redox cycling for 10 µM dopamine, 20 µM DOPAC and their mixture in a-CSF buffer (pH 7.4) at band MEA coated with 500 nm thick layer of Nafion with 9 pairs of alternating generator collector arrangement of electrodes recorded at 0.01 V/s scan rate. Generator was held at 0.5 V and collector at – 0.2 V.

transients in vivo should be offset by a much thinner layer of Nafion (though faster spin rates and diluting the polymer solution to make it less viscous) to obtain a better response time. The thinner film would allow dopamine to reach the surface of the MEA in less time, and dopamine-quinone to exit the film via ion exchange so that it can travel quickly through solution to the collector. A decrease in Nafion thickness by a factor of 5 should improve the temporal resolution by a factor of 25 because diffusion length is proportional to the square root of time. The diffusion coefficient of dopamine in Nafion is 2 x 10^{-9} cm^2/s[11, 19] and the average diffusion distance between generator and collector is estimated by Niwa et al to be[11]

$$d = 0.232w + g \qquad (2)$$

where w is the width of the electrode (4 µm) and g is the gap between the electrodes (4 µm). Thus it is estimated that the oxidized form of dopamine, dopamine-quinone will take ~ 60 s to diffuse from the generator to the collector in 100 nm thick Nafion layer. On the other hand, it will take only about 0.1 s to diffuse from the generator to the bulk through Nafion and then back to collector.

An attempt was made to coat a layer of Nafion on MEA with different thicknesses and test those layers for the response time of redox cycling. The thickness of Nafion layer varies between 500 nm to 350 nm at spin speeds of 1000 rpm to 3000 rpm, which might not provide the required response time. The data is shown in Tables 3.1 and 3.2. 1:1 and 1:9 dilution of Nafion with ethanol provided a final thickness of 250 nm and 50 nm thick layer on MEA when coated at 6000 rpm.

CV and redox cycling experiments were done on 1:1 and 1:9 (dilution by volume using ethanol) Nafion coated MEA using a model compound (1 mM $K_4Fe(CN)_6$ in a-CSF buffer) and solutions of dopamine, DOPAC and ascorbate in a-CSF buffer as well as their mixture. The

Table 3.1. Thicknesses of Nafion coated at different spin speeds on MEAs. The Nafion thickness was measured using DekTak profilometer tool.

Spin speed	**RPM**	**1000**	**2000**	**25000**	**4000**	**6000**
Thickness	**µm**	0.4527	0.4850	0.4201	0.3349	0.2045
		0.542	0.5259	0.4081	0.2800	0.1951
		0.5141	0.5187	0.3970	0.2990	0.2207
		0.5303	0.5296	0.3949	0.2500	0.1960
		0.5941	0.5230	0.3621	0.3623	0.2213
Average	**µm**	**0.5266**	**0.5164**	**0.3964**	**0.3052**	**0.2075**
STD	**µm**	**0.0511**	**0.0180**	**0.0217**	**0.0443**	**0.0128**

Table 3.2. Thicknesses of Nafion diluted with 200 proof ethanol coated at different spin speeds on MEAs. The Nafion thickness was measured using DekTak profilometer tool after ensuring the drying of Nafion layer and the complete evaporation of ethanol. As the Nafion layer gets thinner, the error in the measurement of its thickness increases. Because the profilometer tool is not kept on an isolation table which increases the amount of vibration received by the instrument, its spatial resolution is limited to 100 nm.

Dilution		**1:02**	**1:02**	**1:10**
Spin speed	**RPM**	**1250**	**4000**	**4000**
Thickness	**nm**	325.3	298.0	61.6
		286.0	198.7	26.6
		326.5	321.2	55.1
		368.5	207.6	21.8
			204.6	24.6
Average	**nm**	**326.6**	**246.0**	**37.9**
STD	**nm**	**33.7**	**58.7**	**18.9**

control experiments were done where the MEA were not coated with Nafion. At this point Nafion layer is permeable to all the species and was not selective toward dopamine alone. Ferrocyanide, $[Fe(CN)_6]^{4-}$ is a huge compound and carries 4 - charge. Thus it should not permeate through a defect free layer of Nafion and should not provide any electrochemical signal above the background. However, a weak signal due to the presence of ferrocyanide was observed on Nafion coated MEA. Similar was the case with ascorbate and DOPAC. They both are also negatively charged at pH 7.4. Although the signal is much weaker when compared to the signal obtained in the absence of Nafion, its weak presence suggests that there were wholes or defects in the Nafion layers. They could have been left behind after the evaporation of ethanol.

More work is required at this point to improve the uniformity of Nafion layer in our system. The reagent used for the dilution of Nafion can also be varied such as methanol or isopropanol instead of ethanol. Different methods of curing Nafion can be explored. Selective detection of dopamine on electrodes coated with Nafion is possible as has been shown by other people. The diffusion of dopamine in Nafion decreases by a factor of 10^4. This increases the diffusion time of dopamine between the electrodes, decreasing the number of redox cycles and the amplification. Because of this, some scientists have used two polymer layers: Nafion as a top layer to increase selectivity toward dopamine and a bottom polymer layer to facilitate electrochemistry of dopamine without decreasing its diffusion coefficient. Thus, use of two polymer layers can be explored in redox cycling systems for improving detection limit of dopamine.

3.5 CONCLUSIONS

Redox cycling is an effective electrochemical method to detect physiological concentration of dopamine in presence of up to 100 times excess ascorbate without the requirement of any electrode modification method. However electrode modification (coating with Nafion) was required for the elimination of DOPAC signal. Nafion layer used at this point is too thick and slows down the initiation of redox cycling because it requires a long time for dopamine to diffuse through the layer of 500 nm Nafion and reach the electrode surface. A thinner layer of Nafion together with redox cycling can achieve the required sensitivity and selectivity to detect physiological concentration of dopamine in presence of interferences. There will be a need in future to explore other potentials at generator and collector electrodes, as well as surface modification methods in addition to eliminate electrochemically reversible interferences such as DOPAC in redox cycling. Such methods will also improve detection limits and decrease electrode fouling as observed during the use of higher concentrations of ascorbate over prolonged periods of time.

With the increasing use of electrochemical detection methods, dopamine is now known to be found in micromolar concentrations.[51] This paper demonstrates successful use of redox cycling for discriminating dopamine from ascorbate and DOPAC at respective physiologically relevant concentrations. Complications such as background subtraction are also eliminated. With further improvement in the instrumentation, such as filtration of noise at secondary working channels and while working in dual electrode mode, detection limit should further improve, especially at the collector. This study shows that with certain modifications and improvements in the existing set up, redox cycling has great scope for in vivo experiments and real environment

(such as tissue sample) testing. By avoiding complications of background subtraction, new kinds of neurophysiological information (e.g. basal dopamine levels) should be accessible.

3.6 ACKNOWLEDGEMENTS

Funding has been provided in part by the National Science Foundation (CHE-0719097) and the Arkansas Biosciences Institute, the major research component of the Arkansas Tobacco Settlement Proceeds Act of 2000. We thank Errol Porter for advice on microfabrication. The use of the High Density Electronics Center microfabrication facilities is also acknowledged. We express our appreciation to Professor Adrian Michael of the University of Pittsburgh for insightful discussions about applications.

3.7 REFERENCES

(1) Borland, L. M.; Michael, A. C. *Journal of Neurochemistry* **2004**, *91*, 220-229.

(2) Borland, L. M.; Shi, G. Y.; Yang, H.; Michael, A. C. *Journal of Neuroscience Methods* **2005**, *146*, 149-158.

(3) Bungay, P. M.; Newton-Vinson, P.; Isele, W.; Garris, P. A.; Justice, J. B. *Journal of Neurochemistry* **2003**, *86*, 932-946.

(4) Kulagina, N. V.; Zigmond, M. J.; Michael, A. C. *Neuroscience* **2001**, *102*, 121-128.

(5) Cullison, J. K.; Waraska, J.; Buttaro, D. J.; Acworth, I. N.; Bowers, M. L. *Journal of Pharmaceutical and Biomedical Analysis* **1999**, *19*, 253-259.

(6) Dam, V. A. T.; Olthuis, W.; van den Berg, A. *Analyst* **2007**, *132*, 365-370.

(7) Katelhon, E.; Hofmann, B.; Lemay, S. G.; Zevenbergen, M. A. G.; Offenhausser, A.; Wolfrum, B. *Analytical Chemistry* **2010**, *82*, 8502-8509.

(8) Liu, Z. M.; Niwa, O.; Kurita, R.; Horiuchi, T. *Analytical Chemistry* **2000**, *72*, 1315-1321.

(9) Niwa, O.; Morita, M. *Analytical Chemistry* **1996**, *68*, 355-359.

(10) Niwa, O.; Morita, M.; Tabei, H. *Electroanalysis* **1991**, *3*, 163-168.

(11) Niwa, O.; Morita, M.; Tabei, H. *Electroanalysis* **1994**, *6*, 237-243.

(12) Niwa, O.; Tabei, H. *Analytical Chemistry* **1994**, *66*, 285-289.

(13) Benes, F. M. *Trends in Pharmacological Sciences* **2001**, *22*, 46-47.

(14) Wishart, D. S.; Knox, C.; Guo, A. C.; Eisner, R.; Young, N.; Gautam, B.; Hau, D. D.; Psychogios, N.; Dong, E.; Bouatra, S.; Mandal, R.; Sinelnikov, I.; Xia, J. G.; Jia, L.; Cruz, J. A.; Lim, E.; Sobsey, C. A.; Shrivastava, S.; Huang, P.; Liu, P.; Fang, L.; Peng, J.; Fradette, R.; Cheng, D.; Tzur, D.; Clements, M.; Lewis, A.; De Souza, A.; Zuniga, A.; Dawe, M.; Xiong, Y. P.; Clive, D.; Greiner, R.; Nazyrova, A.; Shaykhutdinov, R.; Li, L.; Vogel, H. J.; Forsythe, I. *Nucleic Acids Research* **2009**, *37*, D603-D610.

(15) Redgrave, P.; Gurney, K. *Nature Reviews Neuroscience* **2006**, *7*, 967-975.

(16) Salgado-Pineda, P.; Delaveau, P.; Blin, O.; Nieoullon, A. *Clinical Neuropharmacology* **2005**, *28*, 228-237.

(17) Schultz, W. *Annual Review of Neuroscience* **2007**, *30*, 259-288.

(18) Obata, T. *Journal of Neural Transmission* **2002**, *109*, 1159-1180.

(19) Wightman, R. M.; May, L. J.; Michael, A. C. *Analytical Chemistry* **1988**, *60*, A769-&.

(20) Bibb, J. A.; Yan, Z.; Svenningsson, P.; Snyder, G. L.; Pieribone, V. A.; Horiuchi, A.; Nairn, A. C.; Messer, A.; Greengard, P. *Proceedings of the National Academy of Sciences of the United States of America* **2000**, *97*, 6809-6814.

(21) Phillips, P. E. M.; Stuber, G. D.; Heien, M.; Wightman, R. M.; Carelli, R. M. *Nature* **2003**, *422*, 614-618.

(22) Koob, G. F.; Bloom, F. E. *Science* **1988**, *242*, 715-723.

(23) Mink, J. W. *Pediatric Neurology* **2001**, *25*, 190-198.

(24) Grace, A. A. *Neuroscience* **1991**, *41*, 1-24.

(25) Salahpour, A.; Ramsey, A. J.; Medvedev, I. O.; Kile, B.; Sotnikova, T. D.; Holmstrand, E.; Ghisi, V.; Nicholls, P. J.; Wong, L.; Murphy, K.; Sesack, S. R.; Wightman, R. M.; Gainetdinov, R. R.; Caron, M. G. *Proceedings of the National Academy of Sciences of the United States of America* **2008**, *105*, 4405-4410.

(26) Venton, B. J.; Michael, D. J.; Wightman, R. M. *Journal of Neurochemistry* **2003**, *84*, 373-381.

(27) Binfare, R. W.; Rosa, A. O.; Lobato, K. R.; Santos, A. R. S.; Rodrigues, A. L. S. *Progress in Neuro-Psychopharmacology & Biological Psychiatry* **2009**, *33*, 530-540.

(28) Grunewald, R. A. *Brain Research Reviews* **1993**, *18*, 123-133.

(29) Rice, M. E. *Trends in Neurosciences* **2000**, *23*, 209-216.

(30) Stamford, J. A.; Kruk, Z. L.; Millar, J. *Brain Research* **1984**, *299*, 289-295.

(31) Robinson, D. L.; Hermans, A.; Seipel, A. T.; Wightman, R. M. *Chemical Reviews* **2008**, *108*, 2554-2584.

(32) Popa, E.; Notsu, H.; Miwa, T.; Tryk, D. A.; Fujishima, A. *Electrochemical and Solid State Letters* **1999**, *2*, 49-51.

(33) Oneill, R. D. *Analyst* **1994**, *119*, 767-779.

(34) Niwa, O.; Kurita, R.; Liu, Z. M.; Horiuchi, T.; Torimitsue, K. *Analytical Chemistry* **2000**, *72*, 949-955.

(35) Peng, W. F.; Wang, E. K. *Analytica Chimica Acta* **1993**, *281*, 663-671.

(36) Vandaveer, W. R.; Woodward, D. J.; Fritsch, I. *Electrochimica Acta* **2003**, *48*, 3341-3348.

(37) Niwa, O.; Morita, M.; Tabei, H. *Journal of Electroanalytical Chemistry* **1989**, *267*, 291-297.

(38) Niwa, O.; Morita, M.; Tabei, H. *Analytical Chemistry* **1990**, *62*, 447-452.

(39) Adams, R. N.; Conti, J.; Marsden, C. A.; Strope, E. *British Journal of Pharmacology* **1978**, *64*, P470-P471.

(40) Hoffman, A. F.; Gerhardt, G. A. *Journal of Neurochemistry* **1998**, *70*, 179-189.

(41) Miller, A. D.; Forster, G. L.; Yeomans, J. S.; Blaha, C. D. *Neuroscience* **2005**, *136*, 531-538.

(42) Unger, E. L.; Eve, D. J.; Perez, X. A.; Reichenbach, D. K.; Xu, Y. Q.; Lee, M. K.; Andrews, A. M. *Neurobiology of Disease* **2006**, *21*, 431-443.

(43) Venton, B. J.; Troyer, K. P.; Wightman, R. M. *Analytical Chemistry* **2002**, *74*, 539-546.

(44) Bath, B. D.; Michael, D. J.; Trafton, B. J.; Joseph, J. D.; Runnels, P. L.; Wightman, R. M. *Analytical Chemistry* **2000**, *72*, 5994-6002.

(45) Pihel, K.; Walker, Q. D.; Wightman, R. M. *Analytical Chemistry* **1996**, *68*, 2084-2089.

(46) Clapp-Lilly, K. L.; Roberts, R. C.; Duffy, L. K.; Irons, K. P.; Hu, Y.; Drew, K. L. *Journal of Neuroscience Methods* **1999**, *90*, 129-142.

(47) Mitala, C. M.; Wang, Y. X.; Borland, L. M.; Jung, M.; Shand, S.; Watkins, S.; Weber, S. G.; Michael, A. C. *Journal of Neuroscience Methods* **2008**, *174*, 177-185.

(48) Peters, J. L.; Miner, L. H.; Michael, A. C.; Sesack, S. R. *Journal of Neuroscience Methods* **2004**, *137*, 9-23.

(49) Zhou, F.; Zhu, X. W.; Castellani, R. J.; Stimmelmayr, R.; Perry, G.; Smith, M. A.; Drew, K. L. *American Journal of Pathology* **2001**, *158*, 2145-2151.

(50) Venton, B. J.; Robinson, T. E.; Kennedy, R. T.; Maren, S. *European Journal of Neuroscience* **2006**, *23*, 3391-3398.

(51) Michael, A. C.; Borland, L. M.; Mitala, J. J.; Willoughby, B. M.; Motzko, C. M. *Journal of Neurochemistry* **2005**, *94*, 1202-1211.

(52) Gronbeck, H.; Hakkinen, H.; Whetten, R. L. *Journal of Physical Chemistry C* **2008**, *112*, 15940-15942.

(53) Kautz, N. A.; Kandel, S. A. *Journal of the American Chemical Society* **2008**, *130*, 6908-+.

(54) Walter, M.; Akola, J.; Lopez-Acevedo, O.; Jadzinsky, P. D.; Calero, G.; Ackerson, C. J.; Whetten, R. L.; Gronbeck, H.; Hakkinen, H. *Proceedings of the National Academy of Sciences of the United States of America* **2008**, *105*, 9157-9162.

(55) Yu, M.; Bovet, N.; Satterley, C. J.; Bengio, S.; Lovelock, K. R. J.; Milligan, P. K.; Jones, R. G.; Woodruff, D. P.; Dhanak, V. *Physical Review Letters* **2006**, *97*.

(56) Bruno, J. P.; Gash, C.; Martin, B.; Zmarowski, A.; Pomerleau, F.; Burmeister, J.; Huettl, P.; Gerhardt, G. A. *European Journal of Neuroscience* **2006**, *24*, 2749-2757.

(57) Bruno, J. P.; Sarter, M.; Gash, C.; Parikh, V. *Choline- and Acetylcholine-Sensitive Microelectrodes*; American Scientific Publishers, 2006b.

(58) Burmeister, J. J.; Pomerleau, F.; Huettl, P.; Gash, C. R.; Wemer, C. E.; Bruno, J. P.; Gerhardt, G. A. *Biosensors & Bioelectronics* **2008**, *23*, 1382-1389.

(59) Huang, X. J.; O'Mahony, A. M.; Compton, R. G. *Small* **2009**, *5*, 776-788.

(60) Huong, V. T.; Shimanouchi, T.; Quan, D. P.; Umakoshi, H.; Viet, P. H.; Kuboi, R. *Journal of Applied Electrochemistry* **2009**, *39*, 2035-2042.

(61) Ju, H. X.; Ni, J. G.; Gong, Y.; Chen, H. Y.; Leech, D. *Analytical Letters* **1999**, *32*, 2951-2964.

(62) Gerhardt, G. A.; Oke, A. F.; Nagy, G.; Moghaddam, B.; Adams, R. N. *Brain Research* **1984**, *290*, 390-395.

(63) Bartsch, R. A.; Way, J. D. *Chemical separations with liquid membranes*; Washington, DC : American Chemical Society, c1996, 1996.

(64) Rocha, L. S.; Carapuca, H. M. *Bioelectrochemistry* **2006**, *69*, 258-266.

(65) Szentirmay, M. N.; Martin, C. R. *Analytical Chemistry* **1984**, *56*, 1898-1902.

(66) Nicholson, C.; Rice, M. E. *In Volume Transmission in the Brain: Novel Mechanisms for Neural Transmission* Raven Press, New York, 1991.

(67) Dalmia, A.; Liu, C. C.; Savinell, R. F. *Journal of Electroanalytical Chemistry* **1997**, *430*, 205-214.

(68) Kurzatkowska, K.; Dolusic, E.; Dehaen, W.; Sieron-Stoltny, K.; Sieron, A.; Radecka, H. *Analytical Chemistry* **2009**, *81*, 7397-7405.

(69) Gao, Z. Q.; Huang, H. *Chemical Communications* **1998**, 2107-2108.

(70) Yu, A. M.; Sun, D. M.; Chen, H. Y. *Analytical Letters* **1997**, *30*, 1643-1652.

(71) Alwarappan, S.; Prabhulkar, S.; Durygin, A.; Li, C. Z. *Journal of Nanoscience and Nanotechnology* **2009**, *9*, 2991-2996.

(72) Gonon, F.; Buda, M.; Cespuglio, R.; Jouvet, M.; Pujol, J. F. *Nature* **1980**, *286*, 902-904.

(73) Gonon, F.; Buda, M.; Cespuglio, R.; Jouvet, M.; Pujol, J. F. *Brain Research* **1981**, *223*, 69-80.

(74) Heien, M.; Johnson, M. A.; Wightman, R. M. *Analytical Chemistry* **2004**, *76*, 5697-5704.

(75) Kawagoe, K. T.; Zimmerman, J. B.; Wightman, R. M. *Journal of Neuroscience Methods* **1993**, *48*, 225-240.

(76) Takmakov, P.; Zachek, M. K.; Keithley, R. B.; Bucher, E. S.; McCarty, G. S.; Wightman, R. M. *Analytical Chemistry* **2010**, *82*, 9892-9900.

(77) Hsueh, C. C.; Brajtertoth, A. *Analytical Chemistry* **1994**, *66*, 2458-2464.

(78) Wang, J.; Pamidi, P. V. A.; Cepria, G.; Basak, S.; Rajeshwar, K. *Analyst* **1997**, *122*, 981-984.

(79) Witkowski, A.; Brajtertoth, A. *Analytical Chemistry* **1992**, *64*, 635-641.

(80) Aggarwal, A.; Fritsch, I. *Journal of Electroanalytical Chemistry, To be submitted.* .

(81) Hawley, M. D.; Tatawawa.Sv; Piekarsk.S; Adams, R. N. *Journal of the American Chemical Society* **1967**, *89*, 447-&.

(82) Ciolkowski, E. L.; Cooper, B. R.; Jankowski, J. A.; Jorgenson, J. W.; Wightman, R. M. *Journal of the American Chemical Society* **1992**, *114*, 2815-2821.

(83) Ranganathan, S.; McCreery, R.; Majji, S. M.; Madou, M. *Journal of the Electrochemical Society* **2000**, *147*, 277-282.

4. MICROFABRICATION AND CHARACTERIZATION OF INTERDIGITATED MICROELECTRODE PROBE ARRAYS FOR REDOX CYCLING

4.1 ABSTRACT

Five different designs having two different parameters for small sized microelectrode interdigitated array (IDA) probe sensors were microfabricated with the ultimate goal of performing in vivo dopamine detection. Characterization and calibration curves were obtained using a model compound, hexaammineruthenium (III) chloride. The microfabrication procedure provided high yield and reproducibility for the IDAs (4.45% relative standard deviation, RSD, 15 IDAs, single wafer). Characterization studies with the model compound show a decrease in the sensitivity of redox cycling by a factor of 16 compared to a band MEA and 3 compared to a ring MEA due to the decreased electrochemical area in comparison to chips reported previously (IDA generator areas are 1/10 of that of band and ½ of that of ring MEAs; IDA collector areas are 1/15 of that of band and ½ of that of ring MEA). Detection limits for the design 'E' with mixed arrangement of generator collector electrodes is 532 ± 18.1 nM at the collector electrode in $[Ru(NH_3)_6]^{3+}$ in 0.5 M KCl. Dopamine studies still need to be performed on these IDAs. Theoretical calculations predict that the probes should be able to detect dopamine at least to the single digit micromolar concentrations with minor modifications, which include decreasing the spacing between the electrodes from 4 μm to 0.5 μm or less. Thin film processing facilities (HiDEC) can provide down to 2-μm resolution at present and will be able to provide resolution down to 0.1 μm with the inclusion of an electron beam writer in their facility in November, 2011.

4.2 INTRODUCTION

In Chapter 3, redox cycling was shown to be capable of detecting dopamine at physiological concentration in presence of at least up to 100 times excess ascorbate and has also shown potential for improvement in sensitivity as well as selectivity. However, to be useful, a sensor needs to exhibit similar results in a real environment (i.e. for brain insertion studies). It is now important to replicate the results obtained in previous chapters on a miniaturized system the dimensions of which are compatible with tissue insertion studies. Probes having tapered tips and with different design and dimensions of the array were designed in order to prepare for the above-mentioned studies. Microfabrication procedures were developed for the miniaturized designs.

The amplification and collection efficiency in a redox cycling experiment depends on the ability to bring down the interelectrode distance and use a geometry and electrode size so that recycling is optimized. Also, small feature sizes ensure miniaturization of the sensor which is critical for in vivo studies. Microlithograpical patterning of metal electrodes on a silicon substrate allows both for small feature sizes and cost effectiveness compared to other available technologies. This project is dependent on tapping into the advantages offered by silicon technology available in High Density Electronic Center at the University of Arkansas. The use of silicon technology made it flexible and viable to design as well as fine tune the sensors. The project also takes into account the deep reactive ion etching (DRIE) processes that are also available at HiDEC and will be used to etch the probes away from the bulk of the silicon substrate. Thus, the probes were designed and fabricated containing microelectrode interdigitated arrays (IDAs) with the focus on performing DRIE on them as the last step.

Different kinds of materials have been employed on MEAs as electrode components including metallic substrates and carbon materials.[9, 16, 17] Dopamine is well studied on carbon fiber electrodes. It is known to adsorb on the surface of carbon fibers at oxidizing potentials. Carbon fiber electrode exhibit minimal fouling in vivo compared to gold electrodes, which bind sulfur containing species. Their restriction to a single sensing site rules out the application of electrochemical techniques such as redox cycling for the detection of analyte. They cannot be inserted into the same brain region simultaneously for simultaneous detection of different analytes. Adoption of fabrication techniques for microelectrode arrays opens door to a variety of experimental set ups and allow advanced studies for analyses of same or different analytes in different or same brain regions simultaneously.

In vivo studies have been carried out on gold as well as on carbon arrays. Use of both materials involves a complementary trade off. While both gold and carbon electrodes are being considered as the electroactive material for the probe sensors, several factors need attention. Photoresist that is patterned using photolithography followed by pyrolysis at 800 °C-1000 °C in a reducing atmosphere (95% N_2 and 5% H_2) produces carbon electrodes.[16, 18, 19 20-22] Ceramics have the advantage of being electrochemically-controlled deposited with conducting polymers. Electrochemical stability of carbon in a biological environment makes it the material of choice. However, its fabrication and process challenges become increasingly difficult with feature sizes smaller than 20 µm.

Gold electrodes are easy to fabricate with the application of photolithographic processes. It is reported to be the most frequently used material for fabrication of MEAs.[23] The thin film processing facility at the University of Arkansas does not include pyrolysis capability to be able to fabricate carbon electrodes. Although a pyrolysis system can be set up in our own lab, it is

also apparent that the required electrode features (0.8 μm or less), whether gold or carbon, for our success will be much smaller than the resolution achievable by pyrolysis (> 2 μm).

In order to insert microfabricated multi-electrode devices into brain tissue, they need to be patterned on a substrate that is slender and minimizes tissue damage, such as those constructed previously on silicon daggers.[8] They are the focus of this project. As an advancement over previous reports, connections to silicon daggers can now be made through contact pads.[9] Although this development has reduced the complications of wire bonding involved for lab-based evaluation, fabrication of silicon probes is still difficult and time consuming.[11, 12] Silicon probes work best for very small electrode features such as 1 to 2 μm of lateral spacing and < 1 μm of vertical spacing of stacks, but photolithography remains expensive and time consuming.

Ceramics have been reported previously for such devices, but only as a substrate (backing material) on which routine photolithography defines the electrode sites.[7, 8, 13-15] They might have advantage over microlithography and micromachining of silicon chips due to fast, facile and inexpensive fabrication. Ceramic microstructures are difficult to fabricate compared to silicon. Different conductive pastes (carbon as well metal) can be screen printed on ceramics. However, the process of screen printing limits the spatial resolution to 50 μm; dimensions unsuitable for redox cycling.

DRIE is often used to create deep as well as steep holes or trenches in silicon wafers. It is anisotropic (i.e. directional) and can produce vertical walls (88º – 92º). DRIE can be done in two ways: cryogenic etching (the substrate is cooled down to chilling temperatures to minimize the rate of isotropic chemical etching) and the Bosch process (alternate between polymer deposition to cover the side walls and plasma etch).[1, 2] The Bosch process uses SF_6 for plasma etching and C_4F_8 for coating the walls with a polymer passivation layer. It can provide highly anisotrpoically

etched narrow silicon trenches with high aspect ratio (1:100).[1-6] The Bosch process will be used for etching of the fabricated probe like sensors (refer to section 4.4 and 4.5) from the substrate, requiring the aspect ratio of 1:10 (10 μm wide trench, 100 μm deep).

Typically reactive ion etching, dicing, or chemical etching is used to release the fabricated devices from the silicon substrate.[7-10] Sreenivas et al.[9] have used orientation dependent etching of the silicon to release the individual devices. The effect of the isotropic etching can be clearly seen on their devices. McCarty and co-workers have used deep reactive ion etching for the release of the sensor devices from the substrate.[10] DRIE reduces the amount of undercutting of the metal layer and/ or the substrate. It produces truly vertical walls, providing the as expected electrochemical area for the metal layer(s). It can be applied to smaller dimensions where the safety margin is tiny. As opposed to dicing such as using a diamond aw, DRIE does not suffer from non uniform edges or chipping of the edges. DRIE can be used to produce complex shapes that might be difficult to obtain with a dicing saw.

In the work described in this chapter, IDAs were fabricated onto silicon chips with lateral dimensions small enough (100 μm wide) for trial studies for insertion into tissue. Although presently the thickness of the substrate (600 μm) is much bigger than desired (100 μm), a process has been established to obtain the final desirable thickness. Due to space limitations on a probe, it would not be possible to fabricate more than 10 co-planar pairs of electrodes as individually addressable on a small chip that can be inserted into a tissue. Hence, the design is modified for interdigitated electrodes, containing two sets of active electrodes required for redox cycling. The electrode dimensions required to obtain our ultimate goal are achievable at HiDEC providing two micron resolution. Previous studies have revealed a direct correlation between collection efficiency and the number of generator-collector pairs. Thus, increasing the number of

generator-collector pairs in the final design will provide us better collector sensitivity and thus better dopamine detection limit.

4.3 EXPERIMENTAL

4.3.1 Chemicals and materials. Hexaammineruthenium (III) chloride (Alfa Aesar, MA, USA) and potassium chloride (EMD Chemical Inc., Darmstatd, Germany), both ACS grade, were used as received. Water, ACS reagent grade (≥ 18 MΩ-cm), was obtained from Ricca Chemical Co. (Arlington, TX).

125 cm diameter single crystal 625 ± 25 μm thick silicon wafer (N type, 1-0-0-orientation) with 2 μm ± 5% SiO_2 layer grown thermally on one side was commercially obtained (SQ 12775, Silicon Quest International, Inc., Santa Clara, CA). A gold bar with 99.99% purity was obtained from Credit Suisse and chromium plated tungsten rod (2 in. long x 0.050 in. diameter, CC/ION 40040) from Kurt J. Lesker Company. Chromium etchant (HTA enterprise, CEP 200), gold etchant (Transene, GE8148) were used as obtained.

4.3.2 Instrumentation. Dexon (acid) wet bench chemistries were used for wet etching processes. Dexon (caustic) wet bench chemistries were used for photo resist development. Edwards Auto 6 evaporator was used for thermal vapor deposition of Cr and Au layers on the wafers. Eaton 6000HX spin coater, Suss Microtec MA150 contact aligner with 2.5 μm resolution, Plasma Therm SLR 720 for RIE equipped with a turbo vacuum source and Surface technology Systems Advanced silicon etcher equipped with a an electrostatic chuck, helium backside cooling and a turbo high vacuum source were used during the microfabrication procedures.

4.3.3 Electrochemical studies. Experiments were carried out in triplicate on the same device throughout the study. To avoid compositional changes due to electrochemistry from one experiment to another, fresh solution was used each time. All electrochemical experiments were performed using cyclic voltammetry (CV) with a bipotentiostat equipped with a picoamp booster and a faraday cage (CHI 1030, CH Instruments, Austin, TX).

For redox cycling experiments, current at both electrodes were plotted as a function of potential at the generator. The potential range was swept at the generator (from +0.2 V to –0.3 V and back) and the collector was held at a constant potential (+0.2 V) versus Ag/AgCl (saturated KCl) reference electrode and platinum wire counter electrode. In order to determine the amplification factor, cyclic voltammetry was performed with the same generators, but with the electrodes assigned as collectors left at open circuit. Redox solution of $Ru(NH_3)_6Cl_3$ in 0.5 M KCl electrolyte was used. Unless otherwise stated, all currents reported in this manuscript are the absolute values of the difference between the peak or steady state current, whichever is larger, and the charging background. Generator current is cathodic and collector current is anodic. A small scan rate was chosen to provide a long enough time scale for redox species to diffuse to the neighboring electrodes and recycle at collector electrodes.

4.4 DESIGN OF IDA PROBE SENSORS

The band MEAs used in Chapters 2 and 3 contain 4 µm (width) x 2 mm (length) electrodes separated by 4 µm gaps. Each array contains 18 electrodes with the array dimensions > 140 µm x 2000 µm. These dimensions cannot be used for brain insertion studies. Based on recent results obtained by Michael et al.[24-30] and McCarty et al.[10, 31],100 µm (wide) x 100 µm (thick) x 4 mm (long) was the agreed-upon implantable size of the probe shaft. The smaller size

would further minimize tissue damage. However, at this point the focus of this project is on fabricating probes as small as practicable. Electrodes too small will have less electrochemical area and will provide worse detection limits. Up to 200 µm long electrodes seem to work well in anesthetized rats.[30]

Combining the parameters described above and the knowledge gained from studies described in the previous two chapters, interdigitated microelectrode arrays (IDAs) contained in a space suitable for probe like sensors were designed. Their AutoCAD designs are shown in Figure 4.1. Each sensor contains one IDA. There are a total of 5 sensor designs. Two of them come in two different sizes (to make four). The remaining design was only made with the smaller area. The larger IDAs (260 µm in length and width) were designed to ensure the ease and success of fabrication at HiDEC. Smaller IDAs (260 µm in length and 100 µm in width) were designed for the ease of the tissue insertion process. Should the IDAs detect dopamine at least to 1 µM concentration and fabrication of the probe-shape is successful, they will be tested for dopamine detection in rat brain by our collaborators.

The alternating generator-collector configuration of electrodes (Design C) was chosen because it showed higher amplification and improved collection efficiency compared to other arrangement of electrodes (Chapter 2). It is therefore of interest to test this arrangement at smaller dimensions. At this point of time, the alternating design has not been tested because the arrangement failed to detect dopamine in presence of excess of ascorbate in chapter 3.

Generators flanking a central collector exhibited successful detection of dopamine and elimination of the interference of up to 100 times excess ascorbate. Therefore, a smaller size of this configuration (Design A with large dimensions and Design D with smaller dimensions) was designed with future in vivo experiments in mind. A third arrangement of electrodes (Design B

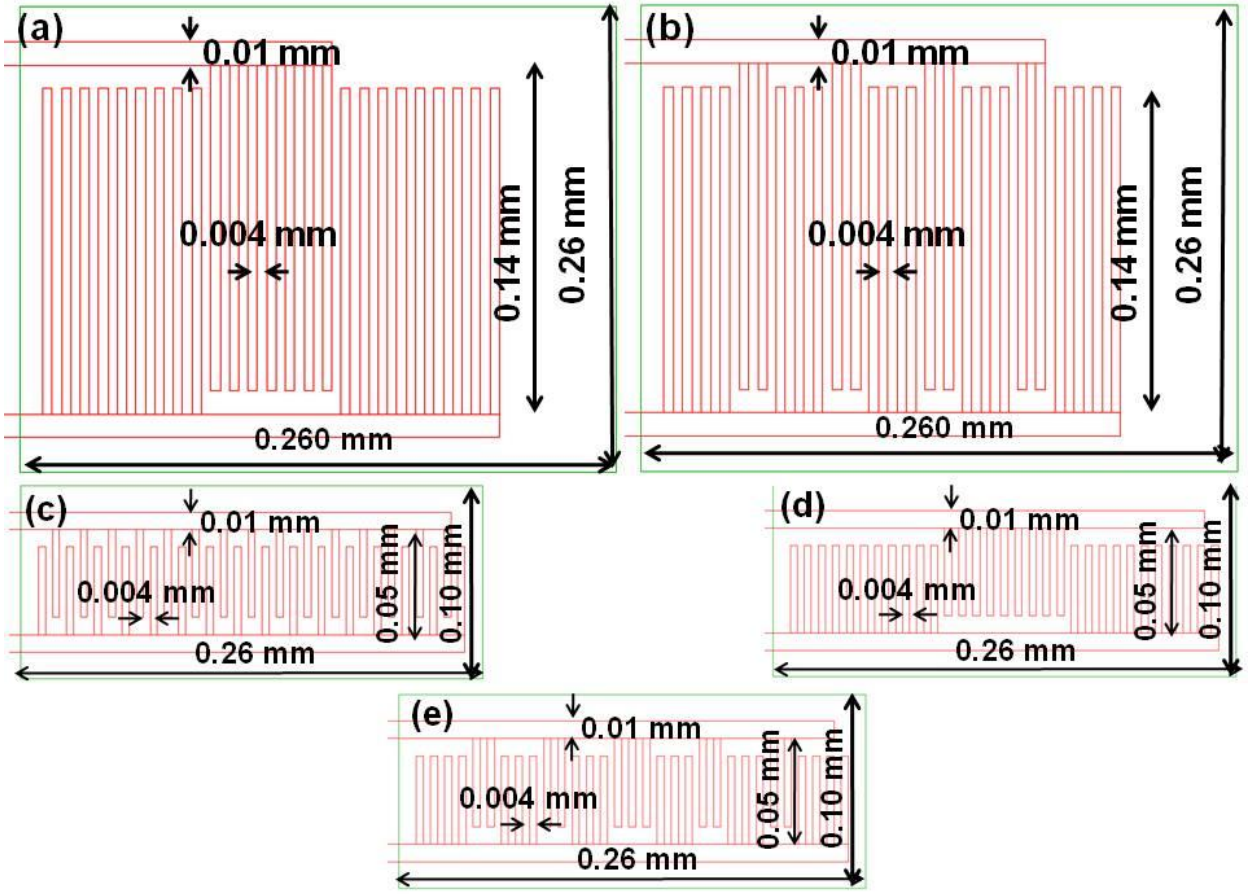

Figure 4.1. Designs of interdigitated microelectrode arrays (IDA) contained in probe like sensors containing one set of generator electrode and one set of collector electrode each with different configurations are shown. (a) Design A: 260 µm x 260 µm IDA contains generator flanking central collector configuration; (b) Design B: 260 µm x 260 µm IDA contains mixed arrangement of generator and collector configuration; (c) Design C: 260 µm x 100 µm IDA contains alternating generator collector configuration; (d) Design D: 260 µm x 100 µm IDA contains generator flanking central collector configuration; (e) Design E: 260 µm x 100 µm IDA contains mixed arrangement of generator and collector configuration. These are the AutoCAD designs drawn to-scale.

with large dimensions and Design E with small dimensions), mixed arrangement of generator collector electrodes, is a rearrangement of Designs C and D. It contains 4 pairs of central collectors, each surrounded by generator on either side. It is hypothesized that this configuration will consume ascorbate more efficiently due to the spatial arrangement of the generator elements, while providing better detection limits of dopamine than Designs C and D. For the mixed arrangement of electrodes where multiple individual bands adjacent to each other are shorted together to form a single generator or collector, microelectrode elements of 4 μm width and gap were created instead of a single giant electrode. This does not affect the amplification or the collection efficiency during redox cycling, but lowers the background charging current. This is especially important when both fast scan cyclic voltammetry (where charging current is a large problem) and redox cycling will be compared on the same probe and in the same location of brain tissue as part of the future validation process. Also, a lower double layer capacitance improves the time response (the RC time constant).

Figure 4.2 shows the general layout of a probe sensor containing an IDA. Sensors of dimensions as small as 100 μm critical dimension are not uncommon in the industry, but have not been fabricated before at HiDEC. The sensors evaluated here were fabricated on 600 μm thick silicon substrate. A process still needs to be established for the thinning of the final product to 100 μm. Some strategies to do so have been published by others. The fabrication process adds stress on the substrate and the features contained on the substrate at each step. Small feature size adds to the complications. Therefore, for the purposes of initial in vitro evaluation, the sensors were designed here with practical dimensions that are sustained through the entire process of their development and allow us to test and establish the protocol.

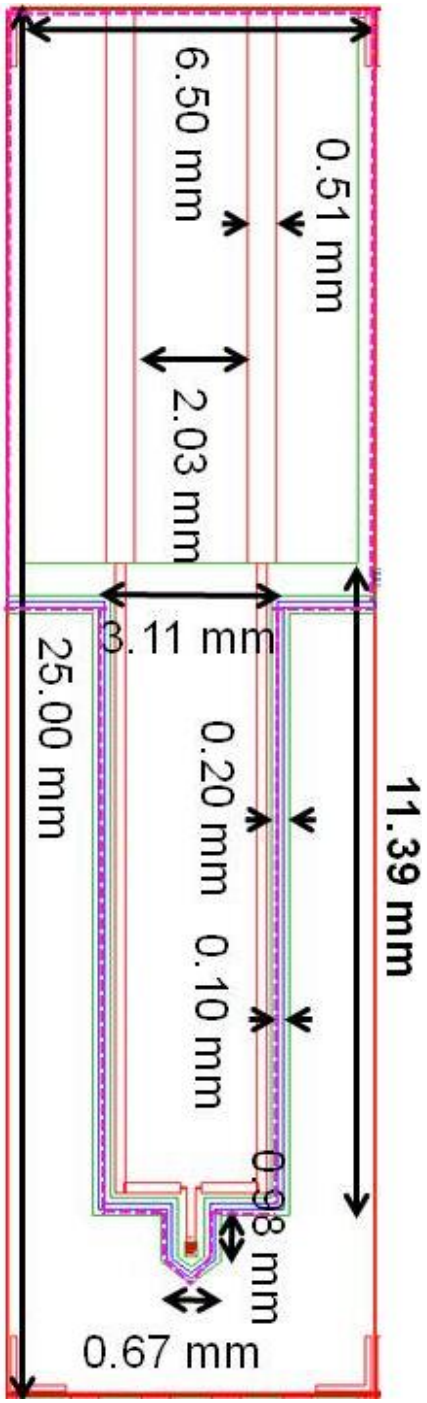

Figure 4.2. General design of the probe sensor containing 260 µm x 260 µm IDA. The width of the shaft after release from the wafer will be 670 µm. Deep reactive ion etching will be used to release the individual sensors from the substrates. After release, the sensors will take the probe shape as outlined by the pink dotted line. The AutoCAD design is drawn to scale.

Silicon sensor when reduced to 100 µm x 100 µm dimensions will become fragile and will be prone to breaking. Thus, the length of the probe also becomes a critical dimension. The center of the striatum, where dopamine is often measured in the rat brain, is located 4 mm below the surface of the brain. Thus the probes need to be at least 4 mm long with the array located close to the end of the tip. To avoid the increased stress on the sensor during fabrication and handling, the length of the shaft containing the IDA was kept to 1 mm at this point. In the final design, the length of the shaft will be increased to 4 mm or more and that of the broader part containing the connection lines will be decreased accordingly. The connection pads are designed so that the connectors currently in use are compatible with the sensors. Although longer shafts (1.98 mm long) have been fabricated, but with a different goal.[9] This leads us to anticipate that the process is feasible.

4.5 FABRICATION PROCEDURE

The coplanar IDA sensors were fabricated using a conventional photolithographic procedure. These devices are 1 in. in length and 0.25 in. wide. Up to 44 such devices can be fabricated on a single 5-in. diameter wafer. Electrical connection from the sensor to the potentiostat is made using an edge connector (solder contact, 20/40 position, 0.05 in. pitch) from Sullins Electronics Corp., CA. After being released from the substrate, the sensor will be 0.25 in. wide from the back end containing the connection pads and 670 µm or less from the tip. A brief procedure is listed below and a fabrication flow chart as well as the schematics of the steps followed are shown in Figure 4.3 and 4.4.

SiO_2 thermally grown served as an initial passivation layer between gold and the semiconductive silicon. The devices consist of two layers: gold attached to the silicon by Cr

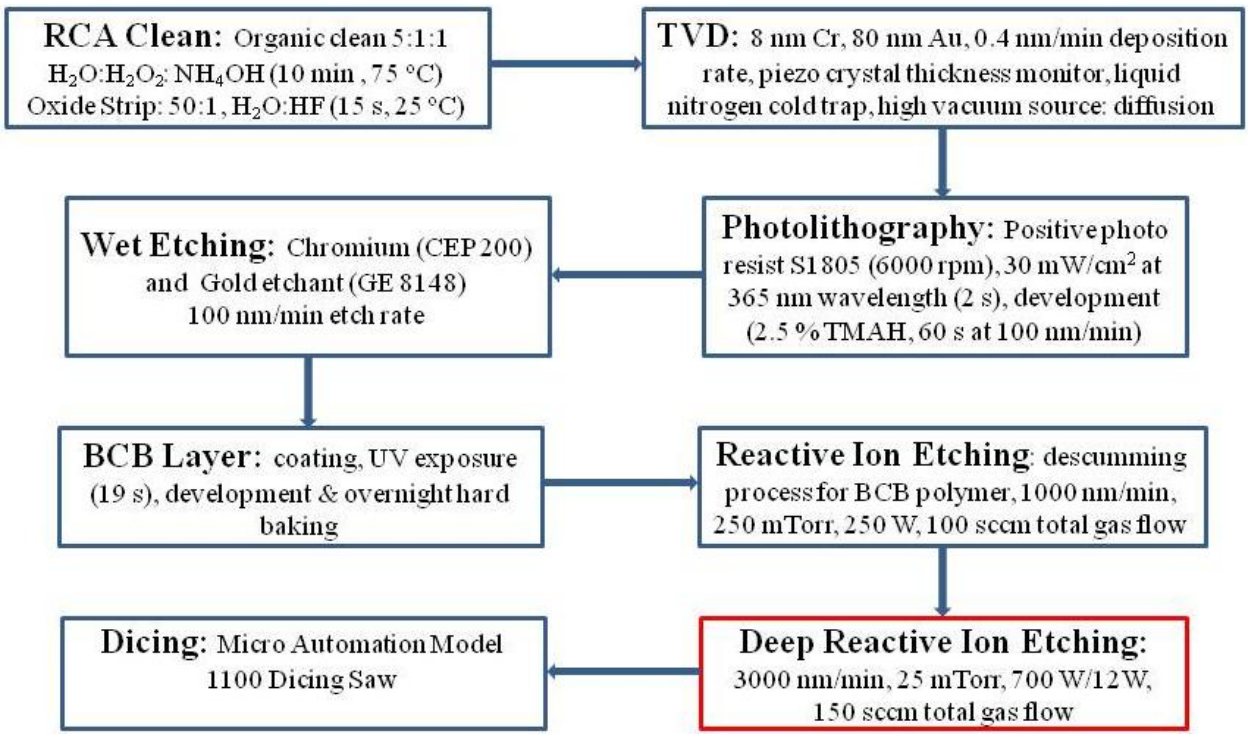

Figure 4.3. Flow chart of the fabrication procedures followed for the making of the sensors. The step shown in red box (DRIE) is not yet performed on the IDAs that have been characterized in this chapter. DRIE will be performed on the IDAs fabricated in future to release them from the bulk of the silicon substrate and tested for their durability and fragility.

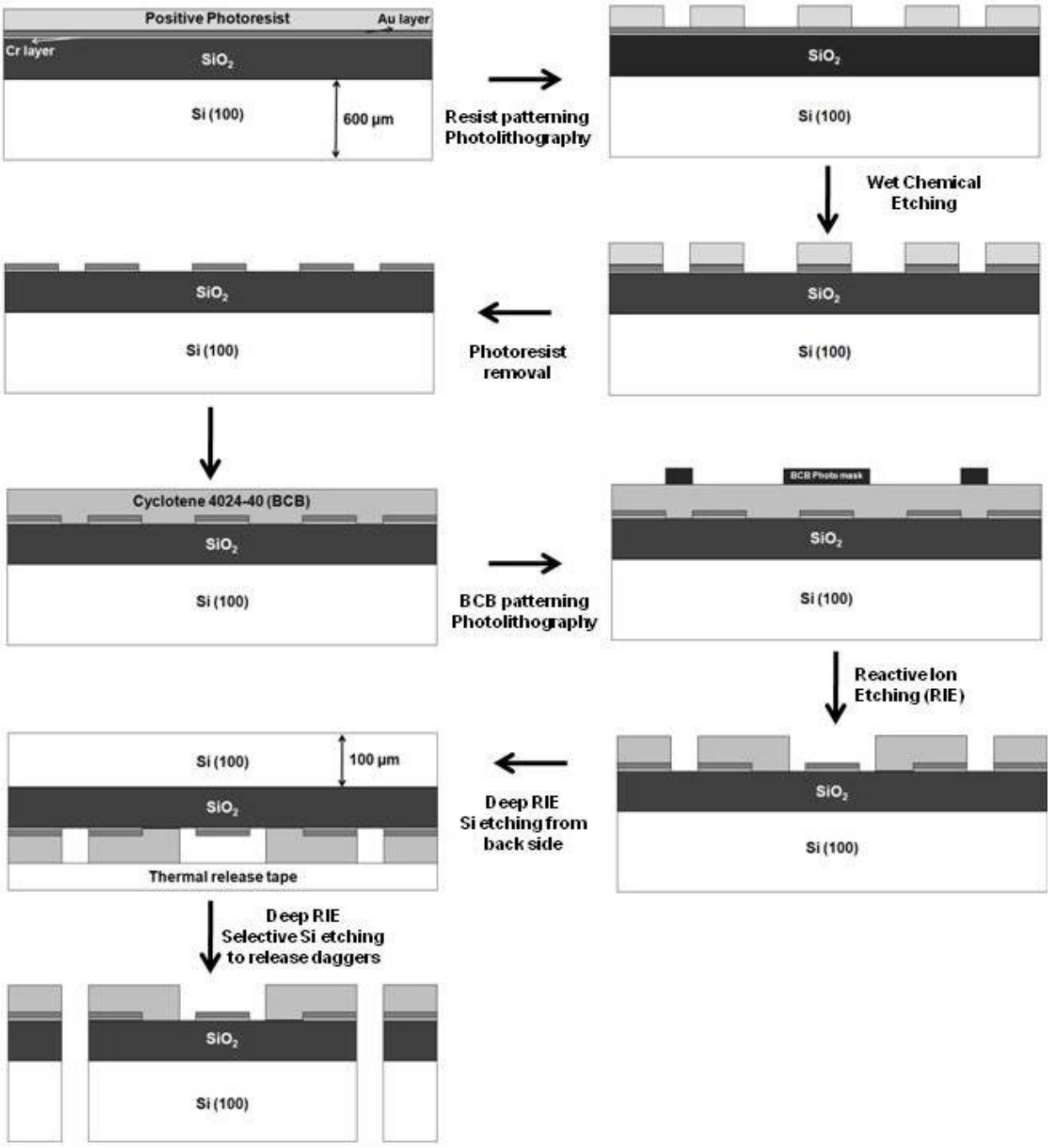

Figure 4.4. Schematics of the fabrication steps followed for the making of the sensors. The DRIE step is not yet performed on the IDAs that have been characterized in this chapter. DRIE will be incorporated in the fabrication of the IDAs in future to release them from the bulk of the silicon substrate and tested for their durability and fragility.

adhesion layer; insulating polymer layer that defines the active electrochemical area. These devices are constructed by sequentially depositing and patterning each layer, followed by reactive ion etching (RIE) to expose the array area.

Wafers were cleaned prior evaporation of metal layers to remove any contaminants that can cause defects during fabrication. One of the most commonly used procedures, known as RCA clean (named after the inventors RCA (Radio Corporation of America) Laboratories), was used. It is a wet clean process and uses a mixture of water, solvent, acids or bases depending on the type of the contaminant to be removed. To remove organics, metals and particles in the first step, SC1 (organic clean) is used. To remove the native oxide, oxide strip using HF is used. The organic clean was done using the 5:1:1 mixture of DI H_2O:NH_4OH:H_2O_2 for 10 minute at 75 °C. The oxide strip was done using the 5:1:1 mixture of DI H_2O:NH_4OH:H_2O_2 for 10 minute at 75 °C. The oxide strip was done using the 50:1 mixture of DI H_2O:HF for 15 s at room temperature. After each step, the wafers were rinsed immediately with copious amount of deionized water followed by spin-rinse-dry.

A gold bar and a chromium plated tungsten rod served as sources for thermal evaporation. Layer 1 forms the IDA and the contact pads to the electrodes contained in the IDA. Layer 1 (8 nm of Cr and 80 nm of Au) was deposited on SiO_2 deposited Si wafer (without breaking vacuum between the metals) with an Edwards 306 Auto thermal evaporator, fitted with a piezoelectric crystal thickness monitor. The wafer was spin-coated with photoresist (S1805) at 6000 rpm to form a uniform thickness of the film. The photoresist was patterned by exposure through a chrome mask for 2 s. The Au and Cr layers were then etched for 5 s each respectively by wet etch process. The completion of the etching process was verified through resistance

measurements between contact pads of the same Au layer with a multimeter. After rinsing with deionized water, the wafer was dried for 30 min at 125 ºC prior to coating with the polymer.

Layer 2 serves as the insulator to prevent the shorting of metal layers. The wafer was spin coated with the photosensitive polymer at 3000 rpm for a final thickness of 4.8 µm. The polymer film was exposed to a blanket of 350 nm UV light for 19 s through a second Cr mask using Karl Suss MA-150 mask aligner to cross-link the polymer, resulting in a continuous, defect-free insulator film. The layer was then selectively removed from certain parts of the IDA and the connecting lines for the contact pads using the BCB developer (DS 2100). A descumming procedure was then performed using reactive ion etching (mixture of O_2, 36 sccm and SF_6, 4 sccm at 300 mT and 300 W rf power applied for 1 min).

Individual sensors were cut into the individual rectangular chips (shown in figure 4.2) from the wafer by dicing them using a silicon blade. At this moment the sensors are joined to the bulk of the substrate. Once they are characterized, they will be released from the bulk of the silicon substrate to give them a probe like shape, as outlined in pink in figure 4.2. This will be done using deep reactive ion etching. The existing designs of the masks and the sensors have provisions for carrying out deep reactive ion etching. The sensors are also 600 µm thick. Their thickness needs to be reduced to 100 µm. This will be accomplished using reactive ion etching with controlled timing. Reactive ion etching will be performed on the back side of the wafers having a bare silicon surface. The thinning of the wafer containing multiple sensors will be performed before the individual sensors are released using deep reactive ion etching, to prevent their scattering inside the instrument. Once their thickness is reduced to 100 µm, a protocol for their handling will have to be established.

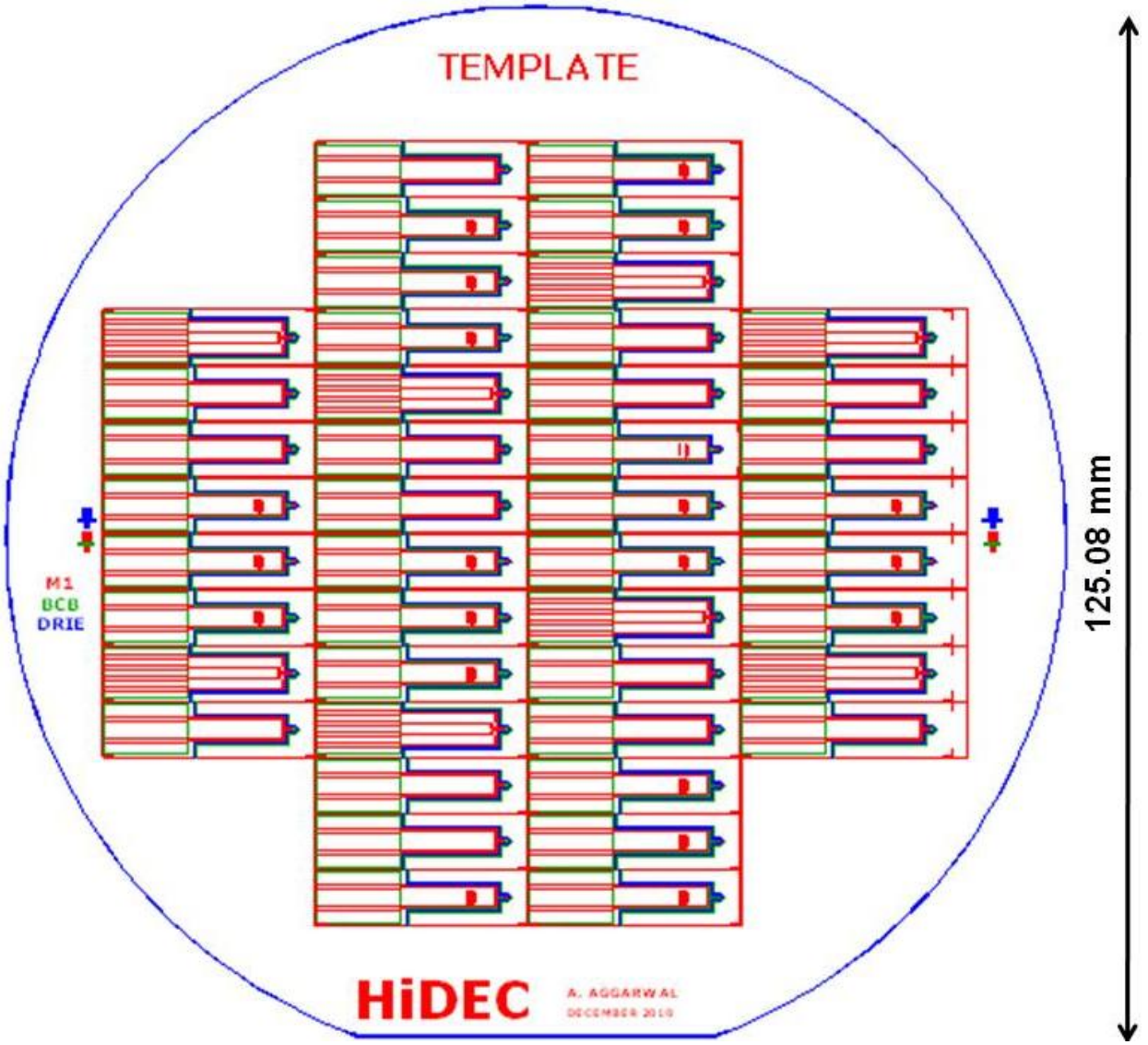

Figure 4.5. Overlay of the AutoCAD designs of different layers on the sensors. The bottom layer (shown in red) forms the gold features on the silicon wafer. The middle layer (shown in green) forms the BCB insulation layer over gold. The top layer (shown in blue) forms the sensor release boundary from the substrate. It will be used to define the area where deep reactive ion etching will be performed. Each sensor device is 1 in. long x 0.25 in. wide. The wafer contains a total of 44 such devices, with a minimum of 7 devices of each design.

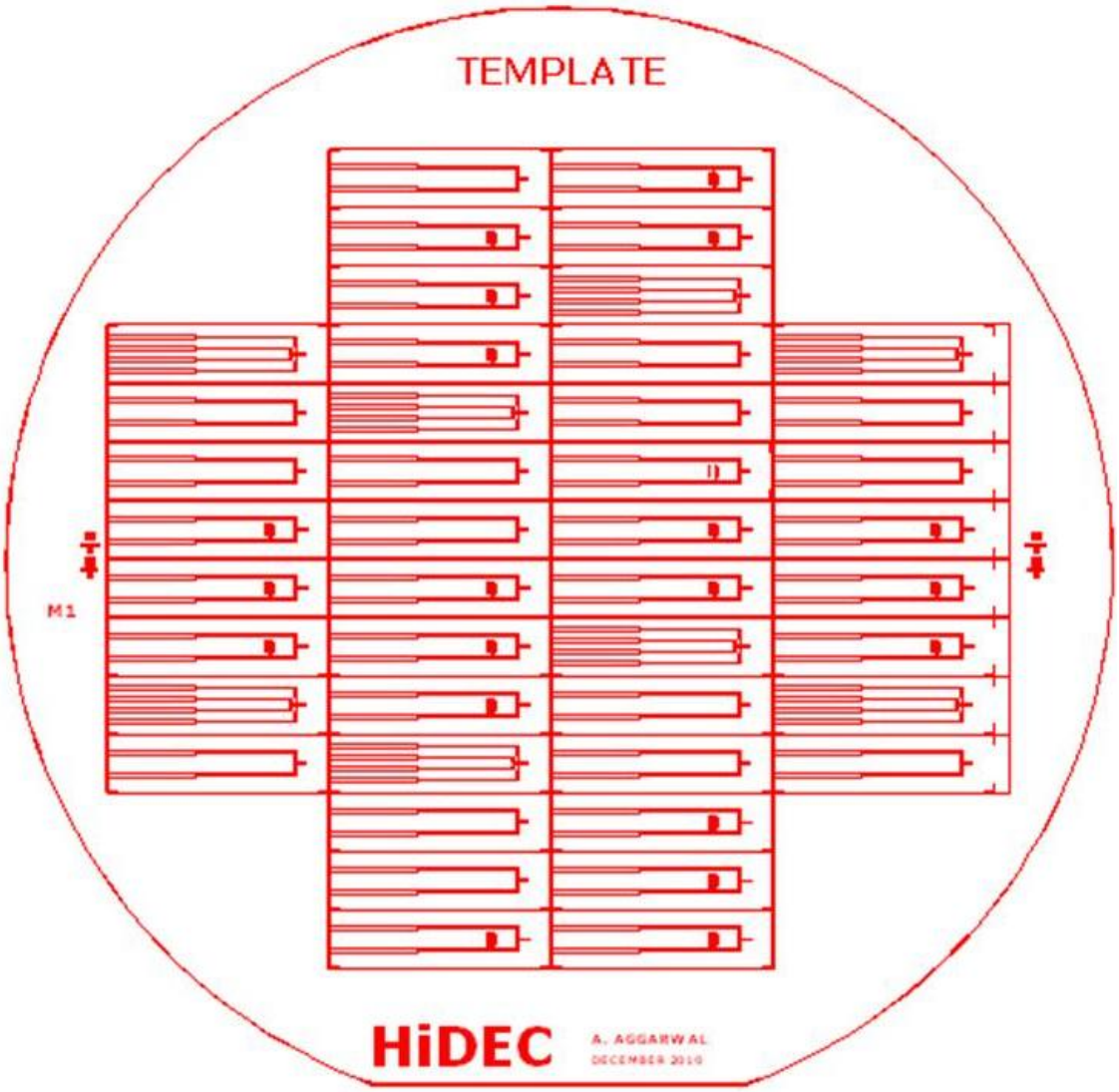

Figure 4. 6. AutoCAD design of the clear field mask forming the gold features on the silicon wafer.

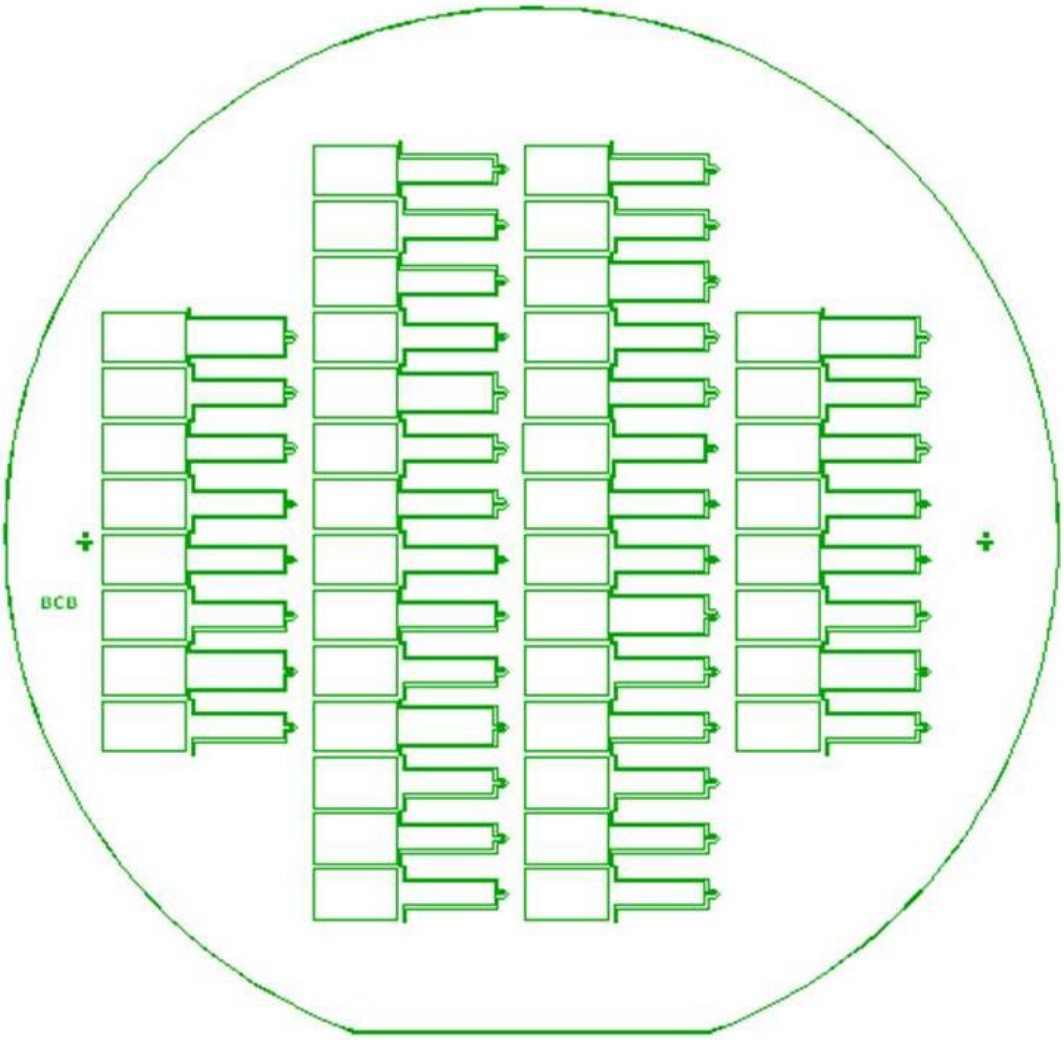

Figure 4. 7. AutoCAD design of the clear field mask forming the BCB features on the silicon wafer.

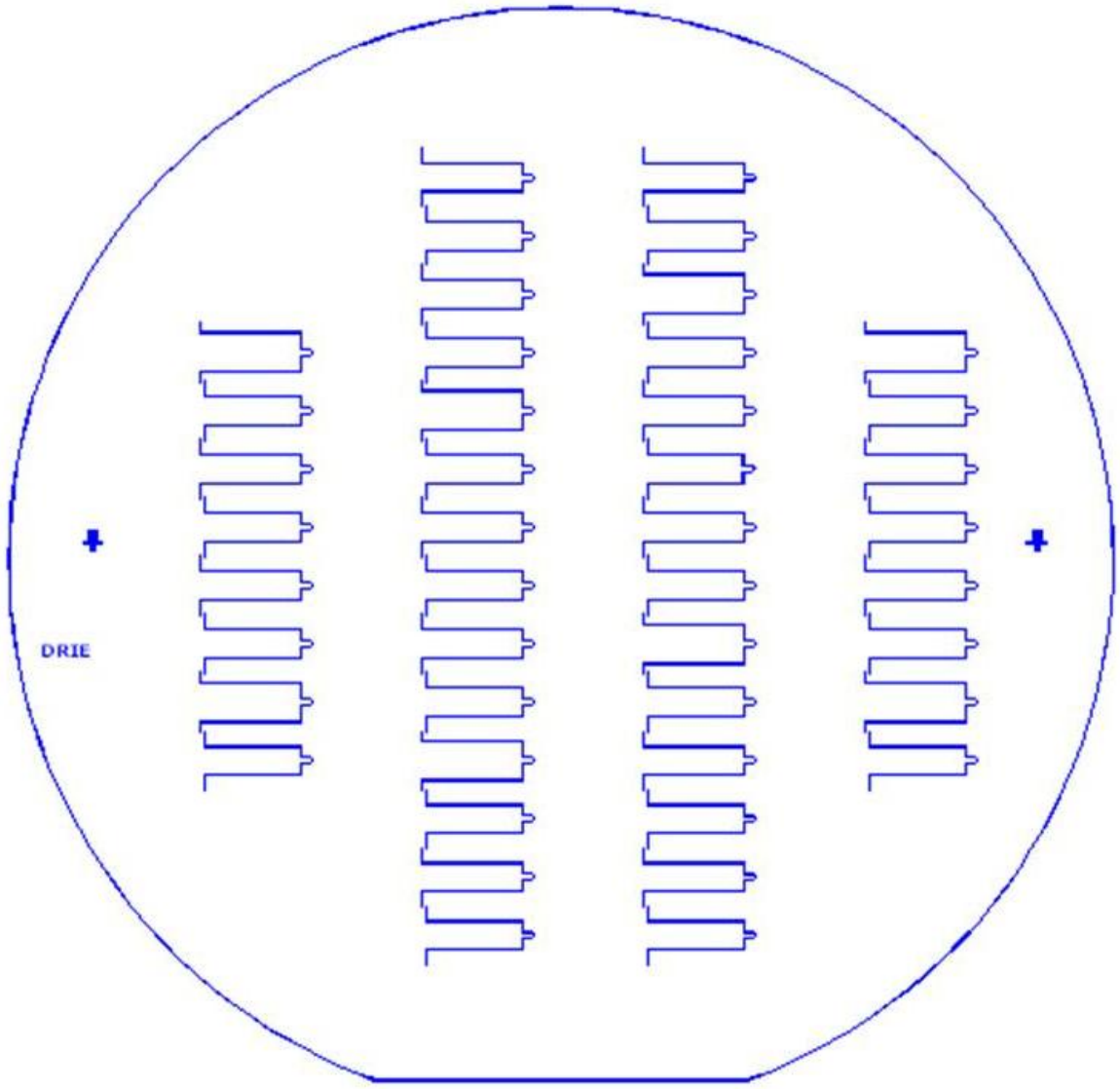

Figure 4. 8. AutoCAD design of the dark field mask defining the perimeter where DRIE is to be carried out.

4.5 RESULTS AND DISCUSSION

4.5.1. Characterization of IDAs. Pictures of the fabricated IDAs that were characterized are shown in Figure 4.9. Each IDA contains two sets of coplanar band electrodes comprising of a generator and a collector electrode, each with multiple microband elements. Microbands in the IDAs have an average width of 5.38 ± 0.47 μm and are separated by 2.42 ± 0.47 μm gaps. The combined width and gap on one side of microband is 7.8 ± 0.1 μm. The parallel microbands are 140 ± 0.1 μm long in the 260 μm x 260 μm IDA (Designs A and B) and 50 ± 0.1 μm long in the 260 μm x 100 μm IDA (Designs C, D, and E). Once released from the substrate, the width of the shaft containing 260 μm x 260 μm IDA will be 670 μm and for 260 μm x 100 μm IDA will be 580 μm. Due to different arrangements of electrodes in each design and different numbers of electroactive elements composing the generator and the collector, the area of generator and collector is different in each design. Table 4.1 lists the measured electroactive areas and total areas occupied (electroactive and spaces between) by the generator and the collector for different configurations.

Each set of interdigitated electrode was characterized by cyclic voltammetry in 5.0 mM $[Ru(NH_3)_6]^{3+}$ redox solution and 0.50 M KCl electrolyte at 0.10 V/s and 0.01 V/s scan rates. Figure 4.10 shows CV responses for each geometry at 0.10 V/s scan rate. The electrochemical response of the electrodes for each design showed high reproducibility from array to array (4.45% relative standard deviation, RSD, 15 IDAs, single wafer). These results suggest that the fabrication procedure is sufficiently precise for these dimensions.

4.5.2. Calibration curves. Of the five IDA designs constructed, calibration curves for Designs D and E were prepared. They have the required dimensions for future tissue insertion

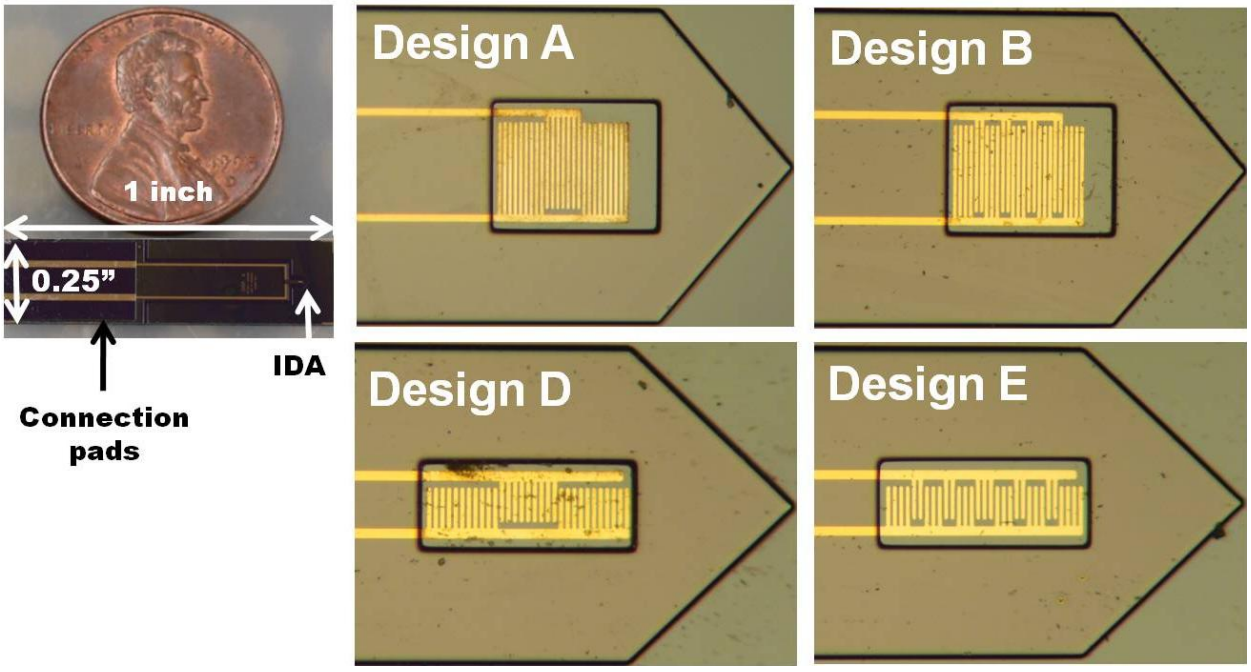

Figure 4.9. Pictures of the probe sensor and expanded views of IDA designs A through E. The probes have not been removed from the substrate at this stage. After releasing them using deep reactive ion etching, they will lose much of the bulk material around the shaft and the tip of the shaft will become pointed as shown by the black outline. The black outline is the BCB edge formed where it has been developed to expose the underlying substrate.

Table 4.1. List of the measured areas of the generator and the collector electrodes contained in different IDAs. G represents the generator electrode and C represents the collector electrode.

IDA Designs	Generator area / cm^2	Collector area / cm^2
A (260 µm x 260 µm outer G flanking central C)	1.63×10^{-4}	6.88×10^{-5}
B (260 µm x 260 µm mixed G – C pairs)	1.60×10^{-4}	8.29×10^{-5}
C (260 µm x 100 µm alternating G-C)	7.06×10^{-4}	6.70×10^{-5}
D (260 µm x 100 µm outer G flanking central C)	7.90×10^{-5}	4.65×10^{-5}
E (260 µm x 100 µm mixed G – C pairs)	7.42×10^{-5}	5.14×10^{-5}

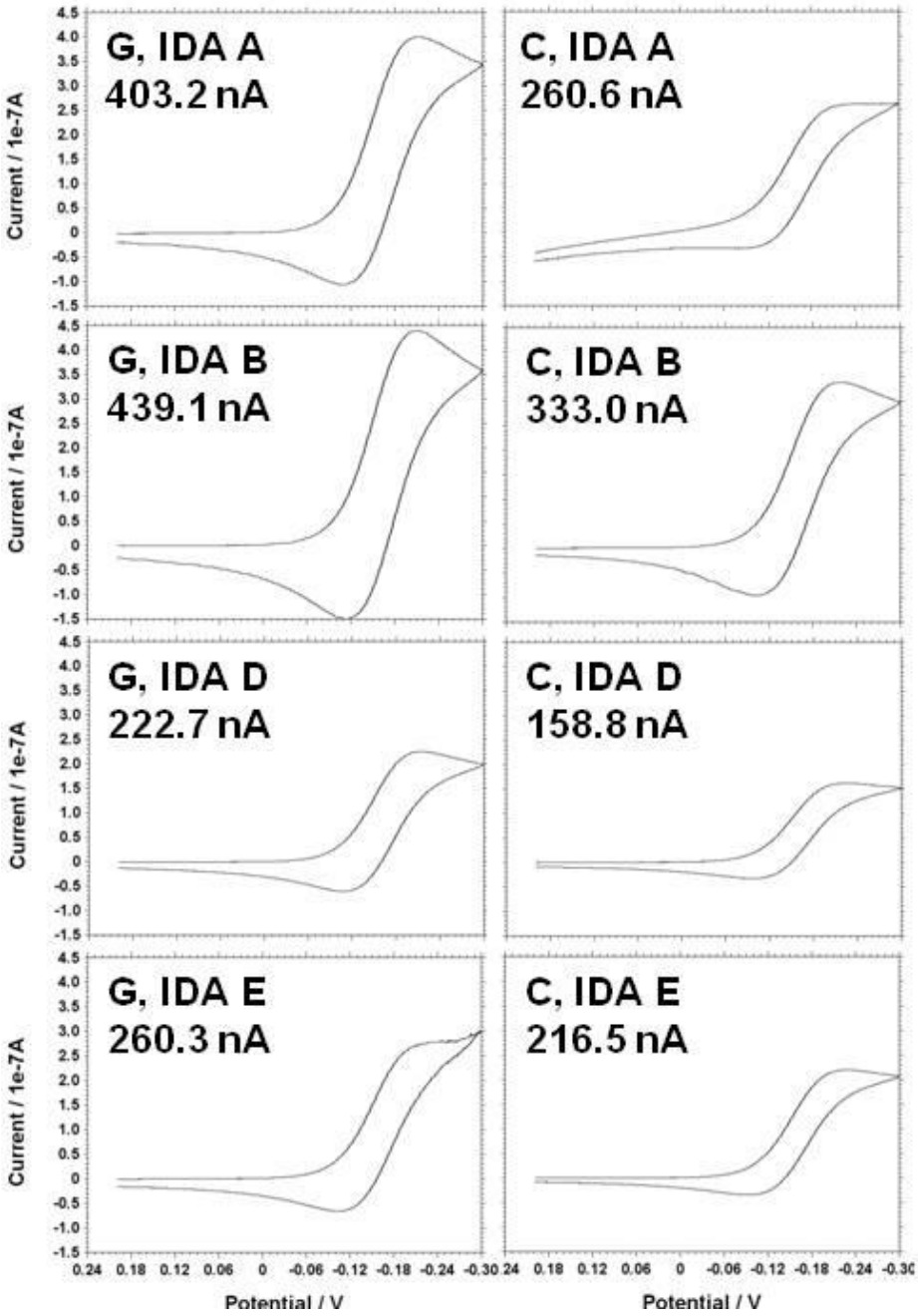

Figure 4.10. CV responses for generator and collector electrodes contained in IDA designs A, B, D and E obtained in 5 mM $[Ru(NH_3)_6]^{3+}$ and 0.5 M KCl at 0.10 V/s scan rate. G represents the generator and C represents the collector. The electrochemical current of the generator and collector electrode contained in each IDA is shown. At the given scan rate of 0.1 V/s, all the electrodes in each IDA produced a peak current. As stated earlier in the text, design C has not been characterized at this time.

experiments and the optimized electrode configuration for dopamine detection in presence of ascorbate. Figure 4.11 shows linear calibration curves for the two 260 µm x 100 µm IDAs (all having R^2 values of ≥99%) obtained in $[Ru(NH_3)_6]^{3+}$ at 0.01 V/s scan rate with and without redox cycling. The detection limits were calculated at a signal-to-noise ratio of three. The detection limits for the IDA design E (0.291 µM at the generator and 0.532 µM at the collector) show 30% improvement at the collector and 63% deterioration at the generator than those for the IDA design D (0.178 µM at the generator and 0.786 µM at the collector). We have seen in Chapters 2 and 3 that the same configuration of electrodes may not work as efficiently for dopamine as for the model compound. Therefore, at this point, the data is not sufficient to conclude which IDA design will provide better results with dopamine. Additional experiments are required to determine the optimal IDA for dopamine detection.

The current amplification at the generator (factor of 1.22 for design D and 1.47 for design E) caused by redox cycling is similar to the amplification (1.23) obtained for individually addressable MEA contained in 1" x 1" chips for the outer generator flanking the central 4 collector elements. The current enhancement due to redox cycling is not significant due to low concentration gradient because of the very small collector and due to big gap (4 µm) between the electrodes. The collection efficiencies of the collector (46.40% for design D and 58.03% for design E) are also similar to the collection efficiency (40.00%) obtained for individually addressable MEA contained in 1" x 1" chips for the outer generator flanking the central 4 collector elements.

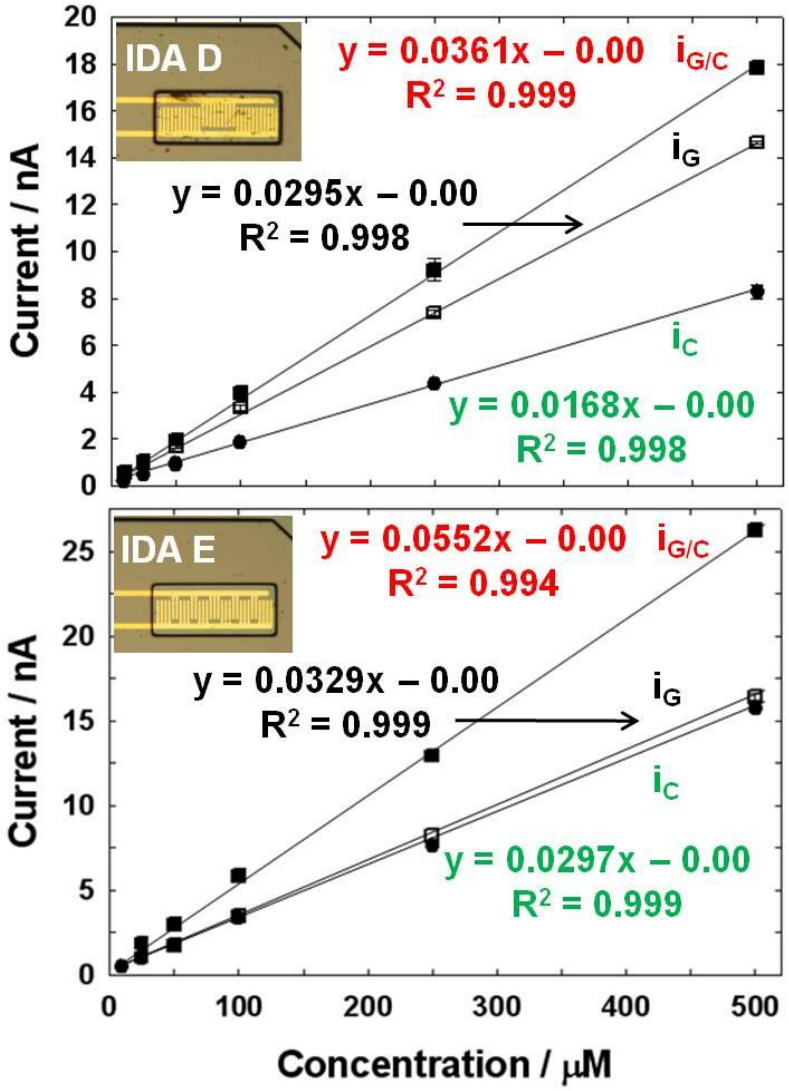

Figure 4.11. Calibration curves obtained from IDA design D and E in the presence and absence of redox cycling in varying concentrations of $[Ru(NH_3)_6]^{3+}$ at 0.01 V/s scan rate. Equations for the least squares best fit lines to the data are shown in the figure. Detection limits (determined from three times the standard deviation of the blank) are as follows: (a) design D: generator with collector off, 0.360 µM (open squares); generator with collector on, 0.178 µM (closed squares); collector, 0.786 µM (closed circles); and (b) design E: generator with collector off, 0.396 µM (open squares); generator with collector on, 0.291 µM (closed squares); collector, 0.532 µM (closed circles). i_G is CV current, $i_{G/C}$ is the generator current during redox cycling and i_C is the collector current.

4.6 DISCUSSION, CONCLUSIONS & FUTURE WORK

Semiconductor is the fastest growing industry in terms of attaining smaller device dimensions and lower cost. Advancements in semiconductor industry can be intertwined with redox cycling technology to detect smaller concentrations of biochemicals on sensors with ever decreasing sizes. This will also fulfill the goals of the neurological and medical industry to achieve more challenging detection limits. Smaller sizes of the sensors are desirable to decrease tissue damage, which will facilitate research and improve the scope and reliability of the diagnosis.

The IDAs have been fabricated and characterized with the model redox species, hexaammineruthenium (III). A precise fabrication procedure has been established for the small sensors as well as their electrochemical reproducibility from device to device has been shown. Of the five designs fabricated, two (D and E) containing the optimized electrode dimensions and configurations were studied in more detail. Their current detection limits with the model compound are ~ 500 nM. Future studies on these IDAs include characterizing them and obtaining calibration curves for dopamine in the presence and absence of interferences such as ascorbate and DOPAC. Detection limits of dopamine under different conditions still need to be determined on the IDAs.

We predict that these IDA sensors should be able to detect down to 5 μM dopamine in the presence of 100 times excess ascorbate, as explained below. The area of the generator in the IDAs (design D and E) is smaller by a factor of 15 and of the collector is smaller by a factor of 7 from the areas of the generator and collector of the electrode arrangement in a band MEA (outer 14 generator and central 4 collector arrangement, chapter 3) evaluated for detection of dopamine

in presence of 100 µM ascorbate, giving a detection limit of 452 nM at the collector. With a seven-fold decrease in the electrochemical area of the collector electrode in the IDAs compared to that in the band MEA, the level of the background noise (standard deviation (S) of the blank signal) at the collector during redox cycling also scaled down by a factor of six (S = 29.0 pA for the collector at band MEA and 4.4 pA at the IDA). Therefore, the IDAs with the present dimensions should detection at least 7 fold dopamine to that of the LOD obtained at band MEA in presence of 100 µM ascorbate, which would be 3.2 µM.

In order to optimize the final design of the sensor and be able to use it for brain insertion studies, it needs to detect at least 1 µM dopamine in presence of 100 times excess ascorbate. It is also shown that the collection efficiency of the collector increases exponentially with a decrease in the generator-collector gap. Before proceeding further, it is possible to determine theoretically the required changes to be made in the final sensor design to achieve the target LOD of dopamine.

According to the Fick's first law, the flux of a redox species is directly proportional to its concentration gradient, and therefore also to the gap between the electrodes (which is the distance traveled),

$$-J_o(x,t) = D_o \frac{\partial C_o(x,t)}{\partial x} = \frac{i}{nFA} \qquad (1)$$

where J is the flux of the species, D_o is the diffusion coefficient, C_o is the concentration, x is the distance traveled by the redox species, n is the number of electrons transferred, F is the faraday constant, and A is the area of the electrode. Also,

$$m = \frac{\partial i}{\partial C_o} = \frac{3S}{LOD} \qquad (2)$$

where m is the slope of the calibration curve. Equations 1 and 2 can now be rearranged to estimate the gap between the electrodes needed to obtain the target detection limit.

$$\partial x = LOD\frac{DnFA}{3S} \qquad (3)$$

Note that the above analysis is only an approximation. It is based on a geometry where collector and generator are directly opposite to each other and of equal areas, as in a sandwich configuration. This is why Fick's Law was used, which represents diffusive-flux for one dimension. Therefore, the analysis underestimates what should be expected experimentally, because it does not account for additional improvements in signal from enhanced collection efficiency of co-planar electrodes that occurs when the gap is diminished. (In a sandwich-arrangement, collection efficiency does not change with gap.)

Assuming the same level of the noise (S) as for the IDAs with 4-μm spacing between the generator and collector electrodes, the LOD should vary linearly with the gap between the electrodes. Thus, in order to improve the detection limits of the IDAs from 5 μM to 1 μM in dopamine in a mixture with 100 μM ascorbate, the gap between the electrodes should be decreased from 4 μm to 0.8 μm; to improve the detection limits to 0.5 μM, the gap should be decreased to 0.4 μm.

The numbers provided above do not take into account other factors such as the additional improvement in amplification possible when the gap is diminished between co-planar electrodes, and the decrease in the amount of the reaction between ascorbate and dopamine-quinone. The rate of the reaction depends on the available concentrations of the two species. Capture efficiency of dopamine quinone at the collector before being reduced by ascorbate should also improve because less time is needed to travel across smaller gaps. Thus, less generator area is

needed to deplete ascorbate. More collector area in an interdigitated arrangement would then be possible, which as we saw in Chapter 2, can greatly improve amplification and detection limits.

4.7 ACKNOWLEDGEMENTS

Funding has been provided in part by the National Science Foundation (CHE-0719097) and the Arkansas Biosciences Institute, the major research component of the Arkansas Tobacco Settlement Proceeds Act of 2000. We thank Errol Porter and Mike Glover for advice on microfabrication. The use of the High Density Electronics Center microfabrication facilities is also acknowledged. We express our appreciation to Professor Adrian Michael at the University of Pittsburgh for insightful discussions about applications and offering to test our probes in vivo.

4.8 REFERENCES

(1) Kempe, V. *Inertial MEMS: Principles and Practice*; Cambridge University Press, 2011.

(2) Plummer, J. D.; Deal, M. D.; Griffin, P. B. *Silicon VLSI technology : fundamentals, practice, and modeling*; Beijing : Publishing House of Electronics Industry, 2003, 2003.

(3) Ayazi, F.; Najafi, K. *Journal of Microelectromechanical Systems* **2000**, *9*, 288-294.

(4) Ayon, A. A.; Zhang, X.; Khanna, R. *Sensors and Actuators a-Physical* **2001**, *91*, 381-385.

(5) Chang, C. L.; Wang, Y. F.; Kanamori, Y.; Shih, J. J.; Kawai, Y.; Lee, C. K.; Wu, K. C.; Esashi, M. *Journal of Micromechanics and Microengineering* **2005**, *15*, 580-585.

(6) McAuley, S. A.; Ashraf, H.; Atabo, L.; Chambers, A.; Hall, S.; Hopkins, J.; Nicholls, G. *Journal of Physics D-Applied Physics* **2001**, *34*, 2769-2774.

(7) Burmeister, J. J.; Moxon, K.; Gerhardt, G. A. *Analytical Chemistry* **2000**, *72*, 187-192.

(8) Burmeister, J. J.; Pomerleau, F.; Palmer, M.; Day, B. K.; Huettl, P.; Gerhardt, G. A. *Journal of Neuroscience Methods* **2002**, *119*, 163-171.

(9) Sreenivas, G.; Ang, S. S.; Fritsch, I.; Brown, W. D.; Gerhardt, G. A.; Woodward, D. J. *Analytical Chemistry* **1996**, *68*, 1858-1864.

(10) Zachek, M. K.; Park, J.; Takmakov, P.; Wightman, R. M.; McCarty, G. S. *Analyst* **2010**, *135*, 1556-1563.

(11) Henry, C. S.; Fritsch, I. *Journal of the Electrochemical Society* **1999**, *146*, 3367-3373.

(12) Henry, C. S.; Fritsch, I. *Analytical Chemistry* **1999**, *71*, 550-556.

(13) Burmeister, J. J.; Pomerleau, F.; Huettl, P.; Gash, C. R.; Wemer, C. E.; Bruno, J. P.; Gerhardt, G. A. *Biosensors & Bioelectronics* **2008**, *23*, 1382-1389.

(14) Liu, X.; Li, Y. L.; Hou, F. *Journal of the American Ceramic Society* **2009**, *92*, 49-53.

(15) Burmeister, J. J.; Gerhardt, G. A. *Analytical Chemistry* **2001**, *73*, 1037-1042.

(16) Ranganathan, S.; McCreery, R.; Majji, S. M.; Madou, M. *Journal of the Electrochemical Society* **2000**, *147*, 277-282.

(17) Zachek, M. K.; Takmakov, P.; Moody, B.; Wightman, R. M.; McCarty, G. S. *Analytical Chemistry* **2009**, *81*, 6258-6265.

(18) Kostecki, R.; Song, X.; Kinoshita, K. *Electrochemical and Solid State Letters* **1999**, *2*, 465-467.

(19) Ranganathan, S.; McCreery, R. L. *Analytical Chemistry* **2001**, *73*, 893-900.

(20) Gao, Z. Q.; Ivaska, A. *Analytica Chimica Acta* **1993**, *284*, 393-404.

(21) Mo, J. W.; Ogorevc, B. *Analytical Chemistry* **2001**, *73*, 1196-1202.

(22) Pihel, K.; Walker, Q. D.; Wightman, R. M. *Analytical Chemistry* **1996**, *68*, 2084-2089.

(23) Huang, X. J.; O'Mahony, A. M.; Compton, R. G. *Small* **2009**, *5*, 776-788.

(24) Michael, A. C.; Borland, L. M.; Mitala, J. J.; Willoughby, B. M.; Motzko, C. M. *Journal of Neurochemistry* **2005**, *94*, 1202-1211.

(25) Borland, L. M.; Shi, G. Y.; Yang, H.; Michael, A. C. *Journal of Neuroscience Methods* **2005**, *146*, 149-158.

(26) Michael, A. C.; Borland, L. M. *Electrochemical methods for neuroscience* Boca Raton : CRC Press/Taylor & Francis, 2007.

(27) Kulagina, N. V.; Zigmond, M. J.; Michael, A. C. *Neuroscience* **2001**, *102*, 121-128.

(28) Borland, L. M.; Michael, A. C. *Journal of Neurochemistry* **2004**, *91*, 220-229.

(29) Borland, L. M.; Michael, A. C. *Electrochemical methods for neuroscience*; Boca Raton : CRC Press/Taylor & Francis, 2007.

(30) Michael, A. C.

(31) Takmakov, P.; Zachek, M. K.; Keithley, R. B.; Bucher, E. S.; McCarty, G. S.; Wightman, R. M. *Analytical Chemistry* **2010**, *82*, 9892-9900.

5. SCANNING ELECTROCHEMICAL MICROSCOPY

5.1 ABSTRACT & SIGNIFICANCE

Scanning electrochemical microscopy (SECM) allows visualization of the local electrochemistry on the surface of a substrate. It uses very small microelectrode tips (SECM tips, 10 nm – 10 µm) that scan the surface of the substrate to study its electrochemical activity. The SECM electrode tips are usually made in house by laboratories having shapes and sizes specific to their needs. Fritsch lab has acquired the SECM instrument that has been specifically modified for studying the local electrochemistry of dopamine and ascorbate interaction in their mixture during redox cycling on a sensor. SECM electrode tips as well as carbon fiber electrodes were fabricated in order to carry out the future SECM experiments. This chapter discusses the fabrication procedure and characterization of the SECM electrode tips. The experiments to be performed using SECM for the optimization of generator and collector electrode gap to obtain better detection limits for dopamine using redox cycling, determine the possible pattern in electrode fouling, and study the local electrochemistry between the interaction of dopamine with ascorbate during redox cycling are discussed in detail in chapter 6 as part of the future work. This chapter presents the essential preliminary work that has been accomplished for performing the mentioned experiments.

5.2 INTRODUCTION

SECM is an electrochemical imaging technique that allows mapping of chemical species generated or depleted at surfaces immersed in electrolyte. Since its invention in 1980's, SECM has become a powerful tool for studying processes at surfaces and biological samples.[1-5] When operated in constant distance control mode,[2] it provides submicron spatial resolution. Constant-distance or shear force positioning mode allows positioning of needle-type electrode tips (e.g. micron and sub-micron Pt-, Au- and carbon),[3, 4] in close proximity (< 200 nm) of surfaces, allowing the tip to follow the surface features without running into them. With SECM, voltage can be controlled and currents can be monitored at the tip or at the substrate that the tip scans over, or both. It has been used in past to monitor the electroactive and electroinactive regions of materials, as well as cellular activity of living biological cells grown on solid support.[6, 7] It can also provide tunable placement of microelectrode tip near the chip-based electrodes of sensor devices designed for redox-cycling detection of dopamine. This mode will allow the study of optimization of gap between generators and collectors. The SECM instrument purchased by the Fritsch laboratory has been specifically modified for these experiments.

State of the art to fabricate the SECM tips[3] depends on each laboratory based on the experimental requirements and conditions. At present, laboratories device their own mechanism to make the SECM tips. The diameter, length and shape of the tip as well as their flexibility are some of the important parameters that need to be controlled during their construction. Change in these parameters can affect the results obtained. State of the art procedure for their construction is irreproducible. It is difficult to control all the parameters. Their shape and diameter, however,

can be controlled to the best of the present abilities by carefully selecting the manufacturing conditions and polishing parameters.

Since the substrate for electrochemical redox cycling studies contains the noble metal gold as the conductive material, it would be in the best interest to use SECM tips containing similar metal as their active electrochemical surface. It is extremely difficult to pull gold wires into microdisk electrodes by laser pulling or by gravitational pull mechanism. Few laboratories, including Dr. Fritsch's group, who attempted to produce gold microdisk electrodes were unsuccessful. Platinum, on the other hand, provides the best alternative to gold electrodes. It is easy to work with, provides reproducible microdisk electrode tips with diameters in the range of 100 nm to 25 μm. Platinum microdisk electrode and carbon fiber electrode tips have been fabricated using the pulling approach and characterized using a model compound. Their fabrication procedure is described below and their characterized data is shown. Characterization experiments were performed to demonstrate the capability of the SECM instrument in different operating modes.

Dopamine is well studied on carbon fiber electrodes. Their surface chemistry aids in adsorption of dopamine at oxidizing potentials, providing an increase in the signal. They were fabricated as an alternative to platinum electrode tips, if required. The procedure for their construction is similar to that for platinum electrode tips with minor modifications in the heating and pulling programs. PAN based T 650 carbon fibers (made by pyrolysis of polyacrylonitrile) were used as the conductive material. Availability of these electrodes in the lab will serve as a handy tool for carrying out fast scan cyclic voltammetry experiments as well as comparison of results.

5.3 EXPERIMENT

5.3.1. Chemicals and Materials. Hexaammineruthenium (III) chloride (Alfa Aesar, MA, USA) and potassium chloride (EMD Chemical Inc., Darmstatd, Germany), both ACS grade, were used as received. Water, ACS reagent grade (≥ 18 MΩ-cm), was obtained from Ricca Chemical Co. (Arlington, TX). 25 µm diameter Pt wire (99.99%, annealed) was obtained from Goodfellow Cambridge Ltd. and carbon fibers (chopped, 8 µm diameter x 76.2 mm length, 94% were obtained from Alfa Aesar (stock # 43055). Quartz capillaries (1.2 mm o.d. x 0.60 mm i.n. x 0.75 cm length, catalog # Q120-60-7.5) and borosilicate capillaries (1.2 mm o.d. x 0.69 mm i.d. x 10 cm length, item # B120-69-10) were both obtained from Sutter Instrument company. Single component silver epoxy (EPO-TEK® H35-175MP) was obtained from Epoxy Technology, Inc., Billerica, MA. MicroCut® Discs (PSA backed, 8" (203 mm) diameter, 1200 grit, P2500, Buehler, Deutschland) were used as polishing pads for the polishing of microdisk electrodes. The SECM instrument (SECM 004, Sensolytics GmbH, Bochum, Germany) contains PalmSens handheld tri-potentiostat, 7280 DSP lock in amplifier, XYZ nano-positioning system (P-611.3S Nanocube), and piezoelectric transducer (PZT P-611.3S).

5.3.2. Electrochemical characterization of tips. All electrochemical experiments were carried out in triplicates with a fresh solution each time to avoid carryover from the previous electrochemistry on the tripotentiostat. SECM tips were characterized with 5 mM $[Ru(NH_3)_6]^{3+}$ in 0.1 M KCl using cyclic voltammetry at 0.10 V/s scan rate. Potential was applied versus Ag/AgCl (saturated KCl) reference electrode.

To reveal the quality of the seal and features of electrode shape and structure, characterization of the electrodes by cyclic voltammetry in KCl electrolyte solution with and

without the model redox species hexaammineruthenium (III) chloride was performed. SEM was used to provide actual dimensions and micrographs of the shapes of electrodes.

5.4 CONSTRUCTION OF MICRODISK ELECTRODE TIPS

5.4.1 Platinum electrode tips. A laser puller (P2000, Sutter Inst. Co., Novato, CA) is used for pulling the metal wire – quartz capillary assembly. Platinum wire, 1 cm long, was inserted manually in the center of a 10 cm long quartz capillary. Capillary was inserted into the center of the laser heating chamber such that the laser beam would be focused on the center of platinum wire. Two ends of the capillary were connected to a vacuum pump via silicon tubing and a Y connector to evacuate the capillary prior and during heating as well as pulling to obtain proper glass seal around the metal wire and avoid any air bubbles. During the heating process, puller slays were fixed using an in house designed clamp.

The construction was done in two steps: uniform cylindrical sealing of the quartz capillary around the platinum wire followed by pulling of the capillary – platinum wire assembly into two halves, one having a long flexible end (which was used to make the electrode), and the other, a short-tapered end, which was discarded. The focus was on preparing thin ($\leq$ 1 μm tip diameter), long ($\geq$ 1 cm) and flexible tips. The parameters were optimized for obtaining the tips having desired shape. The following parameters were used for sealing of the quartz around the metal wire:

Heat: 770, Filament: 5, Velocity: 100, Delay: 120, Pull: 1

for 8 minutes in a series of 20 seconds heating time followed by 40 seconds cooling time. The clamp was then removed immediately and a second program with hard pull was applied:

Heat: 600, Filament: 2, Velocity: 130, Delay: 150, Pull: 220

This resulted in formation of two platinum electrode tips having long flexible and tapered ends. Electrical contact was made between a copper wire and platinum wire inside the pulled capillary from the back end of the capillary using a single component conductive silver epoxy. The epoxy was allowed to cure for 2 hours at 180ºC. A polishing machine was developed in house to provide suitable polishing of the fabricated electrodes while maintaining their long, thin and flexible shafts. A computer hard disk was used as the polishing disk. A polishing pad was glued to the surface of the hard disk. To polish the electrode surface, both the polishing disk and the electrode were rotated in opposite directions at 5000 rpm, while slowly bringing the electrode in contact with the rotating polishing disk simultaneously, using a micro-positioning system. SEM pictures of the fabricated platinum electrode tips are shown in Figure 5.1.

5.4.2 Carbon fiber electrodes. A single carbon fiber (heated at 400°C for 7 hours to remove seizing compounds) was inserted into a borosilicate type micro capillary along the entire length of the capillary. The capillary was then laser pulled by the application of parameters for the desired tip length, shape and seal using micropipette laser puller.

Conductive contact was made between the carbon fiber and copper wire (0.5 mm diameter) from the back end of the capillary using conductive carbon adhesive (product # 12664, EMS, PA). The back end of the capillary was sealed using PDMS or SYLGUARD. To ensure complete seal between glass and carbon fiber, the electrode tip was epoxied using Shell Epon Resin 828 and MPDA hardener (Miller Stephenson Chemical Co., Inc., CT). SEM images of the fabricated carbon fiber electrodes are shown in Figure 5.2.

5.4.3 Polishing of the electrode tips. The importance of polishing specially for the nano- and microdisk electrodes cannot be stressed enough. The surface of the electrode tip needs to be flat and smooth, with absence of any cracks and minimal surface roughness. This ensures

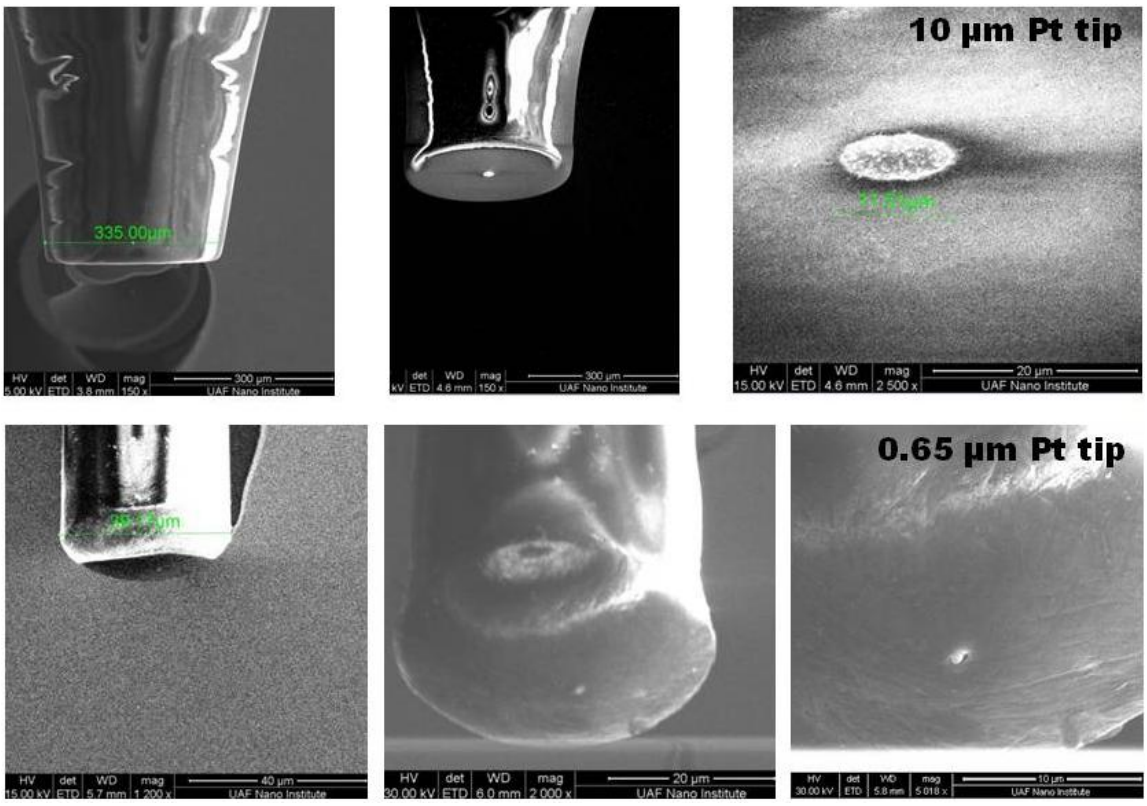

Figure 5.1. SEM images of the fabricated and polished platinum microdisk electrode tips of 10 µm and of 0.65 µm diameter are shown.

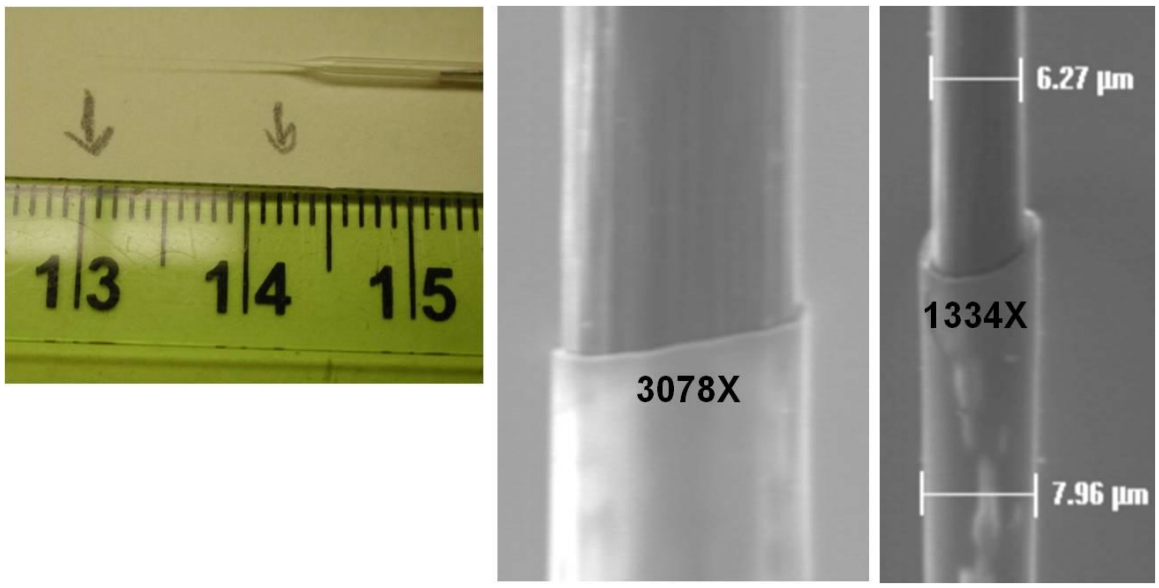

Figure 5.2. SEM images of the fabricated carbon fiber microdisk electrode tips of 6.27 µm diameter are shown.

reproducible electroactive area of the tips, which is important to maintain because the faraday current is proportional to the active area of the electrode. To obtain reproducible electroactive area of tips, they require polishing before and after their use each time. This reproducibility is observed in the background charging current which does not change from electrode to electrode. Diamond MicroCut® discs was used for the polishing of electrodes. The electrode is soaked in isopropanol for 30 minutes prior to use to remove organic or other insulating residue from the electrode surface.

5.5 RESULTS AND DISCUSSION

The desire to obtain extremely smooth surface and the inability to control the polishing time result in varying electrochemical area of these electrodes upon each round of polishing. Hence their active surface area has to be determined electrochemically prior their use each time.

The characterization also determines their electrochemical properties. Any exposed electroactive surface area at cracks in the glass insulating material increases the background charging current. An easy way to check for a good seal is to obtain log-log plot of capacitance normalized against the nominal electrode area as a function of scan rate. A robust seal would yield a slope of zero because capacitance is independence of scan rate; a negative slope suggests imperfect seal. At faster scan rates when higher currents are expected, the cracks impart an uncompensated resistance that provides a higher iR_u (potential) drop. Therefore, the contribution of the additional electroactive area of the electrodes to charging current is small. At slow scan rates, when i (and therefore iR_u) is small, charging current from electroactive area within the cracks plays a larger role, increasing the net capacitance.

At present the electrode tips are characterized in the model compound 5 mM $[Ru(NH_3)_6]^{3+}$ redox solution in 0.5 M KCl as the electrolyte and Ag/AgCl (saturated KCl) reference electrode at 0.10 V/s scan rate. Assuming a disk shape for the micro- and submicrometer size electrodes, a diffusion limited steady state current is expected due to hemispherical diffusion. The active surface area of the electrodes is then determined from the steady state current obtained using the equation 1.

$$i = 4nFDCr \qquad 1$$

It is important for SECM tips to exhibit steady state currents with a perfect plateau region. Using the procedure described above, well defined steady state cyclic voltammograms (shown in Figure 5.3) are obtained for electrode tips within the radius range of 100 nm to 2 µm. Figure 5.4 shows that the sigmoidal shape of the cyclic voltammograms as well as their current magnitude is independent of the scan rate.

5.6 CONCLUSIONS

Suitable electrodes for use as SECM tips are fabricated. Their characterization tells that they have good seal and a perfectly microdisk shape. Using these electrode tips and the sensor arrays as substrates, not only can SECM diagnose electrode fouling, but can also study the location and functionality of coatings.

5.7 ACKNOWLEDGMENTS

We appreciate the time and support from Dr. Wolfgang Schuhmann at the Ruhr-Universität, Bochum, Germany to provide valuable input on the use of SECM for our work. We thank Dr. Thomas Erichsen for fixing the SECM instrument. The time invested by Jerry Homesley in an attempt to fix the problems with the SECM instrument is greatly appreciated.

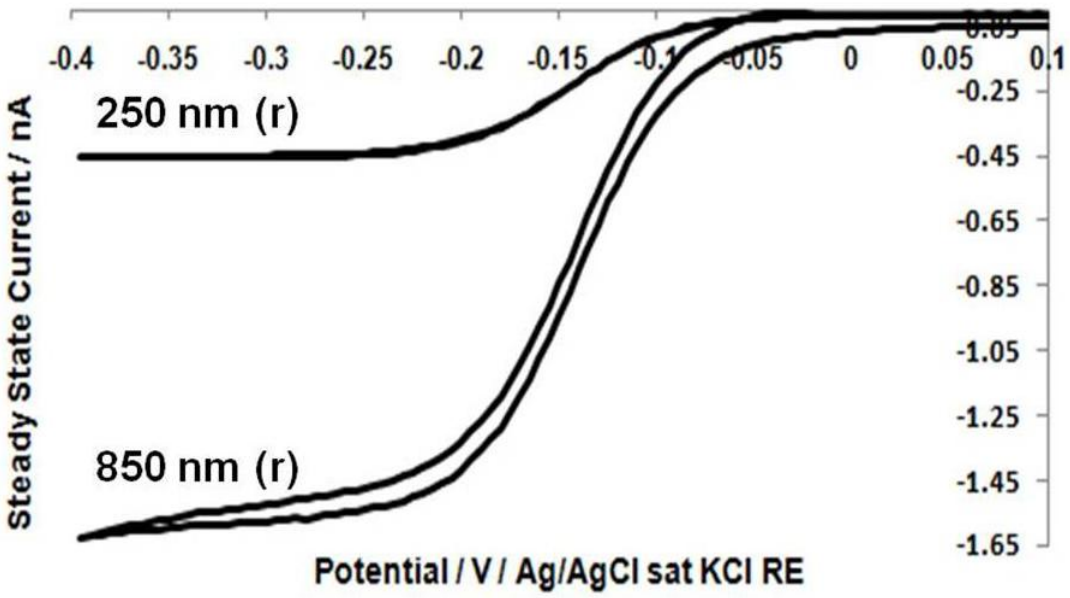

Figure 5.3. Overlay of cyclic voltammgrams of 850 nm and 250 nm radii microdisk platinum electrode tips obtained in 5 mM $[Ru(NH_3)_6]^{3+}$ and 0.5 M KCl at 0.10 V/s scan rate, exhibiting well defined steady state current.

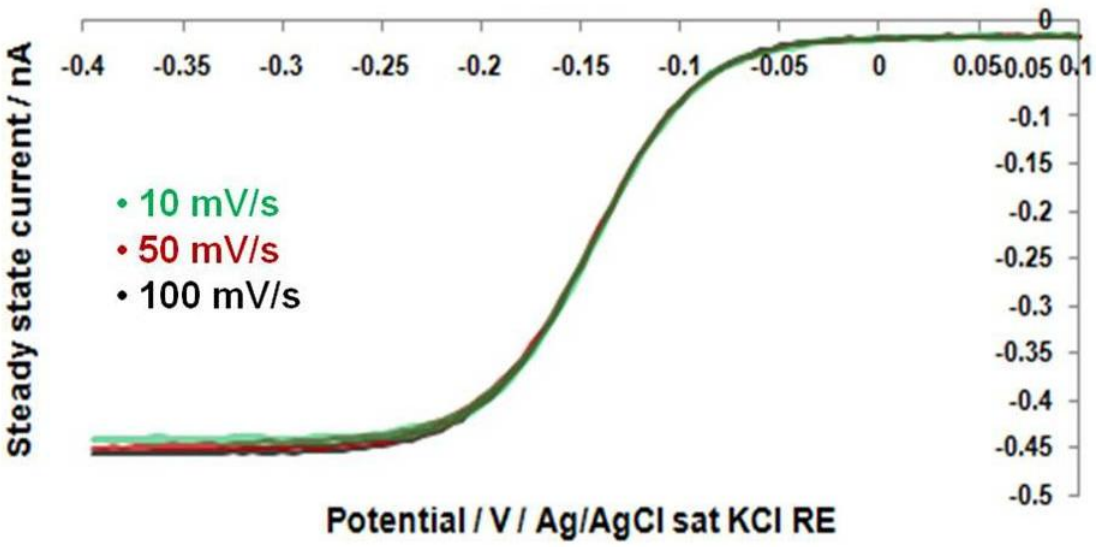

Figure 5.4. Overlay of cyclic voltmmogram (CV) of 250 nm radius microdisk platinum electrode tip in 5 mM $[Ru(NH_3)_6]^{3+}$ and 0.5 M KCl at scan rates: 0.10, 0.05 and 0.01 V/s. No change in the shape of the CV or in the magnitude of the current is observed with scan rate.

We thank Michaela Nebel for providing the training to work with SECM, as well as help in the understanding of the technique.

5.8 REFERENCES

(1) Barker, A. L.; Gonsalves, M.; Macpherson, J. V.; Slevin, C. J.; Unwin, P. R. *Analytica Chimica Acta* **1999**, *385*, 223-240.

(2) Hengstenberg, A.; Kranz, C.; Schuhmann, W. *Chemistry-a European Journal* **2000**, *6*, 1547-1554.

(3) Katemann, B. B.; Schuhmann, T. *Electroanalysis* **2002**, *14*, 22-28.

(4) Katemann, B. B.; Schulte, A.; Schuhmann, W. *Chemistry-a European Journal* **2003**, *9*, 2025-2033.

(5) Mirkin, M. V.; Horrocks, B. R. *Analytica Chimica Acta* **2000**, *406*, 119-146.

(6) Liu, B.; Rotenberg, S. A.; Mirkin, M. V. *Proceedings of the National Academy of Sciences of the United States of America* **2000**, *97*, 9855-9860.

(7) Yasukawa, T.; Kaya, T.; Matsue, T. *Electroanalysis* **2000**, *12*, 653-659.

6. FUTURE WORK AND OVERALL CONCLUSIONS

6.1 ABSTRACT

The dissertation project is the first step toward sensors for dopamine detection in the presence of interferences through the electrochemical method of redox cycling, which has the potential for elimination of irreversible redox species as well as for avoiding background subtraction. The studies completed here lay the groundwork for a possible successful device. This section proposes some future studies to aid in design and preparation of a sensor for testing in brain. The future work includes:

1. Characterize and determine detection limits for redox cycling at the IDAs on the probe-like sensors in a-CSF buffer with dopamine and common interferents (e.g. norepinephrine, epinephrine, L-DOPA, serotonin, homovanilic acid, uric acid).
2. Fabricate the optimized probe-like IDA sensors with parameters based on the studies already performed and based on the studies proposed.
3. Optimize the thickness of Nafion to obtain response time of 10 ms for the initiation of redox cycling.
4. Study local electrochemistry of dopamine and ascorbate interaction during redox cycling on the surface of the sensor through scanning electrochemical microscopy.

6.2 FUTURE WORK

6.2.1 Characterize and determine the detection limits for redox cycling at the IDAs on probe-like sensors in a-CSF buffer with dopamine and common interferents. Five different designs of the IDAs were fabricated on the probe-like devices. Two of the devices contain IDAs that are bigger (260 µm x 260 µm) than the dimensions suitable for tissue insertion studies. They were fabricated keeping in mind the need to establish the fabrication procedure and simplification of the process. The other three IDAs have the dimensions (260 µm x 100 µm) suitable for tissue insertion studies. The smaller IDAs have been characterized and detection limits determined with the model compound, 5 mM hexaammineruthenium (III) chloride.

Characterization of the IDAs. Based on the data obtained to-date, it is anticipated that the sensor should be able to detect 5 µM dopamine in the presence of up to 100 µM ascorbate. It is now required to verify this prediction by obtaining experimental data. The sensors still need to meet the size requirements for insertion into brain tissue, in vivo. This makes the sensors limited in terms of the electrochemical area of the IDA. Therefore it is important to determine the detection limits of the fabricated IDAs in dopamine before further improvements in their design. Fabrication of these IDAs require huge time and cost investment. It will not be worthwhile to spend the time and energy in improvement of the sensors if they cannot detect down to 1 µM dopamine in presence of 100 µM ascorbate or if they cannot survive the harsh conditions during exposure to a-CSF buffer and other biochemicals (dopamine, ascorbate, etc) for 5 hours or more.

Calibration curves of the IDAs should be obtained in different concentrations of dopamine in presence and absence of 100 µM ascorbate in a-CSF buffer (pH 7.4). Detection limits of dopamine will be obtained. The IDAs will be characterized before and after the

calibration curves. Any effect on their electrochemical activity (such as fouling of the electrodes) will be examined. Different designs of the IDAs will be compared and the optimized arrangement of generator and collector electrodes will be used for the final design of the sensors.

The electrochemical behavior of dopamine under redox cycling conditions was examined in presence of two common interferences, ascorbate and DOPAC. A sensor was fabricated with interdigitated microelectrodes that are 4 µm in width and separated by 4 µm gap and overall array dimensions suitable for tissue insertion studies. Based on the data obtained from characterization studies, it is anticipated that in order to achieve the required detection limit for dopamine (1 µM) the microelectrode gap needs to be optimized to at least 0.8 µm (or smaller if possible).

The collection efficiency of redox cycling increases exponentially with decrease in the inter electrode spacing. With decrease in the inter electrode spacing, diffusion distance of the redox species between generator and collector electrodes decreases with the following relation estimated by Niwa et al[2]

$$d = 0.232w + g \qquad (2)$$

where w is the width of the electrode (4 µm) and g is the gap between the electrodes (4 µm). Decrease in diffusion distance will lead to greater number of redox cycles for the molecule before it finally diffuses out to the bulk. The diffusion length of a molecule is proportional to the square root of time the molecule requires to diffuse through the distance. For w = g, a decrease in feature size by a factor of 10 will also decrease the diffusion distance by a factor 10, but the diffusion time by the factor of $(10)^2$ i.e. by a factor of 100.

The spatial resolution of 4 µm achieved in the fabricated sensors is based upon the limitation of the instrumentation available in HiDEC. The HiDEC at the University of Arkansas

is acquiring an electron beam writer in November 2011. That instrument will make it possible to obtain down to 0.1 µm resolution of the features using photolithography. It will therefore be possible to fabricate devices containing features as small as 0.1 µm with a spacing of 0.1 µm. The final sensor design will not only contain smaller electrode widths with smaller gaps, but their total tip width will also be reduced to 100 µm. The length of the insertion tip will be increased to 4 mm with the IDA located at the end of the tip before it starts to taper. Once 1 µM detection capability for dopamine is achieved and the sensor with 100 µm width x 100 µm thickness are fabricated, they will be sent to Dr. A.C. Michael at the University of Pittsburgh, Pennsylvania for testing in brain tissue.

Study other common interferences in dopamine detection on IDAs using redox cycling. The compounds that act as common interferences in dopamine detection in brain include norepinephrine, epinephrine, L-DOPA, serotonin, homovanilic acid, uric acid. These are electroactive in nature in the potential range similar to that for dopamine (- 0.2 V to + 0.5 V). Most, not all, of them are usually found in concentrations much higher than that for dopamine (0.01 – 1 µM). Carbon fiber electrodes are used commonly to study these compounds using FSCV. Carbon fibers do not discriminate these compounds from each other or from ascorbate. In the worst case scenario, redox cycling might not be an improvement in discrimination. However, there are other options with redox cycling that do not exist with FSCV, such as holding different potentials at different generators and collecting at different potentials simultaneously. This approach still needs to be determined and investigated. The behavior of ascorbate and DOPAC has been studied in presence and absence of redox cycling. Redox cycling eliminates the ascorbate signal at the collector, thus providing selectivity toward dopamine. The method shows

similar sensitivity toward DOPAC and dopamine. Thus, additional methods to improve dopamine selectivity had to be explored such as coating of the electrodes with Nafion.

There are physiological controls that aid in determining whether the carbon fibers sense dopamine or other neurotransmitters, such as provision of biologically specific stimulus, or the application of selective potentials using voltammetric techniques such, or tissue content measurement. Similar methods can be employed for redox cycling as well. Thus, it might be okay that total selectivity towards dopamine is not obtained.

For the success of the redox cycling method in vivo, it is important to first explore the behavior of other interfering compound on these sensors. Sensitivity of the sensor toward interferences and selectivity toward dopamine in their presence need to be determined. If redox cycling alone does not exhibit the required selectivity and sensitivity toward dopamine, additional methods (such as electrode coatings or modification methods) need to be explored. Calibration curves of dopamine in presence of the interferences need to be obtained and detection limit of dopamine needs to be determined.

6.2.3 Optimization of the thickness of Nafion to obtain better response time for redox cycling. The perfluorinated sulphonated cation exchange membrane, Nafion, allows positively charged compounds such as dopamine (at pH 7.4) to permeate through its layer and reach the electrode surface. The negatively charged ions such as ascorbate and DOPAC (at pH 7.4) are repelled. Thus, Nafion will improve dopamine selectivity in the presence of DOPAC and ascorbate. Behavior of other interfering compounds on the Nafion-coated electrodes needs to be determined in presence of dopamine with and without redox cycling.

In the studies conducted thus far, 500 nm thick layer of Nafion coated on the electrodes decreased the response time of redox cycling, as expected. This will create problem in measuring the dopamine transients occurring on seconds to sub-second time scale. The slow step is the dopamine getting in and out of the Nafion, perpendicular to the chip. Mass transfer through solution between generator and collector is not hindered, however. Thus, a thinner layer of Nafion should significantly improve the response time, which should scale with the square of its thickness, ϕ ($t = \phi^2/2D$), based on the Einstein formulation for random-walk diffusion. A thickness of 23 nm, for example, should offer an improvement of 473 fold in time response (from 5 s to 0.010 s, where 0.010 s is the desired response time for FSCV at CFEs). In order to obtain the required thickness, dilution of Nafion such as with ethanol or isopropanol can be explored as well as high spin rates during deposition. An alternative would be surface modification with negatively-charged molecular species, which would provide the thinnest layer possible (~1 to 5 nm).

6.2.4 Study of local electrochemistry of dopamine and ascorbate interaction in their mixture during redox cycling on the surface of the sensor and determination of optimal electrode parameters for dopamine detection. This will be accomplished through scanning electrochemical microscopy (SECM). It is important to study the local interactions between dopamine and ascorbate during redox cycling to determine the effect of secondary processes such as the survival of dopamine-quinone from its spontaneous reaction with ascorbate and intramolecular cyclization of dopamine. This should help evaluate the results as well as build a sensor containing electrode designs which might minimize the extent of the secondary reactions.

The microelectrochemical devices consist of arrays of microelectrodes fabricated on a silicon chip with photolithography. The process is expensive and time-consuming, without variability of electrode shape or dimensions, except by fabricating a new set of arrays.[1] SECM will be used in three ways, making this study time and cost-efficient: (1) to provide variable, real-time, high-precision spacing between its tip (where oxidation occurs) and individual microelectrodes on the chip (where reduction occurs) to determine the most desirable gap between electrodes *before* fabricating the final sensor design, (2) to follow reaction products resulting from redox cycling at the array on the chip, and (3) to determine the a trend in electrode fouling areas on the arrays, if any and troubleshoot the poorly performing electrodes in the array. The Fritsch lab has acquired SECM – 004 from Sensolytics GmbH, Bochum, Germany, equipped with a tripotentiostat, stepper motors for movement of the tip with micrometer resolution and piezocube for the movement of the tip with nanometer resolution.

Height-dependent redox cycling between SECM tip and microelectrodes contained in the IDA to determine maximum gap between electrodes for desired sensitivity during redox cycling. Redox cycling should be performed as a function of distance between the SECM tip and one

active microelectrode on the IDA. The tip will be fixed in a single x,y location, while the vertical, z dimension will be scanned. The SECM tip can be set to oxidize while the microband electrode is reducing, as shown in Figure 6.1, or visa-versa. The current at the tip as a function of its vertical displacement from a small chip electrode will determine the separation between IDA electrodes needed to achieve optimal signals for a final design. Current at the SECM tip will be plotted as a function of distance away from one active microelectrode for the configuration where the microelectrode will serve as the generator and the tip as a collector. Microelectrode will serve as the generator and tip as the collector.

The SECM tip should be positioned over the center of the active microelectrode. Current at the SECM tip should be monitored as a function of distance in the z-direction from the active electrode. Redox cycling can be investigated in multiple ways. The generator can be ramped up from reducing potential to oxidation potential (cyclic voltammetry) to convert the arriving dopamine to its quinone form while the collector remains at reducing potentials. The generator can be held at constant oxidizing potential while the collector electrode remains at a constant reducing potential. In this way, the collector electrode can more accurately track the time dependence of dopamine arrival with a limit in time resolution that depends on the gap between the electrodes and the size and geometry of the collector electrode. In all cases, the desirable measurement of dopamine will be at the collector. Since the collector will be held at a constant reducing potential, it will not exhibit a background (charging) current.

2D-imaging of redox cycling at a microelectrode array to follow reaction products resulting from redox cycling at the array on the chip. Two dimensional imaging of oxidized and reduced redox species (shown in Figure 6.2) will be performed by the SECM tip over an IDA that is undergoing redox-cycling. Current will be measured at the tip held at different potentials

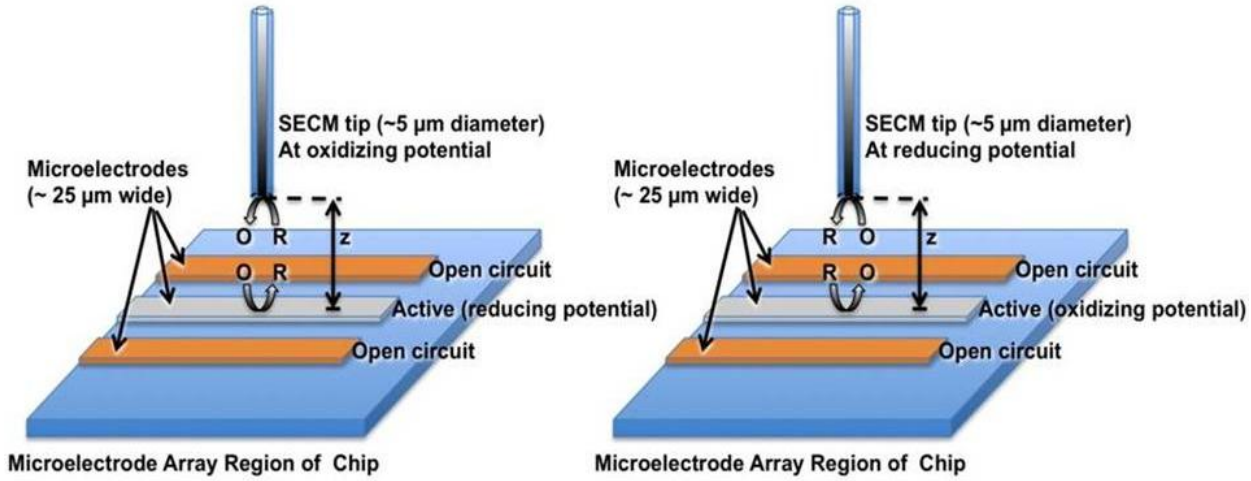

Figure 6.1. Representation of height dependent redox cycling studies between SECM tip and a microelectrode. The tip can be raised and lowered in z-direction, capable of evaluating dependence of redox cycling signal on the separation between oxidizing and reducing electrodes.

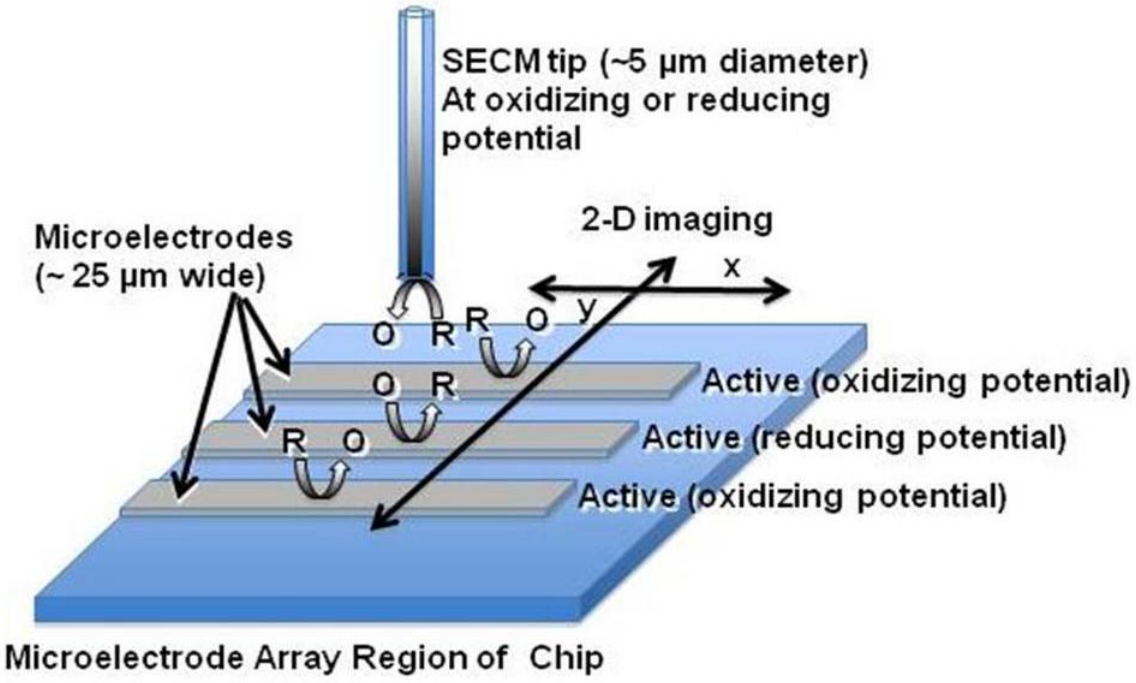

Figure 6.2. Representation of 2D imaging of redox cycling at microelectrode array to image the changes in the concentrations of redox species while undergoing redox cycling.

(once at oxidizing and once at reducing potentials) while it scans the microelectrodes of IDA in x and y directions. This will allow imaging of changes in the concentration of oxidized and reduced forms of dopamine and ascorbate resulting from redox cycling at the array. Effects of continuous redox cycling on the solution composition will be studied. Monitoring of the survival of oxidized dopamine in presence of ascorbate to undergo redox cycling will be possible. The tip will either be held at oxidizing or at reducing potential. All microelectrodes in the array will be involved in redox cycling and will be polarized at oxidizing or reducing potentials based up on the desired configuration of generator and collector.

Motion of the SECM tip: The SECM tip will be positioned over a region of the array where more than one microelectrode is visible in the 2-D image. One position of the tip could be near one end of the array where parts of more than one microelectrode and their short ends can be imaged. Current at the tip should be monitored as a function of x-y location. The SECM tip will scan over the substrate and image the location of dopamine and ascorbate using oxidizing potential, and of dopamine-quinone using reducing potential. Study of dopamine, of ascorbate, and of their mixture will throw a light on the effect of the reaction between ascorbate and dopamine-quinone, which suppresses the signal at the collector from reduction of oxidized dopamine.

Experimental considerations of the homogeneous chemical interactions of dopamine and ascorbate. In solution, the reaction between ascorbate and dopamine-quinone is spontaneous, forming dihydroascorbic acid and returning dopamine to its reduced form. This phenomenon suppresses the signal from reduction of dopamine-quinone at collector. However, this reaction is known to have slow kinetics.[22,24,30,43] Exploiting the slow kinetics of the reaction by decreasing the gap between electrodes can alleviate this effect. If the gap between electrodes is successfully

optimized, the reaction could be negligible on the time frame of the mass transfer across the gap. The inherent nature of redox cycling to consume ascorbate (by its oxidation at generator) should also inhibit the reaction from occurring.

Oxidized dopamine undergoes intramolecular cyclization to form substituted indole[55], which cannot be reduced at the collector and thus, does not contribute to the signal. This leads to a suppressed signal at collector. Because the generator and collector electrodes are at a fixed separation, this suppression in current can be calibrated and accounted for. It will be harder to account for suppression in current due to the reaction of ascorbate and dopamine-qiunone because it depends on the relative amounts of the two species which are not known apriori. Thus, in the latter case, it is important to either eliminate or minimize the reaction or make the experiment so fast that it is not a problem. The rate of indole formation is also slow. Decreasing the gaps between generator-collector pairs should decrease the time before oxidized dopamine is re-reduced, minimizing its loss.

2D-imaging of microelectrode array at open circuit to determine fouled areas on the arrays, if any and troubleshoot the poorly performing electrodes in the array. When the SECM tip at oxidizing or reducing potentials approaches a microelectrode at open circuit immersed in a solution of redox species, an enhancement in SECM current, called positive feedback, results. This occurs because oxidized and reduced forms of the chemical species equilibrate (exchange electrons) through the conductor, shuttling electrons from species distant to the region directly under the tip. However, if the region of the microelectrode directly under the tip is insulated due to fouling, current at the tip does not increase. Two dimensional image of MEA at open circuit potential will be obtained at the SECM tip as a function of x and y locations as shown in Figure 6.3. Essentially, this is a sensitive method for imaging the activity of surfaces of

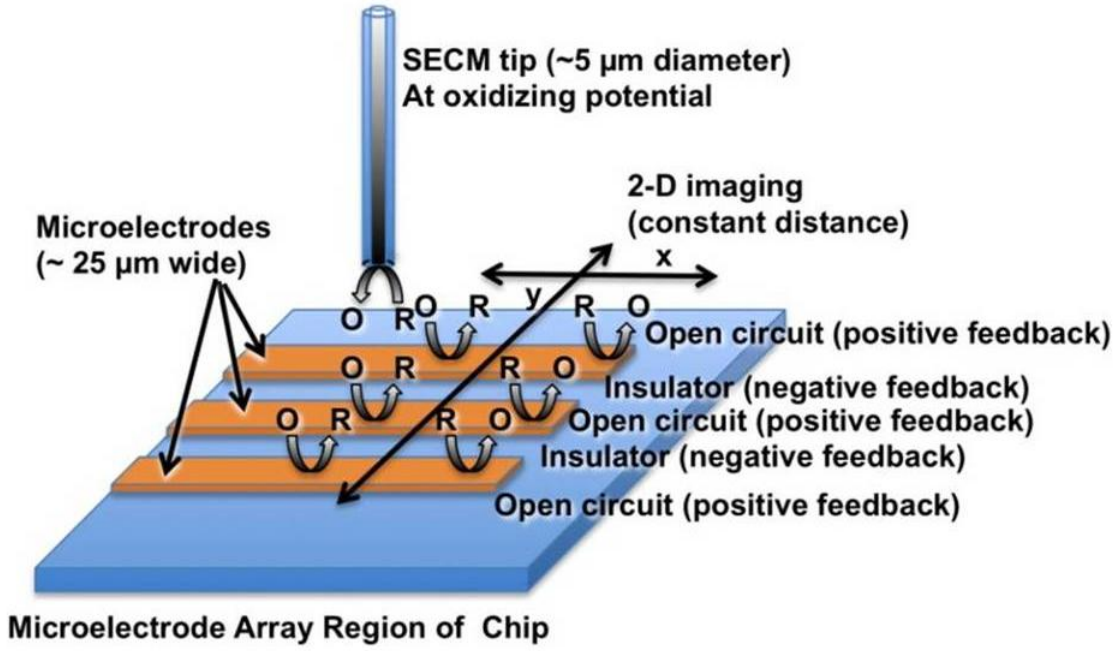

Figure 6.3. Two dimensional imaging of MEA at open circuit potential to assess quality of electrodes before and after redox cycling experiments locating inactive regions of electrodes.

microelectrodes, and needs to be performed with model species regularly to characterize the microelectrodes, especially before and after studies involving dopamine, which is known to foul electrodes over time. If a pattern of fouled regions of the arrays is determined, alternative designs of geometries and dimensions of electrodes can then be adapted to diminish the fouling.

Motion of the SECM tip: The SECM tip will be positioned over a region of the array where more than one microelectrode is visible in the two dimensional image, such as near one end of the array where parts of more than one microelectrode and their short ends can be imaged.

6.3 CONCLUSIONS

This project is the first step toward creating an interdigitated microelectrode array sensor that will employ the method of redox cycling for detection of dopamine with increased sensitivity and selectivity.

A new electrochemical method for detection of compounds, *redox cycling*, has been studied and developed for detection of compounds. *Closely spaced individually addressable microelectrodes* contained in an array have been fabricated for the purpose of exploring redox cycling with the provision of flexibility in electrode space and electrode arrangement. This has made possible to conduct a unique study where *individual elements composing the generator and collector electrodes were monitored* independently using a multipotentiostat. Different geometries of microelectrodes have been compared in order to determine the best possible conditions for carrying out the most efficient redox cycling of compounds.

The method of *redox cycling* is further developed specifically *for the detection of dopamine in presence of ascorbate and DOPAC* at physiologically relevant concentrations. The optimized design of the electrodes is transferred on to *probe like redox cycling sensor arrays*.

The electrodes in the IDA do not contain exactly the same dimensions as in the MEA. Thus, further improvements are needed so that the overall in vivo dimensions will still achieve the desirable detection limits and response times. Characterization data and theoretical calculations of the probe arrays reveal that: *by bringing the electrode width and gap to 0.8 µm the optimized sensor design can detect physiological concentrations of dopamine, redox cycling method can eliminate interference from electrochemically irreversible compounds such as ascorbate, by coating electrode with polymer such as Nafion interference from reversible but negatively charged compounds (at pH 7.4) such as DOPAC can be eliminated.*

The ultimate goal is to fabricate the probe-like sensors having 100 µm x 100 µm dimension by using DRIE and to achieve 1 µM detection limit for dopamine in presence of 100 µM ascorbate on those sensors at which point they will be ready to be sent to Dr. Adrian Michael for further testing in vivo.

6.5 REFERENCES

(1) Henry, C. S.; Fritsch, I. *Journal of the Electrochemical Society* **1999**, *146*, 3367-3373.

(2) Niwa, O.; Morita, M.; Tabei, H. *Electroanalysis* **1994**, *6*, 237-243.

APPENDIX A: SYMBOLS USED

AA	ascorbic acid
A_F	amplification factor
BCB	benzocyclobutene
C	collector electrode
C_e	collection efficiency
CFE	carbon fiber electrode
CV	cyclic voltammetry
DA	dopamine
DAQ	dopamine-quinone
Do	diffusion coefficient
DOPAC	3,4-dihydroxyphenylacetic acid
DRIE	deep reactive ion etching
FSCV	fast scan cyclic voltammetry
G	generator electrode
IDA	interdigitated array
LOD	limit of detection
MEA	microelectrode array
RCA	Radio Corporation of America
RIE	reactive ion etching
RRDE	rotating ring disk electrode
RSD	relative standard deviation

Ru^{n+}	shorthand for $[Ru(NH_3)_6]^{n+}$
SECM	scanning electrochemical microscopy
g	gap
i.d.	inner diameter
$i_{G/C}$	current at the generator electrode with collector 'on'
i_G	current at the generator electrode with collector 'off'
i_C	current at the collector electrode
l	length
o.d.	outer diameter
r_i	inner radius
r_o	outer radius
t	time
w	width